Transport Processes in Snow and Ice Crystal Icing

Vom Fachbereich Maschinenbau
der Technischen Universität Darmstadt
zur
Erlangung des Grades eines Doktor-Ingenieurs (Dr.-Ing.)
genehmigte

Dissertation

vorgelegt von

Kilian Köbschall, M.Sc.

aus Mainz

Berichterstatter:	Prof. Dr.-Ing. Cameron Tropea
1. Mitberichterstatterin:	Prof. Dr.-Ing. Jeanette Hussong
2. Mitberichterstatter:	Prof. Pierre Trontin
Tag der Einreichung:	30.05.2023
Tag der mündlichen Prüfung:	03.08.2023

Darmstadt 2023

D 17

Köbschall, Kilian:
Transport Processes in Snow and Ice Crystal Icing

Darmstadt, Technische Universität Darmstadt
Jahr der Veröffentlichung der Dissertation auf TUprints: 2023
Tag der mündlichen Prüfung: 03.08.2023

Bitte zitieren Sie dieses Dokument als:
URN: urn:nbn:de:tuda-tuprints-244704
URL: https://tuprints.ulb.tu-darmstadt.de/id/eprint/24470

Dieses Dokument wird bereitgestellt von TUprints, E-Publishing-Service der
Technischen Universität Darmstadt
http://tuprints.ulb.tu-darmstadt.de
tuprints@ulb.tu-darmstadt.de

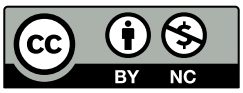

Erklärung

Hiermit erkläre ich, dass ich die vorliegende Arbeit, abgesehen von den in ihr ausdrücklich genannten Hilfen, selbständig verfasst habe.

Darmstadt, den 30.05.2023 

K. Köbschall

Abstract

Icing caused by snow and ice crystals poses a serious threat in aviation. Ice crystals ingested into jet engines can partially melt, which facilitates the adhesion of the ice particles to engine components. The accumulated ice deteriorates engine performance and shedding of the accretion can extinguish the combustion or cause severe damage. Helicopters are particularly vulnerable to wet snow, which can clog the engine intake, reducing efficiency and potentially causing a flameout when shed into the engine. The associated physical phenomena are diverse and not yet completely understood. Therefore, the objective of this thesis is to provide insight into several key processes involved in snow and ice crystal icing.

In the first part of this thesis, transport processes of airborne snowflakes are studied. Numerical tools to predict icing require accurate models to determine the trajectory and liquid fraction of snowflakes, which is challenging due to their highly complex shape. To improve the estimation of the drag coefficient, an experimental study is performed using artificial snowflakes. Additionally, a theoretical model, based on the convex hull of the particle is developed. This model enables the estimation of three-dimensional descriptors from two-dimensional particle projections, which drastically reduces the required information to predict snowflake drag.

Experiments are conducted on the melting of laboratory-generated snowflakes. A theoretical model is proposed and validated by comparing the predicted size evolution and melting duration against experimental results. The novel model requires less empiricism than previous models and is able to account for different particle morphologies.

The second part of this thesis considers the water transport in porous ice layers. First, imbibition into melting granular ice layers is investigated. A capacitive sensor is developed and utilized to characterize the space and time resolved liquid distribution during imbibition. Pore saturation is found to increase with decreasing porosity. Decreasing grain size and increasing volume flux due to melting result in a sharper decline in saturation.

Finally, a capacitive measurement instrument for the application in icing wind tunnels is developed. This novel instrument uncovers the liquid distribution in ice accretions, which was previously inaccessible in experimental studies. The conducted wind tunnel experiments reveal the relation between liquid fraction and growth rate of an ice layer.

The gained insights presented in the present thesis enable an enhanced prediction of snow and ice crystal icing and can thereby improve safety and efficiency in aviation.

Kurzfassung

Die Vereisung durch Schnee- und Eiskristalle stellt in der Luftfahrt ein erhebliches Sicherheitsrisiko dar. Eiskristalle, die in Triebwerke eingesaugt werden, können teilweise schmelzen, wodurch das Anhaften der Eispartikel an Triebwerkskomponenten erleichtert wird. Auftretende Eisansammlungen verschlechtern die Triebwerksleistung und deren Ablösen kann die Verbrennung zum Erlöschen bringen oder schwere Schäden verursachen. Hubschrauber sind insbesondere durch nassen Schnee gefährdet, der den Triebwerkseinlass verstopfen kann, wodurch die Effizienz beeinträchtigt wird und es zu einem Flammabriss kommen kann, wenn das Eis in das Triebwerk gelangt. Die damit verbundenen physikalischen Phänomene sind vielfältig und noch nicht vollständig verstanden. Ziel der vorliegenden Arbeit ist es, einen Einblick in mehrere entscheidende Prozesse zu geben, die an der Schnee- und Eiskristallvereisung beteiligt sind.

Im ersten Teil dieser Arbeit werden die Transportprozesse von Schneeflocken in Luftströmungen untersucht. Numerische Werkzeuge zur Vereisungsvorhersage erfordern genaue Modelle für die Berechnung der Trajektorie und des Flüssigkeitsanteils von Schneeflocken, was aufgrund deren komplexer Form eine Herausforderung darstellt. Um die Vorhersage des Widerstandsbeiwertes zu verbessern, wird eine experimentelle Studie mit künstlichen Schneeflocken durchgeführt. Zusätzlich wird ein theoretisches Modell entwickelt, das auf der konvexen Hülle des Partikels basiert. Dieses Modell ermöglicht die Schätzung dreidimensionaler Beschreibungsgrößen anhand zweidimensionaler Partikelprojektionen, wodurch die für die Vorhersage des Luftwiderstandes von Schneeflocken erforderlichen Informationen drastisch reduziert werden.

Das Schmelzen von im Labor erzeugten Schneeflocken wird experimentell untersucht. Ein theoretisches Modell wird vorgeschlagen und durch den Vergleich der vorhergesagten Größenentwicklung und Schmelzdauer mit den experimentellen Ergebnissen validiert. Das neue Modell erfordert weniger Empirie als frühere Modelle und ist in der Lage, unterschiedliche Partikelmorphologien zu berücksichtigen.

Der zweite Teil der Arbeit befasst sich mit der Untersuchung des Wassertransports in porösen Eisschichten. Zunächst wird das Aufsaugen von Wasser in schmelzende granulare Eisschichten untersucht. Ein kapazitiver Sensor wird entwickelt und eingesetzt, um die räumlich und zeitlich aufgelöste Flüssigkeitsverteilung während des Prozesses zu charakterisieren. Es wird festgestellt, dass die Sättigung der Poren mit abnehmender Porosität ansteigt. Eine abnehmende Korngröße, sowie eine zunehmende, durch das Schmelzen bedingte Volumenstromdichte, führen zu einem steileren Abfall der Sättigung.

Schließlich wird ein kapazitives Messinstrument für den Einsatz in Vereisungswindkanälen entwickelt. Dieses neuentwickelte Instrument ermöglicht die Untersuchung der Flüssigkeitsverteilung in Eisanwüchsen, welche zuvor in experimentellen Untersuchungen nicht gemessen werden konnte. Die durchgeführten Windkanalversuche zeigen einen Zusammenhang zwischen dem Flüssigkeitsanteil einer anwachsenden Eisschicht und ihrer Wachstumsrate.

Die in der vorliegenden Arbeit gewonnenen Erkenntnisse ermöglichen eine verbesserte Vorhersage der Schnee- und Eiskristallvereisung und können so die Sicherheit und Effizienz in der Luftfahrt verbessern.

Acknowledgments

First and foremost, I would like express my deepest gratitude to **Prof. Dr.-Ing. Cameron Tropea** for providing me with the opportunity to start this work at the Institute of Fluid Mechanics and Aerodynamics. His invaluable advice, supervision and guidance throughout the years have been instrumental to the success of this work.

I am also deeply grateful to **Prof. Dr.-Ing. Jeanette Hussong** for her exceptional support, guidance and the countless fruitful discussions and ideas that have significantly contributed to the development of this work.

I would like to extend my appreciation to **apl.-Prof. Ilia V. Roisman** for his insightful ideas and valuable suggestions, which have enhanced the quality of this research.

My gratitude extends to my colleagues at the institute for their unwavering support, engaging discussions, their invaluable input and proofreading of this work. Thank you, **Louis Reitter**, **Niklas Apell**, **Max Lausch**, **Philipp Brockmann**, **Bastian Stumpf**, **Marija Gajevic Joksimovic**, **Ivan Joksimovic**, **Benedikt Schmidt**, **Ang Sun** and **Jan Breitenbach**.

I am particularly thankful to **Boris Aguilar** of ONERA and **Yasir A. Malik** of TU Braunschweig for the constructive discussions and productive collaborations that have enhanced this research.

A special mention goes to the workshop team whose inputs and suggestions have been invaluable in conducting the experiments. Without their expertise and dedication, this work would not have been possible.

I am immensely grateful to **Jan Oberreuter**, **Benjamin Traut**, **Ang Sun**, **Stephan Tecklenburg**, **Hendrik Beck**, **Johannes Kleudgen** and **Viktor Berchtenbreiter** for their significant contributions to this work through their theses and beyond. Their involvement has been vital to the realization of the experiments.

I would like to acknowledge the European Commission for funding the projects **ICE GENESIS** (grant agreement 824310) and **MUSIC-haic** (grant agreement 767560), within the framework of which this work has been conducted. I am also grateful to the numerous project partners involved in these projects, whose contributions have greatly enhanced this thesis.

Finally, I would like to express my deepest appreciation to my family and friends for their ongoing encouragement and belief in me. A special thank you goes to my girlfriend **Christina** for her continuous support, patience and understanding throughout this journey and beyond!

Contents

1 Introduction

From the symmetry of pristine ice crystals to the complexity of snowflakes, the beauty of ice and snow structures captivates the observer. However, beyond their aesthetic allure, ice and snow can also pose significant threats to a wide range of applications.

The accumulation of ice on windshields, roadways and bridges affects road safety and causes numerous accidents every winter [22, 68]. Icing of power lines increases their weight and vibrations caused by subsequent shedding of ice can cause structural damage [105, 53]. Ice and snow on photovoltaic systems or satellite dishes significantly reduce their performance [54]. Ice accretion on airfoils of wind turbines increases drag and thereby decreases their efficiency [84, 145]. Similarly, aircraft wings, fuselage and other components are susceptible to icing caused by supercooled drops, i.e., liquid drops below freezing temperature, affecting aircraft performance and posing serious risks to aviation safety [64].

However, ice accretion is not only limited to structures in cold environments. Ice particles that partially melt in the warm compressor stages of jet engines can cause the accumulation of ice and result in power-loss and damage components when shed [127]. Similarly, wet snow can accrete on the engine intake of helicopters and affect their operation [169]. Furthermore, impacting frozen particles can accumulate on warm engine components and heated measurement probes. Ice accretion due to ice crystal impact is referred to as ice crystal icing (ICI). These risks associated with snow and ice crystal icing motivate the research conducted in this thesis and are elaborated in the following.

1.1 Motivation

Aircraft icing during flight is most commonly caused by the impact of supercooled liquid droplets, which freeze upon impact or shortly thereafter [64]. This typically occurs on exposed surfaces such as the wings and fuselage, or on parts of the engine, which include the inlet, the spinner, the fan blades and the initial stages of the compressor. For a long time, it was believed that ice particles do not pose a substantial threat to aviation safety, since they were considered to mostly bounce off cold surfaces. Hence, no significant accretion was expected. However, in the last decades, many engine icing events have been reported that occurred at cruise altitudes above the limit up to which supercooled liquid is expected [107, 127]. These events commonly occurred in the vicinity of convective clouds, where ice crystals occur in high concentration. Ice crystals in these clouds have been found

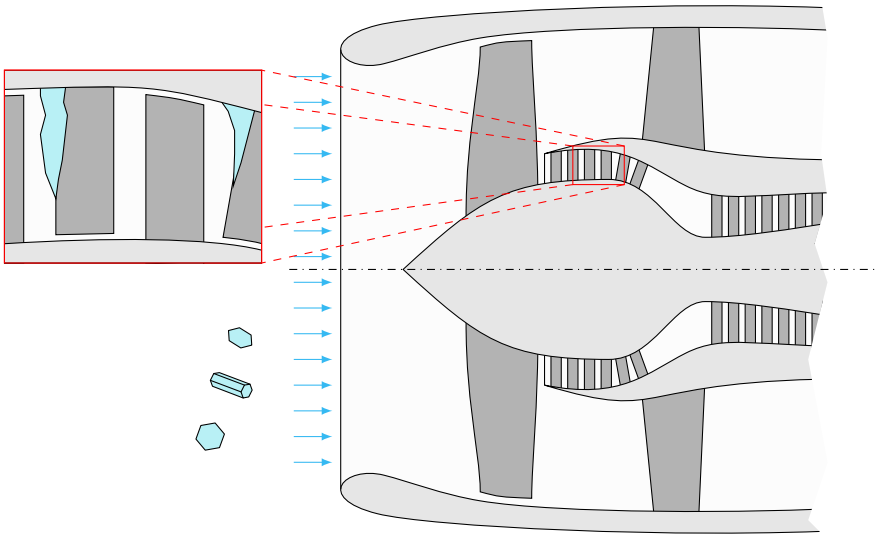

Figure 1.1: Jet engine compression system with ingested ice particles. The early stages of the system are susceptible to icing due to supercooled liquid water. Ice particle accretion mostly occurs on the stators and the casing of the compressor.

to be accountable for the engine icing events [127]. While ice particles do not accumulate on the wings, the engine inlet and fan components, ice crystals in the engine have been shown to accrete on static components with a local temperature significantly above freezing. An accretion at an exemplary site in the low-pressure compressor stage, which is prone to ice crystal icing, is illustrated in Figure 1.1.

The ingested ice particles are exposed to the warm environment inside the engine and partially melt. The presence of liquid water in the airflow was found to facilitate adhesion of the particles to the substrate upon impact [176, 46]. This is commonly expressed as the melt ratio, which specifies the proportion of liquid water content to total water content in the flow.

The formed ice accretion represents a flow blockage and deteriorates the airfoil of the engine blades. Thereby, it adversely affects the performance of the engine. Eventually, the accumulated ice can detach and impact downstream blades. The caused damages typically include blade tip curl, but in some cases blade release can occur. Shed ice entering the high-pressure compressor or combustor can cause a compressor stall and surge or extinguish the combustion.

Ice crystal icing does not only occur in an aircraft engine, but can also cause ice accretion on measurement probes, which provide vital information to the pilots, auto-pilot and engine control. The accreted ice can hinder the measurement or result in a malfunction.

Snow poses a severe risk for helicopters operating in cold environments. Especially encounters with wet snowflakes can cause the accumulation of snow on components

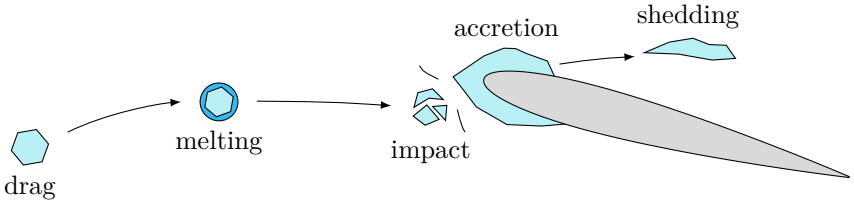

Figure 1.2: The main physical phenomena in icing due to ice crystals and snow.

of the helicopter. The accumulation on the grid protecting the engine intake can clog the air intake and reduce engine performance. Similarly, the ingestion of snow from external parts into the engine and shedding of ice accreted in the plenum chamber can cause engine flameout [169].

Icing due to ice crystals and snowflakes is facilitated by the availability of liquid water, which can have different origins. Based on the wet bulb temperature, distinct regimes can be defined. The wet bulb temperature is the lowest temperature achievable by evaporative cooling of a water-saturated surface in the ambient air. It is therefore a function of temperature and relative humidity of the airflow. At positive wet bulb temperatures, ice particles partially melt in the airflow and meltwater is therefore bound to the impacting particles. At negative wet bulb temperatures, water can coexist with the ice particles in the incoming air in form of supercooled drops. Clouds that exhibit both supercooled drops and ice crystals are referred to as mixed-phase clouds. Research indicates that at temperatures below $-40\,°C$ all particles are frozen [158]. Liquid water can also originate from a heated substrate. This can be caused either by impinging particles, which can partially melt upon impact, or by the melting of ice accumulated on the heated substrate.

The processes associated with ice crystal icing and icing in snow conditions are complex and include a variety of physical phenomena. The major processes are illustrated in Figure 1.2. Particle transport in the airflow and the resulting trajectories of ice crystals and snowflakes determine whether and where the particles impact. These trajectories are dictated by the mass and drag of the highly complex shaped particles. Furthermore, the particles may melt due to the ambient conditions experienced during particle transport. The liquid water introduced by melting affects whether the particles adhere to the surface upon impact. The impact dynamics determine the fragmentation and thus the size distribution of secondary reemitted particles. Moreover, ice particles impacting onto a heated substrate cause the formation of a liquid film, which again affects the particle adhesion to the surface. Upon the formation of an ice accretion, its liquid fraction and the distribution of liquid within the accumulation affect its mechanical properties and the accretion process. Finally, aerodynamic forces and melting of the ice accretion

can cause shedding of the ice layer.

Despite the significance of snow and ice crystal icing, the underlying physical phenomena are still not completely understood. Accordingly, the objective of the present thesis is to improve the understanding of multiple of these processes. The first part of this thesis addresses airborne snowflakes and encompasses experimental and theoretical studies on the **drag and melting of snowflakes**. The second part focuses on the experimental investigation of **water transport in porous ice layers** resembling ice accretions.

1.2 Theoretical background and state of the art

This section presents an overview of the theoretical background and recent findings of the physical phenomena investigated in this thesis. First, the characteristics of ice crystals and snowflakes are presented and the two types of particles are compared. Second, the key physical phenomena related to airborne snowflakes, including their drag and melting, are presented. Subsequently, the water transport in granular ice and snow layers is illuminated and the related process of ice accretion is shortly presented. Finally, various measurement techniques for quantifying liquid water in porous media are discussed, with a particular focus on capacitive sensing.

1.2.1 Comparison of ice crystals and snowflakes

The study of snow crystals has been present in research for many centuries. In a pioneering work in 1611, Kepler [95] discussed the hexagonal shape of snow crystals. A few years later Descartes [51] described different morphologies of snow. In the past century, Bentley [14], who photographed thousands of snowflakes coined the saying that no two snowflakes are alike. Subsequently, systematic studies of snow crystal geometries have been performed by Nakaya and Terada [142] who proposed several classes of snow crystals. The most used classification for single snow crystals has been proposed by Magono and Lee [120]. In the following, the differences between regular ice crystals or snow crystals and snowflakes are described. This presents only a short overview of the associated phenomena. The book by Pruppacher and Klett [150] is recommended for more details.

Atmospheric ice particles can grow by three different mechanisms, which follow the nucleation of ice: vapor deposition, riming and aggregation [150]. Vapor deposition leads to the growth of a single ice crystal with shapes mostly determined by temperature and humidity [111]. These shapes include for example hexagonal plates, columns and dendrites. Riming of ice particles occurs when the particle collides with supercooled droplets. The droplets freeze upon impact and form a rough and porous structure on the ice crystal. The degree of riming is determined by the liquid water path of the particle, i.e., the liquid water encountered by

the particle along its path through the atmosphere. Rimed particles can range from barely rimed crystals up to heavily rimed particles, which are referred to as graupel [150]. Aggregation occurs upon collision of two or more snow crystals. Here the terminology of Pruppacher and Klett [150] is adopted and aggregates are referred to as snowflakes which are in contrast to single ice crystals. The classification of particles in natural snowfall revealed that aggregates contribute a major fraction of the overall particle population [20, 149, 85].

A visual comparison of atmospheric ice crystals and snowflakes is shown in Figure 1.3. Ice crystals are usually smaller than 1 mm, while snowflakes can reach sizes of multiple centimeters. A further difference can be recognized in the morphology of the particles. Ice crystals are solid bodies with irregular shape. In comparison, snowflakes represent porous particles with a more complex geometry. Due to the porosity – or void fraction – of snowflakes, they have low bulk densities.

The variety of different shapes of ice particles and the complex three-dimensional structure complicate the characterization of the particles. Leinonen et al. [110] developed a neural network, which enables an approximate three-dimensional reconstruction from stereo images of snowflakes. Despite this recent progress, correlations for snowflake properties and models for physical phenomena of snow are generally based on descriptors obtained from two-dimensional projections of the particle.

Exemplary geometric dimensions, based on a projection of the ice particle, are illustrated in Figure 1.4. The maximum dimension of the particle is denoted by the maximum Feret diameter. A Feret diameter or caliper diameter specifies the distance between two parallel planes that restrict the particle [135]. The diameter of a circle with the same area as the object is referred to as the area equivalent diameter. The roundness of the two-dimensional shape can be described by the Cox roundness defined as [39]

$$\Psi = \frac{4\pi A_\mathrm{p}}{P^2}, \tag{1.1}$$

where A_p specifies the projected area and P denotes the perimeter.

Similarly, several geometric descriptors can be defined for the three-dimensional geometry:

$$d_\mathrm{eq} = \sqrt[3]{\frac{6V}{\pi}}, \quad \Phi = \frac{\pi d_\mathrm{eq}^2}{A}, \quad \Phi_\perp = \frac{\pi d_\mathrm{eq}^2}{4A_\perp} \tag{1.2}$$

Here V denotes the volume of the body, A its surface area and $A_\perp$ the projected area normal to the direction of motion. Analogous to the area equivalent diameter, the volume equivalent diameter d_eq is the diameter of a sphere that has the same volume as the three-dimensional particle. The sphericity Φ of a body describes the ratio of the surface area of the volume equivalent sphere to the actual surface area of the body. Finally, the crosswise sphericity $\Phi_\perp$ is a measure of the orientation of a body and is defined as the ratio of the projected area of the volume equivalent sphere

(a) Exemplary ice crystals from the work of Heymsfield and Iaquinta [77]. (© American Meteorological Society. Used with permission.)

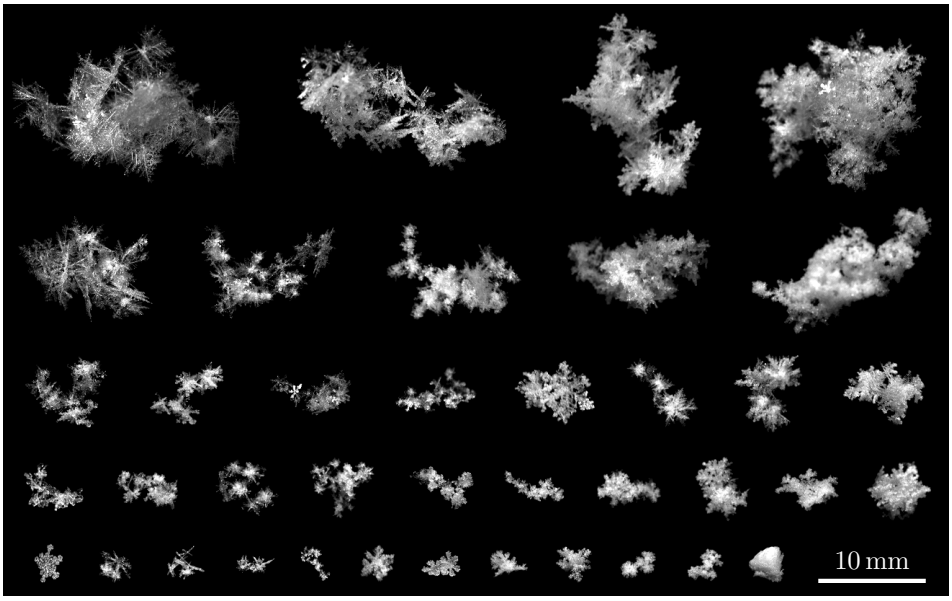

(b) Exemplary photographs of natural snowflakes from the database of Grazioli et al. [66].

Figure 1.3: Photographs of regular ice crystals and snowflakes in comparison.

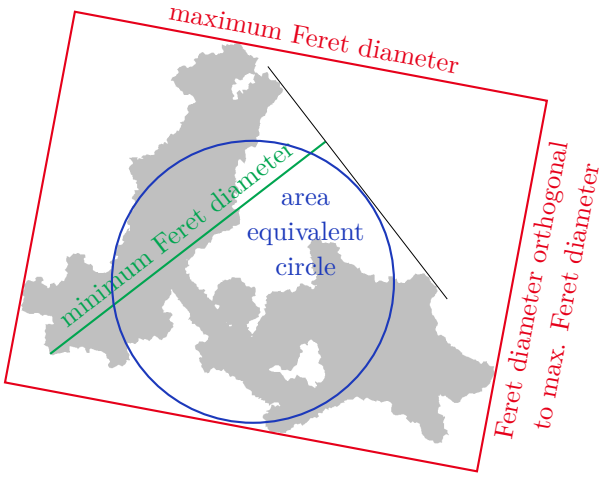

Figure 1.4: Various geometric descriptors of a two-dimensional projection of an exemplary snowflake.

to the projected area of the particle. However, in contrast to the two-dimensional descriptors, it is very difficult or infeasible to measure these three-dimensional descriptors for natural ice particles.

Several physical phenomena associated with ice crystals and snowflakes depend on the particle mass. Since this cannot be directly measured from a single photograph, multiple correlations have been proposed to relate the mass to properties of the two-dimensional projection. Baker and Lawson [10] proposed an empirical correlation for the mass of an ice particle in terms of the length, width, area and perimeter of the projection. However, the most common expression for the mass–size relationship is given by a power law [142, 115, 140, 24, 10]

$$m = \alpha d^{\beta}, \tag{1.3}$$

where m denotes the particle mass, d a characteristic length of the particle and α and β are parameters that are related to the morphological class of the particle and can be found in the literature. Fractal aspects have been found in various types of aggregates, including snowflakes [88, 18, 82, 161]. Therefore, the mass fractal dimension of snowflakes, i.e., the exponent β in the mass–size power law, is significantly lower than three.

Based on this mass–size power law, a similar correlation can be derived for the bulk density of the snowflake

$$\rho = \frac{6m}{\pi d^3} = \frac{6\alpha d^{\beta-3}}{\pi}. \tag{1.4}$$

Here the reference volume was arbitrarily chosen as the volume of a sphere with a diameter equal to the characteristic length of the snowflake.

Atmospheric researchers continue to characterize natural ice crystals and snowflakes, with a focus on the microphysical properties. The knowledge gained by these studies is an important input for the prediction of phenomena related to icing.

1.2.2 Drag of snowflakes

The trajectories of ice crystals and snowflakes determine whether or not a particle impacts on a surface, where it impacts and at what angle and velocity. To calculate this information, numerical tools solve the equation of motion of the ice particles. The particle dynamics are dictated by the drag force vector acting on the particle and its mass. The drag force is determined by the relative velocity between flow and particle, the particle size, shape and orientation. Since snowflakes exhibit highly complex shapes, the accurate physical representation of the particles and the calculation of the flow field around the body are very challenging.

The following literature review on the drag of nonspherical particles and snowflakes is based on the article *Geometric descriptors for the prediction of snowflake drag* by Köbschall et al. [103] published under CC BY 4.0 and has been extended for this work.

Up to date, many researchers studied the terminal velocity of snowflakes, which is of primary interest for the simulation of the microphysics of clouds and weather phenomena [160, 202]. Modern devices like the multi-angle snowflake camera (MASC) presented by Garrett et al. [61] automatically capture high-resolution photographs of falling ice particles from three angles and simultaneously measure the fall speed. This instrument enables the generation of large data sets for natural snow [149, 55, 66]. Several studies employ empirical relations for the prediction of the particle terminal velocity. These correlations are usually given as a power law in terms of the particle maximum dimension [106, 86, 115, 90, 12] or density [121]. The parameters of the power law are fitted to experimental data sets and are different for each morphological class. Further models for the terminal velocity of snowflakes, which take the particle mass and the projected area into account have been proposed [78, 138, 139, 96, 97]. However, Westbrook [195] found that these correlations significantly overpredict the fall speed of small particles, especially if they have an open geometry.

Snowflakes can take on a preferred orientation during free fall [62]. However, a rotational motion around the vertical axis can often be observed, which has been quantified by Kajikawa [90]. McCorquodale and Westbrook [134] describe a spiraling trajectory with a stable orientation for some snowflakes, while others exhibit unsteady trajectories. Snowflakes in turbulent flow show a more complex behavior. Cho et al. [28] concluded that the preferred orientation of ice crystals mostly prevails in turbulence. Various approaches exist to account for the orientation of the particle in a flow: Takano et al. [181] assumed a random orientation; Stephens [173] assumed that the longest axis of the particle is aligned in the horizontal

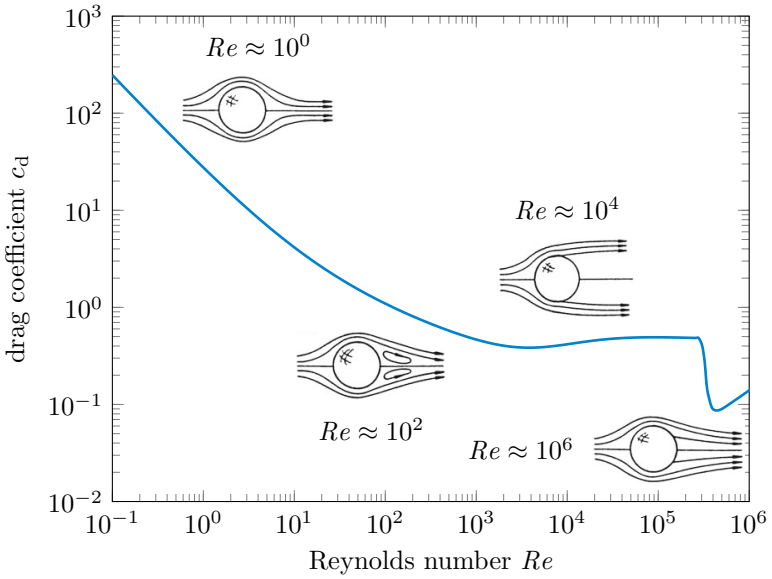

Figure 1.5: Drag coefficient of a sphere as a function of Reynolds number. (Reproduced from Spurk and Aksel [168] with permission from Springer Nature.)

plane and Matrosov [129] modeled the orientation of the particles with a Gaussian distribution.

The translation dynamics of an arbitrary body in a fluid flow are determined by the drag force vector. The magnitude of this drag force F_d is expressed in the dimensionless drag coefficient, which is defined as

$$c_d = \frac{2F_d}{\rho A_{ref} u^2}, \tag{1.5}$$

where ρ denotes the fluid density, A_{ref} a reference area and u the magnitude of the relative velocity of the particle in the fluid. The drag coefficient depends on the geometry and orientation of the particle and is a function of the Reynolds number. The Reynolds number is given by

$$Re = \frac{ud}{\nu} \tag{1.6}$$

and specifies the ratio of inertial forces to viscous forces. Here d is a characteristic length of the particle and ν is the kinematic viscosity of the fluid.

Well established correlations exist for the drag coefficient of a sphere in a steady incompressible flow. The diameter of the sphere defines the characteristic length d and its projected area gives the reference area A_{ref}. In Figure 1.5, the drag coefficient of a sphere is shown as a function of Reynolds number. One of the most widely used correlations for the drag coefficient of a sphere was proposed by Clift

and Gauvin [30] and is given by

$$c_\mathrm{d} = \frac{24}{Re}\left(1 + a_1 Re^{a_2}\right) + \frac{a_3}{1 + a_4 Re^{-a_5}} \text{ with } Re < 3 \times 10^5, \tag{1.7}$$

$$a_1 = 0.15, \quad a_2 = 0.687, \quad a_3 = 0.42, \quad a_4 = 4.25 \times 10^4, \quad a_5 = 1.16. \tag{1.8}$$

This equation is valid for a large range of Reynolds numbers up to the transition to a turbulent boundary layer, which results in a sharp drop of the drag coefficient.

However, ice crystals and snowflakes represent irregular bodies. A recent overview of different correlations for the prediction of the drag coefficient of irregular particles can be found in the work of Roostaee and Vaezi [159]. These correlations are based on different geometric descriptors of the particle shape. The volume equivalent diameter d_eq, the sphericity Φ and the crosswise sphericity $\Phi_\perp$ defined in Equation 1.2 are the most widely used descriptors in these correlations. The crosswise sphericity is evaluated for the projection of the particle onto a plane normal to the direction of the flow.

Numerous studies of the drag of nonspherical particles are available. The most advanced and widely spread models are those of Haider and Levenspiel [69], Ganser [60] and Hölzer and Sommerfeld [81]. These models are based on the volume equivalent diameter as the characteristic length, $d = d_\mathrm{eq}$ and the projected area of a volume equivalent sphere as the reference area, $A_\mathrm{ref} = \pi d_\mathrm{eq}^2/4$. The models of Haider and Levenspiel and Ganser both take the form of Equation 1.7, while the parameters a_1 to a_5 are given as functions of the sphericity Φ.

The model of Hölzer and Sommerfeld accounts for the orientation of the particle by utilizing the crosswise sphericity $\Phi_\perp$. The correlation proposed by Hölzer and Sommerfeld is given by

$$c_\mathrm{d} = \frac{8}{Re\sqrt{\Phi_\perp}} + \frac{16}{Re\sqrt{\Phi}} + \frac{3}{\sqrt{Re}\Phi^{3/4}} + \frac{0.42 \times 10^{0.4(-\log_{10}\Phi)^{0.2}}}{\Phi_\perp}. \tag{1.9}$$

They also specify an alternative equation considering the lengthwise sphericity, which must be obtained from a large number of particle projections onto planes parallel to the direction of the fluid flow. However, since this is difficult to measure in field experiments and it only yields a minor improvement, the formulation given by Equation 1.9 is commonly used.

In recent years, further investigations of the drag of irregular particles have been performed, which include additional geometric descriptors of the particle [185, 116, 9, 192]. However, the complexity of the investigated particles is limited. While single ice crystals can be well approximated by these irregular particles, the shapes of snowflakes are more complex to describe since they represent porous bodies. The flow through the pores of the body can significantly affect the outer flow [26, 15].

Taylor [182] theoretically studied the drag force experienced by a highly porous flat plate. In this study, the porosity is defined as the ratio of the open area to the total area of the plate. Taylor models the mesh as distributed sources in potential

flow, which agrees well for high porosities. Cumberbatch [42] studied the drag of a porous plate by modeling the flow through the pores with Darcy's law. More recently, Steiros and Hultmark [172] extended the model of Taylor to be applicable to lower plate porosities. Masliyah and Polikar [125] investigated the drag of porous spheres and proposed a correlation for a limited range of Reynolds numbers.

Heymsfield and Westbrook [79] proposed a drag model specifically designed for snowflakes. This model is an adaptation of the model of Abraham [1] for the drag of a sphere, which is modified with the roundness measure of Pentland [146] defined as $4A_{\perp}/\pi d_{\mathrm{max}}^2$. The model of Heymsfield and Westbrook uses the maximum dimension as the characteristic length and the particle projection as the reference area. McCorquodale and Westbrook [133] experimentally investigated the drag of 3D-printed snowflakes and suggested a modification of the model of Heymsfield and Westbrook in a later study [134]. Villedieu et al. [189] and Trontin et al. [187] applied a simplification of the shapes of ice crystals to predict the drag coefficient. Aguilar et al. [2] extended this model to snowflakes. In these models, the particle is approximated by a spheroid. The drag coefficient is then calculated from correlations for irregular particles.

Tagliavini et al. [179] computed the drag of individual snowflakes from numerical fluid dynamics simulations and validated the results with experiments using 3D-printed particles. To account for an unknown orientation of the snowflake, the drag coefficient obtained from two orientations was averaged. In a similar study, Tagliavini et al. [180] numerically investigated the wake of a falling snowflake and described the influence of the pores of the particle.

The various existing empirical models for the fall speed of snowflakes do not adequately capture the Reynolds number dependency, which limits their applicability [195]. Furthermore, it is not possible to accurately measure the full three-dimensional shapes of snowflakes, which would be required to evaluate common drag models for irregular particles. The lack of reliable and accurate models makes predicting the dynamics of clouds of snowflakes in an airflow a challenging task and requires further research.

1.2.3 Melting of snowflakes

The melting of ice particles has a major influence on various phenomena associated with icing due to impinging ice crystals or snowflakes. This applies not only to aircraft icing, but also to icing of other structures exposed to snow [148, 53, 169]. For example, the particle shrinks during melting and changes its shape, which affects the particle drag and thus its trajectory. Most importantly though, the melted fraction of the particle determines whether or not it sticks to the substrate upon impact [122, 46]. Furthermore, an adequate modeling of the melting of snowflakes is required for improved weather forecasts. Melting snowflakes in the atmosphere cause errors in precipitation estimates from weather radars [178]. In addition, sleet

formation is determined by snowflake melting. This process withdraws heat from the atmosphere and thus influences the motion of storms [197, 6].

The literature review presented in this subsection is based on the article *Melting of fractal snowflakes: Experiments and modeling* by Köbschall et al. [104], published in the International Journal of Heat and Mass Transfer.

Several effects have to be considered for an accurate description of melting ice particles. Prior to the inception of melting, the ice has to reach the temperature of fusion. This is associated with an increase in sensible heat, while the subsequent melting of the particle is associated with latent heat. The ratio of sensible heat to latent heat is expressed in the Stefan number defined as

$$St = \frac{c_{p,\mathrm{i}}(T_\mathrm{m} - T)}{L_\mathrm{f}}. \tag{1.10}$$

Here $c_{p,\mathrm{i}}$ denotes the specific heat capacity of ice, T the particle temperature, T_m the melting temperature and L_f the latent heat of fusion. In the case of very small Stefan numbers, the required sensible heat can be neglected. Convective heat transfer is usually accounted for by a heat transfer coefficient, which can be obtained from correlations for the Nusselt number [58, 167, 157, 74]. The Nusselt number is defined as

$$Nu = \frac{h_\mathrm{h} d}{k_\mathrm{a}} \tag{1.11}$$

and represents the ratio of convective heat transfer to heat conduction. In this equation h_h denotes the heat transfer coefficient and k_a the thermal conductivity of the fluid, i.e., air in the case of melting ice particles. The Nusselt number is generally a function of the Reynolds number and the Prandtl number

$$Pr = \frac{c_{p,\mathrm{a}} \nu_\mathrm{a} \rho_\mathrm{a}}{k_\mathrm{a}} \tag{1.12}$$

with the specific heat capacity of air $c_{p,\mathrm{a}}$. Due to the analogy between heat and mass transfer, similar correlations can be used for the Sherwood number

$$Sh = \frac{h_\mathrm{m} d}{D_\mathrm{v,a}}, \tag{1.13}$$

which specifies the ratio of convective mass transfer to diffusive mass transfer and is a function of the Reynolds number and the Schmidt number

$$Sc = \frac{\nu_\mathrm{a}}{D_\mathrm{v,a}}. \tag{1.14}$$

Here h_m denotes the mass transfer coefficient and $D_\mathrm{v,a}$ the diffusivity of water vapor in air. The mass transfer coefficient can be used to quantify the evaporation rate, which needs to be considered during the melting of ice particles.

The melting of regular ice particles such as single ice crystals, graupel or hail has been investigated by several researchers. Wind tunnel experiments have been

conducted to investigate the melting of spherical ice particles of different sizes and describe the shedding of meltwater [152, 154]. Multiple theoretical models have been proposed in literature, which are focused on spherical particles. Mason [126] derived a one-dimensional model for the melting of a spherical ice particle. The model assumes that the meltwater forms a liquid layer of uniform thickness around the ice. Mason found good agreement with the results of his laboratory experiments. However, a comparison of this model with the experimental data obtained from wind tunnel experiments of Rasmussen and Pruppacher [152] exhibits a significant deviation. Therefore, Rasmussen et al. [153] proposed an extended model which accounts for internal circulation in the melt water and an eccentric location of the ice core. These effects reduced the predicted duration of melting by approximately 10 % when compared to the model of Mason. Accounting for the increased surface area due to the oblateness of the particle and an adapted heat transfer coefficient due to the flow patterns further decreased the melting duration. When considering these adaptations, the model predictions are in good agreement with the experimental results of Rasmussen and Pruppacher [152].

Hauk et al. [74] investigated the melting of nonspherical ice particles in laboratory experiments and developed a theoretical model for this process. In their experiments Hauk et al. placed the ice particles in an acoustic levitator, which held the particles in a warm airflow. The proposed model takes the particle sphericity into account and makes use of a modified Nusselt number correlation to obtain the heat transfer coefficient. The initial particle sphericity is approximated with the initial crosswise sphericity obtained from a two-dimensional projection. Hauk et al. assume that the sphericity increases linearly with the melted mass fraction. Kintea et al. [98] developed a numerical model to predict the size and shape evolution of melting nonspherical ice particles. This model successfully predicts the cusps, which the particle forms during melting. The model assumes that all meltwater is collected around the midsection of the particle. The model predictions agree well with experimental data of melting spherical and nonspherical ice particles.

These models provide adequate results for the melting of regular ice particles of spherical and nonspherical shape. However, they are not applicable to porous particles such as snowflakes. Knight [102] captured natural partially melted snowflakes and described their morphology. Matsuo and Sasyo [130] investigated the melting of natural snowflakes in a wind tunnel by placing them on a nylon net. Based on their observations, they proposed a semi-empirical model describing the size evolution of the snowflakes. Their approach of fixing the position and orientation of the snowflake with a nylon net enables a detailed observation of the melting snowflake. However, the fibers could affect the melting process and the redistribution of meltwater. In another study Matsuo and Sasyo [131] investigated the influence of evaporative cooling on the melting of snowflakes by varying the relative humidity of the airflow. Fukuta et al. [59] performed wind tunnel experiments with freely suspended snowflakes and proposed a simplified model to better understand

the radar reflectivity of melting snowflakes. This model represents the snowflake as multiple spherical particles arranged in fixed positions. Fukuta et al. assumed a saturated atmosphere and thus neglected evaporation. Another experimental and theoretical study of the melting of falling snowflakes has been performed by Mitra et al. [141]. Here, natural and artificial snowflakes were melted in a vertical wind tunnel by increasing the temperature of the airflow at a constant rate. The model proposed by Mitra et al. approximates the snowflake as an oblate spheroid and makes use of empirical correlations for the particle density and two shape descriptors. Aguilar et al. [3] derived a model for melting snowflakes, which requires fewer empirical correlations. In this model, the snowflake is represented as a spheroid and the bulk density of the particle is obtained from an empirical model. Leinonen and von Lerber [108] studied the melting of snowflakes in a three-dimensional numerical simulation. These simulations show that meltwater gathers in the concave sections of the snowflake. Furthermore, the rough and porous structure of rimed snowflakes appears to absorb a significant volume of meltwater.

While accurate theoretical models for the melting of regular ice particles are available in literature, present models for the melting of snowflakes exhibit a large degree of empiricism. The underlying empirical correlations limit the universality of the models. Furthermore, none of the above mentioned models takes the morphological class of the snowflake into account.

1.2.4 Water transport in ice and snow layers

Ice accretions formed by ice crystal icing or snow represent complex porous structures composed of ice, liquid water and air. Although the exact composition of these ice layers is generally unknown, the role of liquid water in the icing process is indisputable [127, 13, 123]. Liquid water can be supplied to the ice accretion through different mechanisms, such as melting of the accretion on a heated substrate, runback water in the form of rivulets or impinging droplets and partially melted ice particles. Conversely, liquid water can also leak out of the ice accretion. In conditions where the ice particles are fully frozen, the accretion process is influenced by the transport of liquid water through the porous ice layer. Therefore, water transport in granular ice and snow layers is a crucial aspect that needs to be considered to understand icing phenomena.

However, the relevance of water transport in porous ice layers is not only restricted to aircraft icing. The water transport in snow layers is relevant for the prediction of avalanches, the design of water reservoirs in cold regions, the evolution of glaciers and snow accretion on various structures [196, 29, 83, 148, 53].

A major parameter describing a porous medium is its porosity, which is defined as the volume fraction occupied by the voids of the solid matrix [41]. A snow layer can be assumed as a packed bed, which represents a specific type of porous media. The structure of the pores is determined by the geometry of the particles

comprising the medium. The particle shape is an essential factor affecting the range of porosities that these particles can form. For instance, the minimum and maximum porosity of ordered packings of monodisperse spheres are 0.26 and 0.48, respectively [207]. For randomly packed monodisperse spheres, different porosities are obtained in experiments. Depending on the shape and size distribution of particles, a wide range of porosities can be obtained [31].

Two scenarios of water transport in ice and snow layers can be distinguished: saturated flow and unsaturated flow. Saturated flow involves the transport of a single phase through a porous medium where the voids are completely filled with the fluid. Conversely, unsaturated flow refers to multiphase flow, where the pores are only partially occupied by liquid water.

Single phase flow through a porous medium is well described by Darcy's law given by [41]

$$u_* = -\frac{\kappa \nabla p}{\nu \rho}, \tag{1.15}$$

which provides the apparent velocity u_*, also referred to as Darcy flux, specifying the volumetric flux as a function of the pressure gradient ∇p. In this equation, κ denotes the permeability of the medium, which is dictated entirely by the pore structure [41].

Darcy's law has been extended to unsaturated flow by accounting for mass conservation. This equation is commonly known as Richards' equation after the work of Richards [156]. Instead of a permeability that is only determined by the pore structure, the permeability in Richards' equation is a function of the saturation of the pores. This equation describes a diffusion-like behavior of water transport. For further details on Richards' equation, the book by Szymkiewicz [177] is recommended.

Liquid in a porous medium is subjected to various forces, such as viscous, inertial, gravitational and capillary forces. The process of absorption of a liquid by a porous medium is referred to as imbibition [41]. Imbibition is dominated by capillary forces resulting from the wettability of the materials. Due to the hydrophilic nature of ice, imbibition plays an important role in the water transport in granular snow and ice layers [101].

Lucas [117] and Washburn [194] theoretically and experimentally investigated imbibition in saturated flow conditions. The theoretical model is based on an analytical solution for cylindrical capillaries. They then used the identified behavior to model the imbibition into a porous body by approximating the medium as a bundle of very small cylindrical capillaries. Inertia and gravity effects are ignored in this approach. Multiple researchers have identified deviations from this behavior in experiments and proposed improved models for liquid rising in circular capillaries [170, 76, 80]. While this process is driven by capillary forces, different stages can be distinguished by the dominating counter-acting force [70, 56, 57, 164]. Upon initial contact, the capillary rise dynamics are dictated

by inertial forces. Subsequently, the influence of viscous effects increases as the wetting front decelerates. Following the viscous dominated stage, gravitational effects gain importance as the liquid column approaches an equilibrium height.

The case of capillaries with circular cross-sections corresponds to the simplest possible imbibition process. However, in porous media, such as granular ice and snow layers, the pores exhibit a far more complex geometry with angular cross-sections, rough walls and varying diameters. In these complex shaped pores, the wetting fluid flows along the edges and the rough wall of the pores [27]. The edges and roughness of such a medium create a network of interconnected surface grooves, which allows the wetting phase to remain continuous and mobile in the porous structure. Consequently, the pores of snow layers are not fully saturated and the contribution of air inclusions has to be accounted for.

Various flow phenomena have been identified in complex porous media. In the following, a short overview of different phenomena that can occur during the imbibition of liquid water into granular ice or snow layers is presented. The fluid flow along the corners of the pore network and thus bypassing the pore bodies is referred to as corner flow [208]. The nonwetting phase can be trapped in the pore body by the imbibed wetting phase, which is referred to as „snap-off“ [41]. Another flow pattern is cooperative pore filling, where liquid enters the pores from several adjacent pores, which results in a flat wetting front [17]. Due to instabilities in the wetting front, finger-like structures can emerge and propagate through the porous medium [193].

Literature on the transport of liquid water in ice accretions is sparse. Currie and Fuleki [44] studied the liquid fraction of ice accretions grown at positive wet bulb temperatures, i.e., with partially melted particles. However, they did not quantify the transport of liquid water in the accretion. Trontin and Villedieu [186] proposed an accretion model for ice crystal icing which includes an empirical model for the absorption of liquid water. Kintea et al. [99] developed a numerical model for the transport of liquid water in ice accretions based on a diffusion-like equation proposed by Luikov [118]. Kintea et al. successfully applied this model to predict shedding events. The model of Luikov requires a model parameter, for which Kintea et al. assumed an arbitrary value between those corresponding to gypsum and concrete.

Different researchers studied the transport of liquid water through snow layers. Early investigations by Gerdel [65] on water transmission through snow showed that the water storage capacity of snow is initially high but rapidly decreases once a drainage network is established. The velocity of the wetting front was observed to be higher for denser snow layers. Colbeck [32] proposed a model for the water transport in snow layers based on Darcy's law. In a later study, the effect of capillarity on water transport has been investigated [33]. The results indicated that gravity dominated the flow under the analyzed conditions, with capillary forces playing a minor role. However, for small fluxes, the role of capillary forces

significantly increased. In a subsequent study, Colbeck [34] further extended the previous model by accounting for additional effects and observed that flow in the form of fingers advancing down flow channels contributed significantly to the total flow. Conway and Benedict [37] conducted measurements on liquid water transport through subfreezing snowpacks. Schneebeli [162] and Waldner et al. [191] used dye to visualize flow patterns in artificial snow layers and identified two distinct regimes referred to by matrix flow and preferential flow. Matrix flow is described as being dominated by capillary flow in the homogeneous snow matrix, whereas preferential flow occurs in zones with microstructural defects which result in liquid fractions close to saturation. Avanzi et al. [7] observed an increase in the size of fingers in the flow pattern with increasing grain size. Capillary rise in snow layers has been studied experimentally and numerically by Coléou et al. [35]. The experiments were evaluated by optically analyzing slices of snow samples. Here they identified an influence of porosity and grain size on the height of capillary rise.

Most of these investigations of water transport in snow layers focus on large scale water distributions. Therefore, it is unclear to what extent these findings are applicable to the water transport on smaller scales relevant to icing of aircraft or structures. The large span in porosity ranging from compact ice accretions to light snow layers further complicates the generalizability of findings. Similarly, the effects of ice crystal grain size are still not fully understood [65, 37, 35, 162, 191]. These effects of the properties of granular layers on the wetting process and liquid distribution require further investigation. In addition, the influences of different boundary conditions need to be included in experimental studies.

While models for flow in porous media exist, they heavily rely on accurate parameters specific to the properties and composition of the porous medium and fluid [41, 156, 118]. These parameters require further experimental studies in order to improve the prediction of icing phenomena [99].

1.2.5 Ice accretion

Ice accretion in ice crystal icing is commonly modeled based on a mass balance for the ice layer, originally proposed by Messinger [136] for icing due to supercooled water. This model has since been extended to ice crystal icing by multiple researchers [203, 189, 186]. The mass balance incorporates several effects, including the mass flux of runback liquid water (i.e., rivulets of liquid water on the substrate), the mass flux of deposited ice and liquid from impacting particles, a mass flux due to erosion of the ice accretion and evaporative mass flux.

The concentration of ice crystals is specified in terms of ice water content (IWC), which denotes the ice mass in a unit volume of incoming air. Analogously, the liquid water content (LWC) specifies the liquid mass per flow volume and the total water content (TWC) comprises liquid and solid phase. The ratio of liquid water content to total water content is referred to as melt ratio.

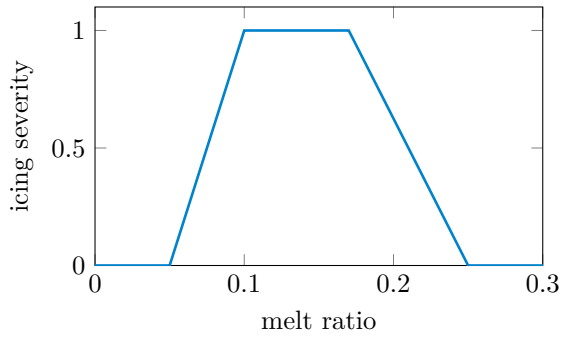

Figure 1.6: Qualitative illustration of the icing severity as a function of melt ratio in the ice cloud according to Currie et al. [46]. Icing severity exhibits a plateau in a certain range of melt ratios.

Ice crystals impacting on a surface can either stick or bounce off, and the impact can also cause erosion of the ice layer. Currie et al. [46] studied ice accretion at positive wet bulb temperatures, where the ice particles are partially melted, and proposed a simple model for the mass fraction of the impacting ice cloud that adheres to the surface, which is referred to as the sticking efficiency. This parameter is crucial in modeling ice crystal icing and has been the subject of many subsequent studies [189, 186, 123].

The accretion of ice due to ice crystals and snowflakes is driven by the presence of liquid water [128, 46]. Ice crystals impacting on a cold dry rigid wall only leave a small amount of residual ice on the substrate [155]. Therefore, the sticking efficiency is determined by the availability of liquid water. While literature on the sticking of impacting snowflakes at conditions relevant to aircraft icing is sparse, the effects can be expected to be qualitatively similar.

Two sources of liquid water can be considered: liquid water carried by the airflow to the substrate and meltwater generated by the melting of impacting particles and their residual ice mass on a heated surface.

For mixed-phase clouds, the sticking efficiency has been found to be a function of the melt ratio. Struk et al. [176] and Currie et al. [46] report that the icing severity, which includes sticking efficiency and erosion effects, exhibits a maximum on a plateau at certain melt ratios. This is qualitatively presented in Figure 1.6, which highlights the importance of an accurate prediction of the melted mass fraction of ice particles.

The influence of Mach number, total water content and air pressure has been investigated experimentally at mixed-phase conditions [47, 46, 45]. These studies have shown that the sticking efficiency is approximately independent of Mach number and total water content at normal impacts of ice crystals. However, a dependency exists at oblique impact angles [46]. Furthermore, an influence of particle size has been identified at high Mach numbers where ice only accreted

for very small particles [45]. A further influence on the accretion is given by the collection efficiency. This quantity describes the fraction of ice crystals in a certain cross-section of the incident flow that impacts onto the substrate. This is determined by the particle trajectories. The coupled effects of collection efficiency, sticking efficiency and erosion on the growth rate of an ice accretion and its shape are discussed in detail in the work of Baumert et al. [13].

In addition to these experiments in icing wind tunnels, experimental studies have been performed with a focus on the physical phenomena on small scales. Hauk et al. [73] and Reitter et al. [155] investigated the impact of ice particles onto dry solid walls. Furthermore, Hauk [72] also investigated the impact onto heated walls and walls covered by a liquid film.

Villedieu et al. [189] modeled the sticking efficiency based on the assumption of a liquid film present on the substrate. Malik et al. [123] conducted accretion experiments with a heated substrate and proposed an empirical model for the sticking efficiency. This model is fitted to the experiments such that the numerically predicted temperature decrease of the substrate agrees with the experimental measurements. The model is specified as a function of the liquid volume fraction at the impact location. However, this data is only available as a result from the numerical simulations and has not been measured in the experiments.

In the numerical studies mentioned above, erosion is commonly accounted for by implementing an erosion efficiency, which is given as a function of the tangential velocity component of the impacting ice crystals, the liquid fraction of the accretion and the shape of the accretion [13, 186, 123].

While the importance of liquid water in the framework of snow and ice crystal icing is well known, literature on the liquid content and its distribution in ice accretions is sparse. The investigation of these quantities is obstructed by a lack of suitable measurement instruments. The resulting knowledge gap impedes the development of advanced physical models for the prediction of ice accretion.

1.2.6 Measurement of liquid fraction

The characterization of liquid fractions in porous media is relevant not only in the framework of aircraft icing but also in various other fields such as hydrology, agriculture, food processing and others [23, 63, 151]. The measurement of the liquid fraction in granular ice layers is relevant for the estimation of the properties of snow layers regarding avalanche prediction, surface albedo and reservoir management [38, 93, 67, 92]. Numerous measurement techniques exist for the quantification of liquid fractions in soils. These techniques include gravimetric measurements, neutron moisture gauges, nuclear magnetic resonance measurements, microwave-based approaches and approaches based on changes in conductivity and dielectric constant [206, 188, 144, 198, 19, 174]. However, many of these measurement techniques are not suitable for the measurement of liquid water in granular ice and

snow layers, since they either require heating the material or they are incapable of differentiating between liquid and solid water. Furthermore, a robust, nonintrusive and nondestructive method is desired, which is capable of capturing time-resolved values. Therefore, calorimetry is unsuitable since it requires melting of the specimen. Furthermore, impurities in water significantly alter its conductivity, which renders a measurement based on the electrical resistance ineligible [184].

Measurements based on the dielectric properties of the wet porous medium provide several benefits when compared to the alternative approaches presented above. These measurement techniques commonly derive the properties of the medium from the measurement of a capacitance of two electrodes, which is described below. Another technique based on the dielectric constant of the medium is provided by time domain reflectometry, which has also been used to measure the liquid content of snow [171, 119]. This technique and the progress made are described in detail in the work of He et al. [75] and are not part of the present work.

Capacitive measurements

Capacitive measurements, based on the dielectric properties of a medium, are a promising method for measuring liquid fraction and fulfill the requirements mentioned above. In the following, a short overview of the application of capacitive measurements for determining the liquid fraction is presented.

The capacitance of a system is determined by its geometry and the dielectric properties of the medium surrounding the conductors. Water exhibits a relatively high dielectric constant, or relative permittivity, which is a consequence of the dipolar nature of the water molecule. Due to the large difference in relative permittivity between liquid water and other common materials, a capacitive sensor is well suited for measuring the liquid fraction of a porous medium.

Various instruments based on this principle have been proposed for soil moisture measurement and similar sensors are widely used [8, 137, 184, 48, 199]. This technique has also been applied to measure the liquid content of snow layers. Several instruments with different electrode geometries are described and compared in the work of Denoth et al. [50]. A widely used device based on this technique has been developed by Denoth [49]. This device consists of a data acquisition system connected to a thin plate, which incorporates the electrodes of the sensor. Inserting this plate in the snow specimen allows measuring its liquid fraction. A similar device has been constructed by Sihvola and Tiuri [165]. The device is referred to as snow fork due to the two parallel rods, which serve as electrodes to the instrument. These devices have been used to measure the liquid water profile in snow layers by inserting the electrodes at different positions in the snow. However, the spatial and temporal resolution of these measurements is limited by the geometry of the sensor electrodes and the procedure, which requires repositioning of the sensor. These devices are calibrated for a limited range of liquid volume fractions, which typically does not exceed 15 % [183].

Currie and Fuleki [44] developed an instrument for the quantification of liquid water in ice accretions due to ice crystal icing. The instrument is based on the measurement of the capacitance of two electrodes embedded in the test article. Since the sensor does not provide the distribution of liquid water in the accretion, this approach is limited to adiabatic substrates and positive wet bulb temperatures, where a uniform distribution of liquid water in the ice accretion can be assumed. Currie and Fuleki conducted wind tunnel experiments with the sensor and obtained liquid volume fractions of the ice accretion in the range of 25 % to 33 % for cloud melt ratios ranging from approximately 10 % to 20 %. However, the liquid content and its distribution in ice accretions formed by fully frozen particles impacting onto a heated substrate remains unknown and cannot be measured with existing wind tunnel instrumentation.

Dielectric properties of wet ice layers

To quantify the liquid volume fractions present in granular ice and snow layers using capacitive measurements, a relationship between the relative permittivity of the medium and the corresponding liquid volume fraction is required.

The wet ice layer represents a mixture of three phases: ice, air and liquid water. These components exhibit different relative permittivities, which are a function of the frequency of the electric field. The dielectric spectra of ice, liquid water and air are illustrated in Figure 1.7. The relative permittivity of liquid water is approximately 88 at 0 °C and excitation frequencies of less than 1 GHz. This value is significantly larger than that of the other two components. Ice exhibits a relative permittivity of approximately 3.2 at frequencies above 100 kHz while air has a relative permittivity close to unity. Since the relative permittivity of air is close to that of ice and the volumetric fraction of air is usually lower than those of the other two phases, the influence of air on the relative permittivity of the mixture is often neglected. Therefore, the effective relative permittivity of the wet ice layer is commonly assumed to be only a function of the liquid volume fraction.

Ambach and Denoth [4] studied the relative permittivity of snow layers with liquid volume fractions up to 12 %. The relative permittivity was measured in a parallel plate capacitor and the liquid fraction was determined by calorimetry. Furthermore, Ambach and Denoth obtained fitting parameters for theoretical models from their measurements.

Currie and Fuleki [44] measured the relative permittivity of wet granular ice layers by adding liquid water to a container with ice crystals, compressing the mixture and measuring the permittivity with two concentric electrodes in the container. Subsequently, the liquid volume fraction was measured by placing the ice layer in a calorimeter.

Many researchers have proposed correlations for the effective dielectric properties of mixtures. Lichtenecker [112] proposed a power law in which the exponent is determined by the shape of the inclusion, with theoretical justifications for

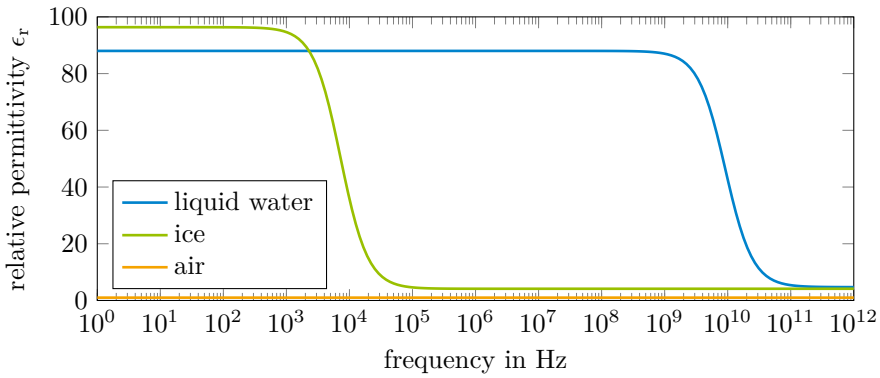

Figure 1.7: Relative permittivities of liquid water and ice as a function of frequency. The curves have been calculated based on data of von Hippel [190] and Johari and Whalley [87].

spherical and cylindrical inclusions [166]. Further mixing laws based on physical derivations were proposed by Maxwell Garnett [132] and extended by Bruggeman [25]. The significant difference between these two models is that the Maxwell Garnett formula describes a host and a guest phase with a clear hierarchy and it neglects the interaction between the inclusions. In contrast, the Bruggeman formula puts the inclusions against the effective medium and is thus symmetrical, i.e., it does not differentiate between a host and a guest phase [166]. The model of Bruggeman is often also associated with the work of Polder and van Santeen [147].

In the Bruggeman model the effective relative permittivity $\varepsilon_{\mathrm{r,B}}$ is implicitly given as a function of the liquid volume fraction v_{liq} by

$$\varepsilon_{\mathrm{r,B}} = \varepsilon_{\mathrm{r,i}} + \frac{v_{\mathrm{liq}}}{3}(\varepsilon_{\mathrm{r,w}} - \varepsilon_{\mathrm{r,i}}) \sum_{j=x,y,z} \frac{\varepsilon_{\mathrm{r,B}}}{\varepsilon_{\mathrm{r,B}} + \zeta_j(\varepsilon_{\mathrm{r,w}} - \varepsilon_{\mathrm{r,B}})} \tag{1.16}$$

where $\varepsilon_{\mathrm{r,i}}$ and $\varepsilon_{\mathrm{r,w}}$ denote the relative permittivity of ice and water, respectively, and $\boldsymbol{\zeta}$ the depolarization factors of the inclusions in the three dimensions in space for which $\zeta_x + \zeta_y + \zeta_z = 1$ must be valid. Ambach and Denoth [4] suggested the values $\boldsymbol{\zeta} = [0.070, 0.465, 0.465]$ based on their measurements with wet snow in the range of $6\,\% < v_{\mathrm{liq}} \leq 12\,\%$.

At high liquid fractions above the so-called percolation threshold, the liquid inclusions are connected and provide a path through the ice layer. The Bruggeman model considers the inclusions to be in an effective mean field, which is no longer the case close to this percolation threshold and above the percolation threshold [205, 100]. The large clusters formed by the inclusions lead to an effective relative permittivity, which is significantly larger than that predicted by common effective medium approximations. Figure 1.8a illustrates an ice layer below the percolation threshold and Figure 1.8b shows clusters of pores with liquid water associated with percolation.

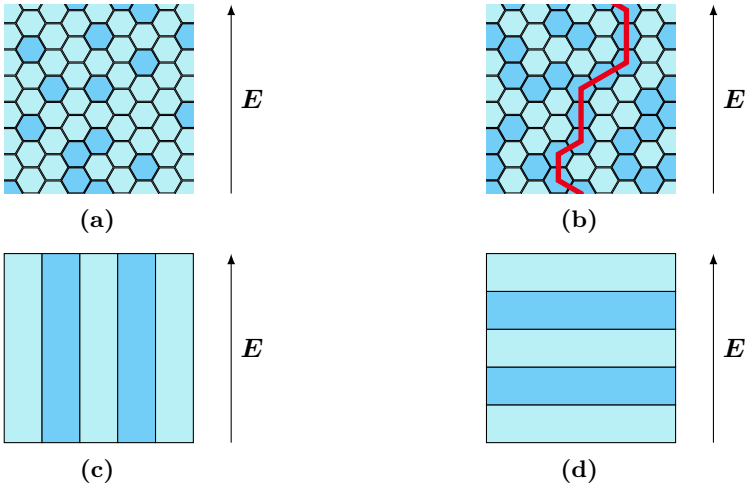

Figure 1.8: A granular ice layer with a liquid volume fraction below the percolation threshold (a) and a wet ice layer with percolation (b). Limiting cases for the effective medium approximation given by a laminate parallel to the electric field (c) and a laminate perpendicular to the electric field (d).

Close to the percolation threshold the inclusions form clusters, which also result in a deviation from models such as that of Bruggeman.

An upper and a lower bound for the relative permittivity of a mixture can be defined by considering the mixture as a laminate. These bounds are commonly called Wiener bounds after the work of Wiener [200]. The upper bound is given by a laminate, which is oriented parallel to the electric field, which is illustrated in Figure 1.8c. The effective relative permittivity of this laminate is given by

$$\varepsilon_{\mathrm{r,par}} = (1 - v_{\mathrm{liq}})\varepsilon_{\mathrm{r,i}} + v_{\mathrm{liq}}\varepsilon_{\mathrm{r,w}}. \tag{1.17}$$

Similarly, the lower bound is defined by a laminate perpendicular to the electric field, which is illustrated in Figure 1.8d. This corresponds to the layers being connected in series, resulting in

$$\frac{1}{\varepsilon_{\mathrm{r,ser}}} = \frac{1 - v_{\mathrm{liq}}}{\varepsilon_{\mathrm{r,i}}} + \frac{v_{\mathrm{liq}}}{\varepsilon_{\mathrm{r,w}}}. \tag{1.18}$$

Hashin and Shtrikman [71] derived bounds to the effective relative permittivity of mixtures that can be considered statistically isotropic on the macroscopic scale. These bounds are narrower than the Wiener bounds. For wet granular ice layers, the upper bound is given by the liquid phase forming a percolation cluster with spherical inclusions of ice. The effective relative permittivity derived by Hashin and Shtrikman for this configuration is given by

$$\varepsilon_{\mathrm{r,HSU}} = \varepsilon_{\mathrm{r,w}} + \frac{1 - v_{\mathrm{liq}}}{(\varepsilon_{\mathrm{r,i}} - \varepsilon_{\mathrm{r,w}})^{-1} + \frac{v_{\mathrm{liq}}}{3\varepsilon_{\mathrm{r,w}}}}. \tag{1.19}$$

Analogously, the lower bound is given by switching the phases, i.e., the ice forms the percolation cluster with spherical inclusions of liquid water. The effective relative permittivity of this lower bound is then given by

$$\varepsilon_{\mathrm{r,HSL}} = \varepsilon_{\mathrm{r,i}} + \frac{v_{\mathrm{liq}}}{(\varepsilon_{\mathrm{r,w}} - \varepsilon_{\mathrm{r,i}})^{-1} + \frac{1-v_{\mathrm{liq}}}{3\varepsilon_{\mathrm{r,i}}}}. \tag{1.20}$$

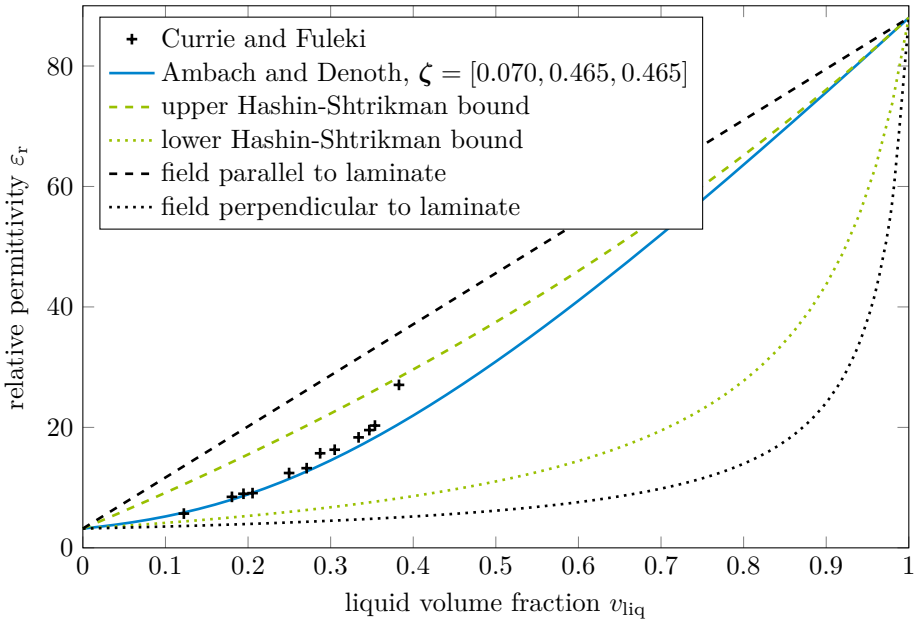

Figure 1.9: Experimental results from Currie and Fuleki, the prediction of the model of Bruggeman with depolarization factors from Ambach and Denoth and different bounds for dielectric mixing. The upper and lower Wiener bounds correspond to a laminate parallel to the electric field and a laminate perpendicular to the electric field.

In Figure 1.9, the experimental data of Currie and Fuleki is shown in comparison to the Bruggeman model with the depolarization factors suggested by Ambach and Denoth. In addition, the above listed bounds are depicted. It can be concluded that the fit of Ambach and Denoth – which was obtained with data of up to 12 % liquid volume fraction – agrees well with the data at low liquid fractions. However, with increasing liquid fraction, the experimental data differs from the fitted model. The sudden increase at the highest experimental liquid fraction is attributed to percolation [44]. The values are bounded by the Hashin-Shtrikman bounds.

Due to the complexities associated with clustering and percolation, no general model for the effective relative permittivity of a mixture, which is valid for the full range of liquid volume fractions, is available.

1.3 Objectives and outline of this thesis

Icing caused by ice crystals and snowflakes entails various physical phenomena that need to be accounted for to accurately predict aircraft icing and mitigate the associated risks in the design process of aircraft and aircraft engines. However, the involved mechanisms are not fully understood and require further research. Two major challenges are the prediction of transport processes of airborne snowflakes as well as the water transport in the ice accumulation, both of which are key mechanisms for snow and ice crystal icing.

The present thesis addresses these topics in two parts. The first part covers the drag and melting of snowflakes and the second part focuses on water transport in porous ice layers. Each of the investigated phenomena requires a dedicated experimental setup, which is described in detail in the corresponding chapter.

In the first part on airborne particles, snowflake drag and melting are investigated. The aim of these studies is to enable an enhanced prediction of the trajectory and the state of the particle prior to impact. While the experimental findings and theoretical models are developed for snowflakes, the results are presented in a way that allows to generalize the key findings to enable their application to different types of ice particles.

Chapter 2 starts with an experimental study of the drag coefficient of artificial snowflakes. A shape simplification based on a convex hull approximation is proposed to grasp the dominating geometrical features of complex shaped snowflakes. In a further step to reduce the required information for the prediction of the drag coefficient, correlations for the estimation of the relevant three-dimensional geometric descriptors from two-dimensional projections are developed.

Chapter 3 comprises an experimental and theoretical study of snowflake melting. In the conducted experiments, laboratory-generated snowflakes are suspended in an acoustic levitator and melted in forced convection. Based on the experimental findings, a theoretical model for the prediction of snowflake melting is proposed and subsequently validated with the experimental results.

The second part of this thesis is devoted to water transport in porous ice layers. Although liquid water has a preeminent role in icing induced by snow and ice crystals, only little is known about the water content and its distribution in ice accretions.

To address this knowledge gap, **chapter 4** presents an experimental study of imbibition into an initially dry melting granular ice layer. In this chapter, a capacitive sensor is developed, which is capable of measuring the space and time resolved liquid content in a porous medium. Various influences on the water transport are investigated.

To more realistically simulate icing, **chapter 5** examines the water content of

ice layers grown in an icing wind tunnel. Motivated by the results of the previous chapter, a novel capacitive sensor is designed to nonintrusively quantify the liquid distribution in the accretion. Water distribution and growth rate of the ice layer are investigated at different experimental conditions and the relationship between liquid fraction and ice layer growth is examined.

Finally, **chapter 6** summarizes the findings of this thesis and provides an outlook for future studies to answer remaining questions.

Part I

Airborne snowflakes

2 Drag coefficient of snowflakes

Numerical tools for the prediction of icing require trajectory calculations for ice crystals and snowflakes. Both types of particles have an irregular shape, which complicates determining their drag coefficients. Especially snowflakes have a highly complex and porous geometry. Simple correlations for the terminal velocity of snowflakes cannot capture the full dependency of the drag force on the Reynolds number. Other models often fail in the Stokes regime at low Reynolds numbers. Moreover, the exact three-dimensional geometry of natural snowflakes is generally unknown and cannot be measured in field experiments. Therefore, a better understanding of the drag of snowflakes and the relevant geometric descriptors is needed.

This chapter first presents an experimental study of the drag of 3D-printed snowflakes. Second, a simplification of the particle shape is proposed, which significantly reduces its complexity and yields improved predictions of the drag. Subsequently, a method for estimating the three-dimensional descriptors of this simplified geometry from two-dimensional projections is proposed. Finally, this method is applied to a generated data set of synthetic snowflakes and the obtained terminal velocity is compared to measurements of natural snow.

This chapter is based on the article *Geometric descriptors for the prediction of snowflake drag* by Köbschall et al. [103] published under CC BY 4.0. The original contents have been edited for this work.

2.1 Experimental methods

The experimental investigation of snowflake drag requires a variety of snowflakes to study and an experimental setup that enables the quantification of the drag coefficient. This section describes the method used to generate the snowflakes, the setup in which their drag force is measured and the post-processing algorithm applied to determine particle orientation.

2.1.1 Generation of three-dimensional models of snowflakes

A detailed investigation of the drag coefficient of snowflakes demands knowledge of the exact three-dimensional geometry of the utilized particles. However, this is not feasible for natural snowflakes. Furthermore, determining the drag force from experiments requires the freestream velocity and the particle mass, which are difficult to measure in field experiments. Therefore, the present study utilizes digital

models of snowflakes to produce artificial snowflakes by additive manufacturing. These artificial snowflakes are then used in the experimental setup to measure the drag coefficient.

The digital models are generated using a code that was developed by Leinonen et al. [109]. In this code, first, numerous individual ice crystals are created. Second, these monomers are stochastically combined to larger aggregates. Third, the snowflakes are subjected to riming. Riming is determined by droplets colliding with the snowflake on its route through the atmosphere, which is quantified with the liquid water path.

Snowflakes occur mostly at temperatures close to 0 °C, where dendritic ice crystals dominate at high supersaturations. Therefore, the present study focuses on aggregates composed of dendritic ice crystals. The number of monomers in the investigated aggregates varies from 3 to 25 individual crystals. Furthermore, the liquid water path extends from $0.1\,\mathrm{kg\,m^{-2}}$ to $0.7\,\mathrm{kg\,m^{-2}}$. This corresponds to a range from barely rimed snowflakes up to highly rimed snowflakes. A further increase in liquid water path would result in particles that would be classified as graupel rather than snowflakes. Exemplary digital models of the utilized snowflakes with different parameters are depicted in Figure 2.1. The morphology of these digital models appears similar to that of natural snowflakes. The utilized parameter ranges result in a large variety of different particles for the investigation of the drag and the relevant geometric descriptors of snowflakes.

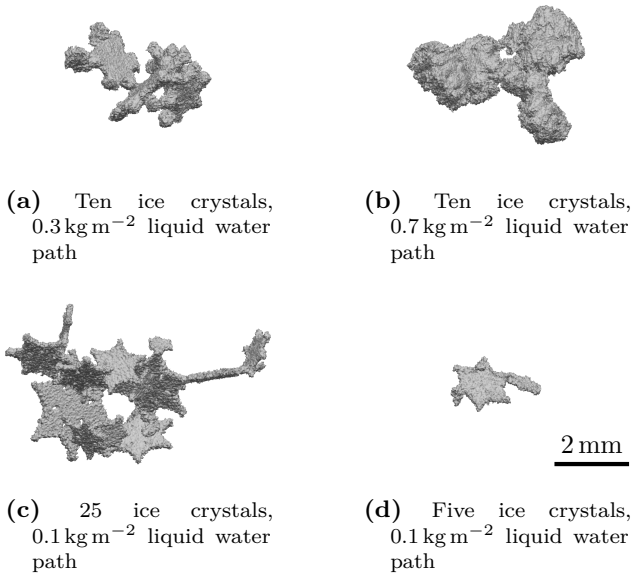

(a) Ten ice crystals, $0.3\,\mathrm{kg\,m^{-2}}$ liquid water path

(b) Ten ice crystals, $0.7\,\mathrm{kg\,m^{-2}}$ liquid water path

(c) 25 ice crystals, $0.1\,\mathrm{kg\,m^{-2}}$ liquid water path

(d) Five ice crystals, $0.1\,\mathrm{kg\,m^{-2}}$ liquid water path

Figure 2.1: Exemplary digital models of snowflakes showing the variety of the generated flakes. While all snowflakes are composed of dendritic ice crystals, the number of monomers and the riming determined by the liquid water path have been varied.

For the experimental investigation, 78 of the generated three-dimensional models are fabricated by selective laser sintering of polyamide powder. The utilized machine accurately recreates structures down to 100 µm. In order to achieve a sufficient level of detail in the printed flake, the digital models were scaled up by a factor of five. In Figure 2.2, a comparison of an upscaled digital model and the manufactured model for the experiments is shown.

2.1.2 Experimental setup

The experiments are conducted in a liquid container to match the Reynolds number of natural snowflakes. The container is equipped with a mechanism to release the snowflakes, a temperature sensor and two light sources and two cameras. Figure 2.3 illustrates the experimental setup for the measurement of the snowflake terminal velocity from which the drag coefficient is obtained.

The container is made of acrylic glass to allow optical access from all sides. The container has a cross-section of 0.4 m × 0.4 m and the liquid level is 0.6 m above the initial position of the snowflake. Water–glycerol mixtures are used to adjust the Reynolds number to match the Reynolds number of falling natural snowflakes. To broaden the range of Reynolds numbers, two different mixing ratios were utilized. The liquid temperature is measured to correct the viscosity of the mixture. The investigated Reynolds numbers are in the intermediate regime in the order of 10 to 10^3.

Prior to the start of the experiment, the artificial snowflake is fixed to the bottom of the container and the liquid is given sufficient time to settle. Subsequently, the release mechanism is triggered and the particle rises up due to buoyancy. Two orthogonal cameras capture the rise of the snowflake with shadowgraphy.

2.1.3 Post-processing

The captured videos are post-processed with regard to the terminal velocity of the snowflake and its orientation. The artificial snowflake is at its terminal velocity when it enters the field of view of the two cameras. Therefore, the particle velocity is constant and can be accurately obtained by linear regression of the particle centroid position. The drag force F_d can then be calculated from the equation of motion given by

$$m\frac{\mathrm{d}u}{\mathrm{d}t} = 0 = (V\rho - m)g - F_\mathrm{d}. \tag{2.1}$$

Since the particle rises on an approximately straight, vertical trajectory, the equation of motion is considered one-dimensional. In this equation, m denotes the mass of the artificial snowflake, V is its volume, u is its relative velocity, ρ is the fluid density, t is time and g is gravitational acceleration. Thus, the drag coefficient

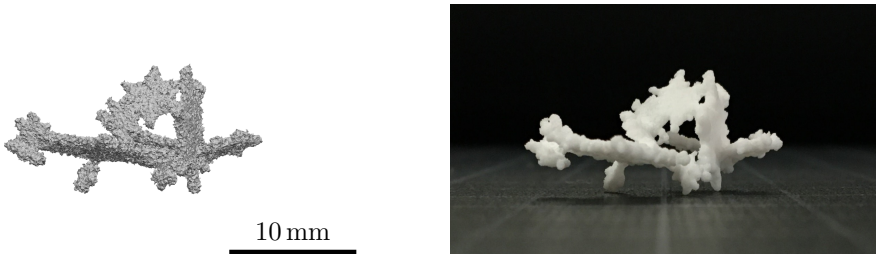

(a) Three-dimensional digital model

(b) Model produced by additive manufacturing

Figure 2.2: Comparison of an exemplary three-dimensional digital model of a snowflake and the resulting 3D-printed particle for the experimental investigation. The snowflake has been scaled up by a factor of five to enable an adequate recreation of the smallest structures of the flake. The depicted snowflake consists of 15 dendritic ice crystals and was subjected to a liquid water path of $0.1\,\mathrm{kg\,m^{-2}}$, which resulted in only slight riming of the particle.

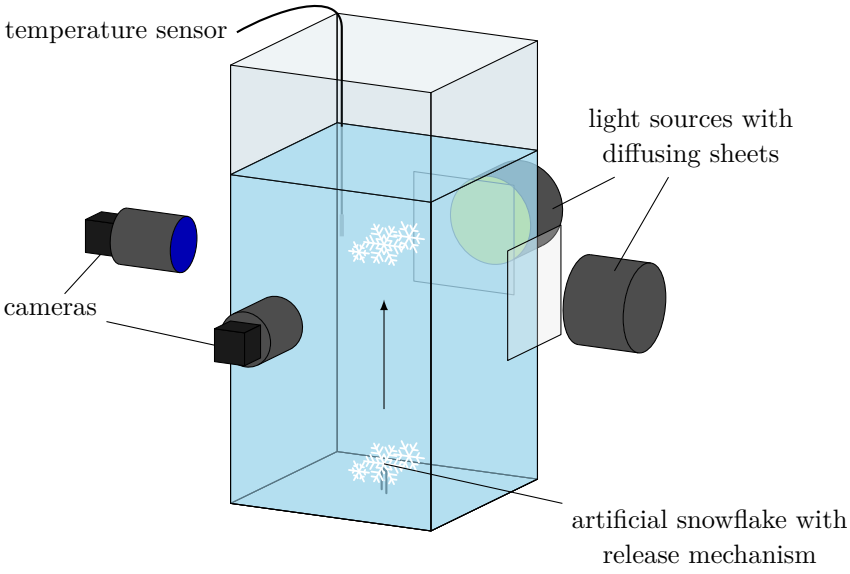

Figure 2.3: The experimental setup comprises a container filled with a glycerol–water mixture, a temperature sensor, two light sources, diffusing sheets and cameras. The artificial snowflake is fixed to the bottom of the container prior to the experiment. Upon release, the snowflake rises through the field of view of the cameras at its terminal velocity.

is obtained from

$$c_{\mathrm{d}} = \frac{2(V\rho - m)g}{\rho A_{\mathrm{ref}} u^2} \tag{2.2}$$

with a reference area A_{ref}.

The particle orientation is determined by matching the projection of the digital snowflake model with the projection captured by the camera. The three-dimensional model of the snowflake is rotated in a stepwise manner around all three axes. For each step, the projection of the model is compared with the binarized video frame. A refinement is performed around the orientation with maximum agreement. This procedure yields the orientation of the artificial snowflake during its motion. The projection of the particle in the direction of flow can then be measured from the digital model. This enables the calculation of the crosswise sphericity defined in Equation 1.2 on page 5. The volume equivalent diameter and the sphericity of the particle can be calculated from the digital model.

2.2 Results on the orientation and drag coefficient of snowflakes

The orientation of falling snowflakes affects their drag and thus their fall speed. Furthermore, the particle orientation is an important input required to obtain the radar reflectivity of snow clouds. Therefore, it is necessary to analyze the gathered data set with regard to a potential preferred orientation of the particle. Hence, three orthogonal projections of the particle are defined: the projection in the streamwise direction resulting in a projected area $A_{\perp}$ and two orthogonal side views as they are observed from the two cameras in the experimental setup. The two projected areas measured from the cameras are denoted by $A_{\parallel,1}$ and $A_{\parallel,2}$. Figure 2.4a illustrates two projections of the particle: The projection on the plane normal to the relative velocity and a projection on a plane parallel to the fluid flow. A comparison of the projected areas from the experiments is shown in Figure 2.4b. The experimental results show that the area normal to the direction of flow is larger than the area observed from the side views in nearly all experimental runs. This indicates that the particle is orienting itself such that the area normal to the flow is maximized. Once the particles assumed this orientation, their motion appeared rather stable. However, several artificial snowflakes showed a rotation around the vertical axis, i.e., the direction of the relative velocity. This observation is limited to steady state conditions and the experiments do not represent snowflakes falling through turbulent air which can affect the stability of the particle orientation. Furthermore, Willmarth et al. [201] showed that the stability of the orientation of a disk in a fluid flow is determined by a dimensionless moment of inertia. While snowflakes exhibit geometries that are far more complex than disks, this effect can also affect the stability of the orientation of snowflakes in a flow.

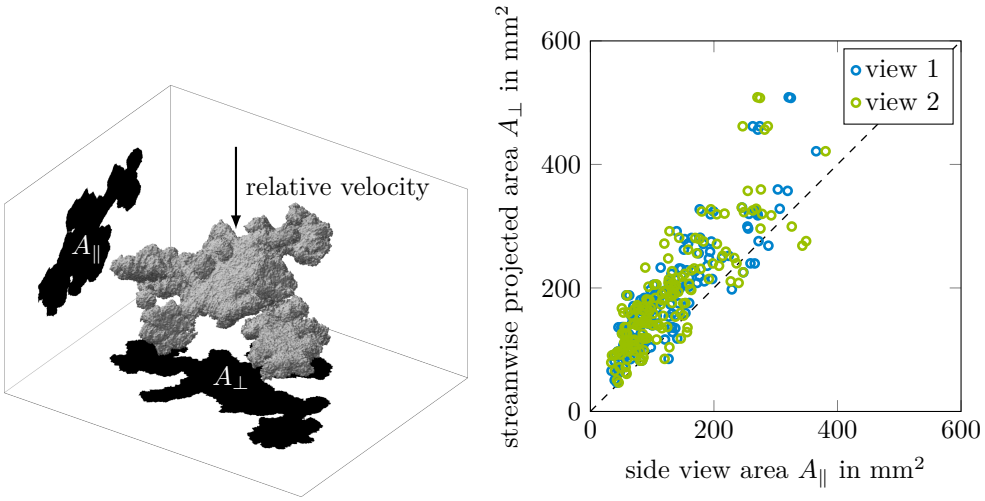

(a) Illustration of the area projected in streamwise direction and an area projected in a direction perpendicular to the flow

(b) Area projected in the direction of flow versus the areas seen from two perpendicular side views

Figure 2.4: Orientation of particles observed in the experiments. The area $A_\perp$ is measured from a projection on the plane normal to the relative velocity of the particle. The area $A_\parallel$ results from a projection on a plane parallel to the fluid flow.

The drag coefficient of the artificial snowflakes can be calculated from the experimental data with Equation 2.2. In Figure 2.5, the experimentally obtained drag coefficients are shown as a function of the Reynolds number and compared to the drag of a sphere. Here the reference area A_{ref} is given by the projected area of a volume equivalent sphere and the characteristic length d is the diameter of this volume equivalent sphere. The data show the decrease in drag coefficient with increasing Reynolds number. However, the data exhibit significant scatter. This is associated with the large variety of different snowflake shapes. The scatter indicates that it is necessary to account for the individual geometry of each snowflake.

The models of Haider and Levenspiel [69], Ganser [60] and Hölzer and Sommerfeld [81] account for the nonspherical shape of particles by incorporating geometric descriptors. The most common geometric descriptors used for the estimation of the drag of nonspherical bodies are the volume equivalent diameter, the sphericity and the crosswise sphericity. These quantities are defined in Equation 1.2 on page 5 and can be calculated from the three-dimensional digital snowflake models, which allows the prediction of the drag coefficient from the aforementioned models.

In Figure 2.6, a comparison of the model predictions of the drag coefficients with the experimentally obtained values is shown. The models of Haider and Levenspiel and Ganser overpredict the experimental values significantly. This is attributed to the fact that these models have been developed for polyhedrons, disks and similar

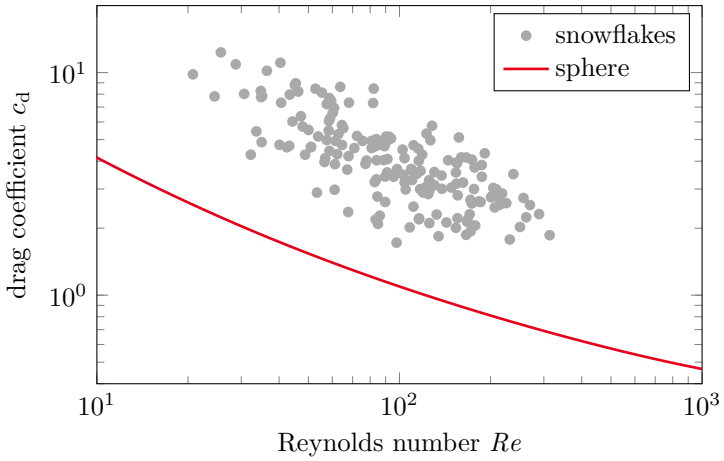

Figure 2.5: Experimentally measured drag coefficients of the artificial snowflakes as a function of Reynolds number. The data are compared to the drag coefficient of a sphere given by Clift and Gauvin [30].

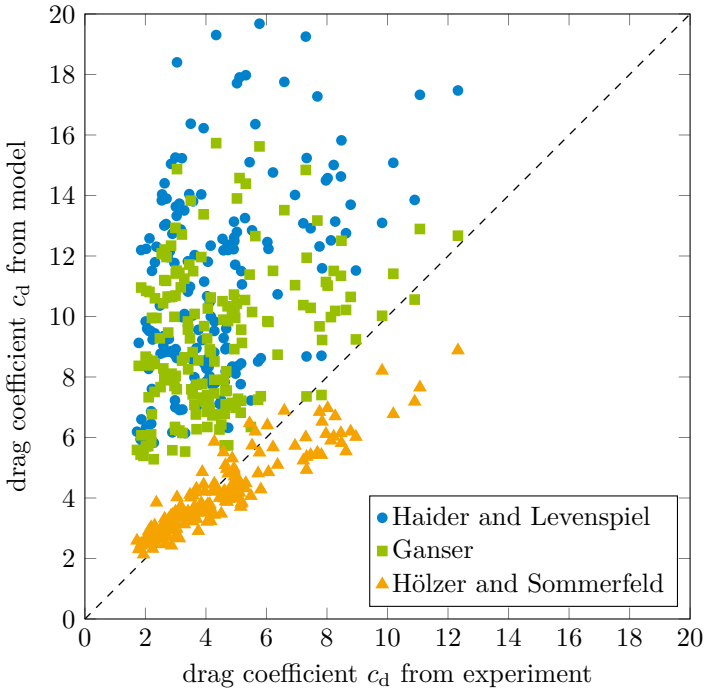

Figure 2.6: Comparison of the drag coefficient predicted by the models of Haider and Levenspiel [69], Ganser [60] and Hölzer and Sommerfeld [81] and the drag coefficient in the experiment.

bodies, which do not represent the geometric complexity of snowflakes. The model of Hölzer and Sommerfeld fits the experimental data well. However, the evaluation of the model requires the particle sphericity, which implies knowledge of the volume and surface area of the particle. While the volume of natural snowflakes can be measured by melting the flake and calculating its mass from the resulting drop, it is not feasible to accurately quantify the surface area of a natural snowflake.

2.3 Convex hull approximation of the particle shape

Correlations for the drag coefficient of nonspherical particles available in literature have the advantage that they are validated for a large range of Reynolds numbers. Furthermore, these models can be applied directly to hailstones or single ice crystals in the form of plates, columns or needles. For these particles, the sphericity can be estimated from multiple photographs from different angles, which can be provided by modern measuring instruments. However, for highly complex and porous particles, an accurate reconstruction of the complete geometry is unfeasible. Therefore, a new approach is proposed here to simplify the geometry of snowflakes while maintaining the drag of the complex shaped particle. Due to aerodynamic considerations, the particle drag is approximated by the drag of its convex hull. An exemplary snowflake and its convex hull are illustrated in Figure 2.7.

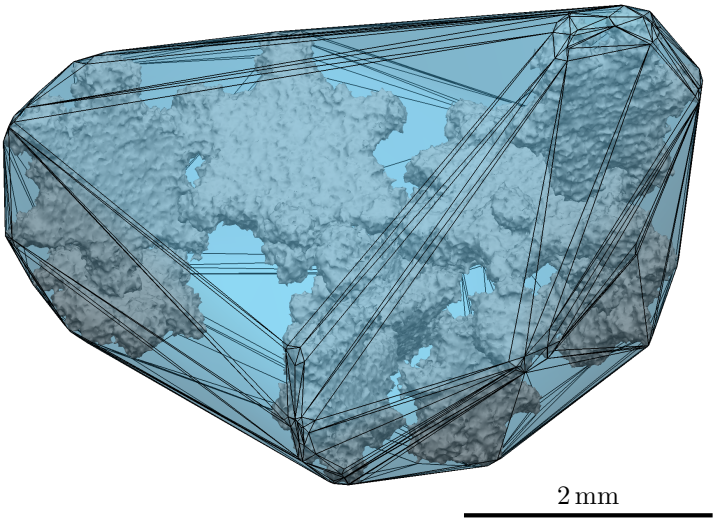

Figure 2.7: Digital model of a snowflake and the corresponding convex hull enclosing it. The hypothesis is, that in the investigated Reynolds number range, both bodies experience approximately the same drag force.

This shape simplification is justified if the flow velocity through the pores is significantly smaller than the freestream velocity. The Reynolds number in the pores is then much smaller than in the outer flow, which indicates that viscous forces affect the flow in the pores considerably. The convex hull of the particle must be considered as a porous body. The permeability κ of this porous body can be roughly estimated by the Carman–Kozeny equation given by [41]

$$\kappa = \frac{\varphi^3}{180(1-\varphi)^2} d_{\mathrm{pore}}^2 \tag{2.3}$$

with the porosity φ and d_{pore} as the typical pore size. The pressure difference Δp at the particle surface can be estimated from Bernoulli's equation as

$$\Delta p \sim \frac{1}{2}\rho u^2. \tag{2.4}$$

when neglecting suction in the porous body. Darcy's law now enables estimating the average flow velocity u_* through the convex hull as

$$u_* = \frac{\kappa \Delta p}{\nu \rho d} = u \frac{d_{\mathrm{pore}}^2 \varphi^3}{360 d^2 (1-\varphi)^2} Re. \tag{2.5}$$

Based on typical snowflakes from the data set, the ratio of the typical pore size to the particle size is estimated as $d_{\mathrm{pore}}/d \sim 0.2$, the porosity of the convex hull is approximately $\varphi \sim 0.6$ and the Reynolds number is in the order of 10 to 10^3. The upper limit of the range of Reynolds numbers provides an upper bound for the average fluid velocity entering the porous body of the order of $u_*/u \sim 10^{-1}$. The resulting reduction in pressure at the surface of the porous convex hull is proportional to the square of the average velocity through the body. Therefore, the reduction in pressure is approximately $\rho u_*^2/2 \ll \Delta p$. Thus, the effect of suction on the drag coefficient of the porous convex hull is negligibly small. Based on this estimation, the flow through the porous convex hull can be neglected and the drag force of the snowflake can be approximated by the drag of its convex hull.

These considerations are in qualitative agreement with the work of Tagliavini et al. [180], who attribute an increase in drag to the pores of a dendritic ice crystal. Tagliavini et al. explain this increased drag with a thickening of the boundary layer, which led to a reduced flow through the pores of the dendritic ice crystal. This effect was also observed by Cummins et al. [43] for the pappus of a dandelion.

The models of Haider and Levenspiel, Ganser and Hölzer and Sommerfeld can then be evaluated for the convex hull of the snowflake. The characteristic length d is now given by the volume equivalent diameter of the convex hull and the reference area A_{ref} is given by the area of the convex hull projected on the plane normal to the relative velocity vector. A comparison of the model predictions with the experimentally obtained drag coefficients is shown in Figure 2.8. The predictions of the models of Haider and Levenspiel and Ganser improved significantly in

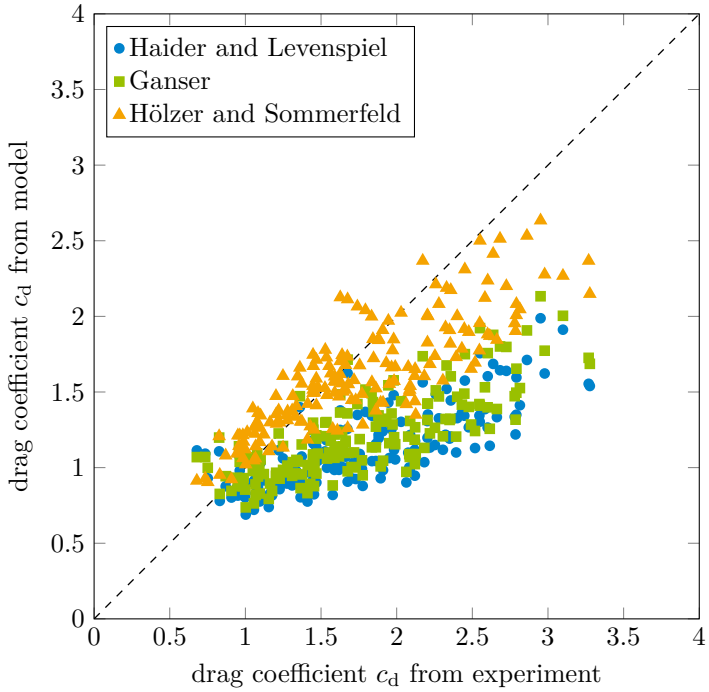

Figure 2.8: Comparison of the models of Haider and Levenspiel [69], Ganser [60] and Hölzer and Sommerfeld [81] evaluated for the three-dimensional convex hull geometry with the drag coefficients obtained from the experiment.

comparison to the prediction shown in Figure 2.6. This is attributed to the shape of the convex hulls, which bear more resemblance to the bodies with which Haider and Levenspiel and Ganser calibrated their models. Furthermore, the predictions of the Hölzer and Sommerfeld model improved slightly. However, the main advantage of the proposed convex hull shape approximation is the significant simplification of the complex geometry. While it is unfeasible to accurately measure the complete three-dimensional geometry of natural snowflakes, the geometry of its convex hull can be estimated from multiple projections of the particle. Leinonen et al. [110] trained a neural network to reconstruct the convex hulls of natural snowflakes from stereoscopic images of the particle. The authors report reasonable results that encourage the use of the convex hull to estimate the drag of a snowflake.

Finally, it should be noted that the proposed approach is not limited to snowflakes. On the contrary, the convex shape simplification can be considered as a general extension of drag models for irregular particles for which the flow through the pores of the body is negligibly small. Therefore, the model is also applicable to other particles. In the framework of icing, the model can also be applied to ice particles such as graupel, hailstones, single ice crystals or other particles.

2.4 Prediction of three-dimensional convex hull descriptors from two-dimensional projections

The convex shape approximation proposed above represents a drastic simplification of the three-dimensional shape of a snowflake. Nonetheless, this simplified shape still represents a three-dimensional geometry. However, most in-flight and ground measurements only capture a single two-dimensional projection of the particle, which does not facilitate a three-dimensional reconstruction. In order to extract information on the geometric descriptors relevant for the trajectory calculation of snowflakes, two-dimensional images of artificial snowflakes are analyzed to identify a correlation between two-dimensional descriptors and three-dimensional descriptors.

The correlation of various two-dimensional length and roundness measures with the volume equivalent diameter and the sphericity of the convex hull has been analyzed. The strongest correlations have been identified with the following measures: First, the area equivalent diameter of the convex hull defined as

$$d_{2\mathrm{D}} = \sqrt{\frac{4A_{\mathrm{p}}}{\pi}} \tag{2.6}$$

with the area of a projection of the convex hull A_{p} is employed to predict the volume equivalent diameter of the convex hull. Second, the Cox roundness of the convex hull projection [39] is used to estimate the sphericity of the three-dimensional convex hull. The Cox roundness is defined in Equation 1.1 on page 5 as

$$\Psi = \frac{4\pi A_{\mathrm{p}}}{P^2}, \tag{2.7}$$

where P denotes the perimeter of the projection of the convex hull.

In the following, a simplified model of a convex hull is constructed and the relations between its two-dimensional and three-dimensional properties are derived. Subsequently, a data set based on the three-dimensional digital snowflake models is generated and the correlations are validated with this data set.

2.4.1 Construction of simplified convex particles

As it can be recognized in Figure 2.7, the surface of a convex hull of an irregular particle can be represented by a multitude of triangles. Analogously, the volume of the convex hull is composed of numerous tetrahedrons. Thus, a simplified convex shape can be constructed by combining multiple similar tetrahedrons.

Consider one of these elements of the simplified convex shape with a geometry as shown in Figure 2.9a. The four vertices of the tetrahedron are given by A, B, C and O. The vertices A, B and C are at the surface of a sphere with radius R and the vertex O is located at the center of the sphere. The face ABC is an equilateral triangle with sides of length $L = lR$. Here l denotes a dimensionless parameter, which determines the sphericity of the convex shape.

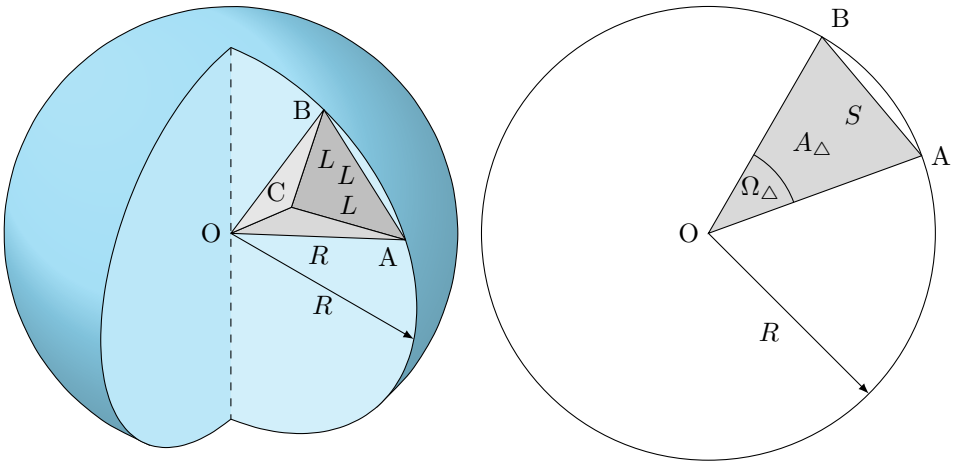

(a) Element of the three-dimensional convex body

(b) Element of the projection

Figure 2.9: Models of a simple convex hull and its projection. (a) a three-dimensional element of the convex hull, approximated by a tetrahedron, (b) an element of the projection.

Geometrical considerations yield the volume of the tetrahedron $V_\diamondsuit$, the area of its outer face $A_\diamondsuit$ and the solid angle $\Omega_\diamondsuit$. The solid angle is defined as the area of the segment of a unit sphere that is covered by the tetrahedron.

$$V_\diamondsuit = \frac{R^3}{12} l^2 \sqrt{3 - l^2} \text{ with } l < \sqrt{3} \tag{2.8}$$

$$A_\diamondsuit = \frac{\sqrt{3}}{4} l^2 R^2 \tag{2.9}$$

$$\Omega_\diamondsuit = 4 \arctan \sqrt{\tan \frac{3\theta}{4} \tan^3 \frac{\theta}{4}} \text{ with } \theta = 2 \arcsin \frac{l}{2} \tag{2.10}$$

Since the solid angle of a sphere is given by 4π, the average number of tetrahedrons in the convex body can be estimated as

$$N_\diamondsuit = \frac{4\pi}{\Omega_\diamondsuit}. \tag{2.11}$$

The volume equivalent diameter and the sphericity of the body can then be estimated as

$$d_{\mathrm{eq}}(l) = \sqrt[3]{\frac{6 V_\diamondsuit N_\diamondsuit}{\pi}} = R \sqrt[3]{\frac{2 l^2 \sqrt{3 - l^2}}{\Omega_\diamondsuit(l)}} \tag{2.12}$$

$$\Phi(l) = \frac{\pi d_{\mathrm{eq}}^2}{A_\diamondsuit N_\diamondsuit} = \sqrt[3]{\frac{4 \Omega_\diamondsuit(l)(3 - l^2)}{l^2 \sqrt{27}}}. \tag{2.13}$$

Considering a projection of the convex body as shown in Figure 2.9b, the element of the projection can be approximated by an isosceles triangle with legs R and

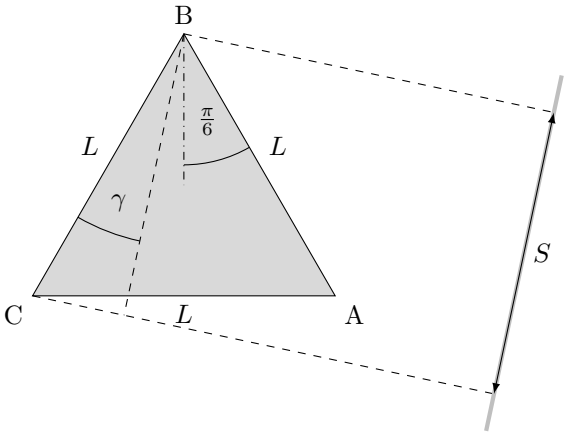

Figure 2.10: Projection of the triangle ABC on an arbitrary plane normal to the triangle plane. Definition of the inclination angle γ and the projection length S.

base $S = sR$. The ratio s of the base to the radius represents a measure for the roundness of the projection. The area $A_\triangle$, the vertex angle $\Omega_\triangle$ and the average number $N_\triangle$ of triangles in the projection are given by

$$A_\triangle = \frac{R^2 s}{2}\sqrt{1-\frac{s^2}{4}} \tag{2.14}$$

$$\Omega_\triangle = 2\arcsin\frac{s}{2} \tag{2.15}$$

$$N_\triangle = \frac{2\pi}{\Omega_\triangle}. \tag{2.16}$$

Therefore, the area equivalent diameter of the projection and the Cox roundness can be estimated as

$$d_{2\mathrm{D}}(s) = \sqrt{\frac{4A_\triangle N_\triangle}{\pi}} = R\frac{\sqrt{s}\sqrt[4]{4-s^2}}{\sqrt{\arcsin\frac{s}{2}}} \tag{2.17}$$

$$\Psi(s) = \frac{4\pi A_\triangle N_\triangle}{(sRN_\triangle)^2} = \frac{2}{s}\sqrt{1-\frac{s^2}{4}}\arcsin\frac{s}{2}. \tag{2.18}$$

Finally, the relation between the two characteristic lengths L and S can be determined by considering a projection of the equilateral triangle ABC on an arbitrary plane normal to the triangle plane, which is illustrated in Figure 2.10. Here the projection of the length L corresponds to the length S. Assuming that the inclination angle γ is uniformly distributed between 0 and $\pi/6$ yields the average length of the projection

$$S = \frac{6}{\pi}\int_0^{\pi/6} L\cos\gamma\,\mathrm{d}\gamma = \frac{3L}{\pi}, \text{ i.e., } s = \frac{3l}{\pi}. \tag{2.19}$$

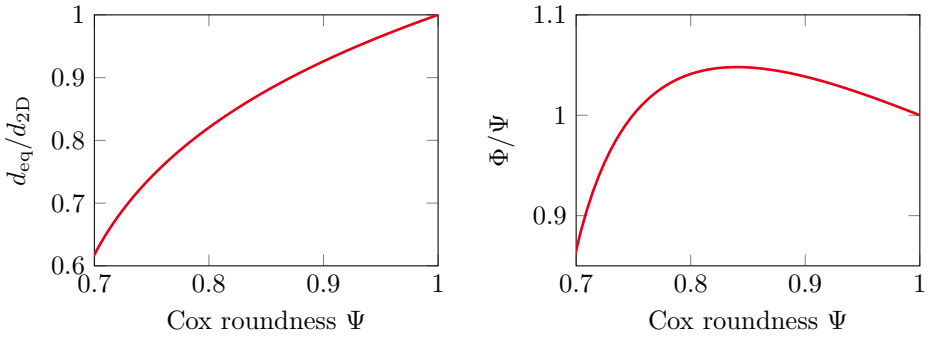

(a) Diameter ratio d_{eq}/d_{2D} as a function of the Cox roundness Ψ

(b) Ratio Φ/Ψ as a function of the Cox roundness Ψ

Figure 2.11: Theoretically predicted correlations of convex hull properties with the projection properties based on the simplified convex body model. Both ratios of the three-dimensional properties to the two-dimensional property depend on the Cox roundness.

The integration limits account for the symmetry of the equilateral triangle. This equation relates the two-dimensional projection to the three-dimensional body.

The ratio of the three-dimensional descriptors of the convex body to the two-dimensional descriptors of its projection is shown in Figure 2.11. Both ratios d_{eq}/d_{2D} and Φ/Ψ are plotted as a function of the roundness of the projection. The Cox roundness of the projection is in the range of $\Psi \in [0.66, 1]$ and the approximation is not applicable to projections with a Cox roundness smaller than 0.66.

The construction of the described convex body is based on several simplifications and does not aim at representing all varieties of real convex hulls of snowflakes. Nonetheless, the simple convex hull model can assume different sphericities and reveals a correlation of the two-dimensional and three-dimensional geometric descriptors.

An important feature is that the fractal aspects of the complex shape of a snowflake do not appear in the convex hull. The fractal geometry of natural snowflakes results in a nonlinear relationship between the two-dimensional and three-dimensional descriptors. In contrast, the relationship for these properties of the convex hull is linear.

2.4.2 Correlations based on a data set of artificial snowflakes

The method for generating digital models of snowflakes described in subsection 2.1.1 is used to generate a data set from which the correlation of two-dimensional and three-dimensional geometric descriptors can be determined.

For this purpose, an ensemble of 102 three-dimensional convex hulls of digital

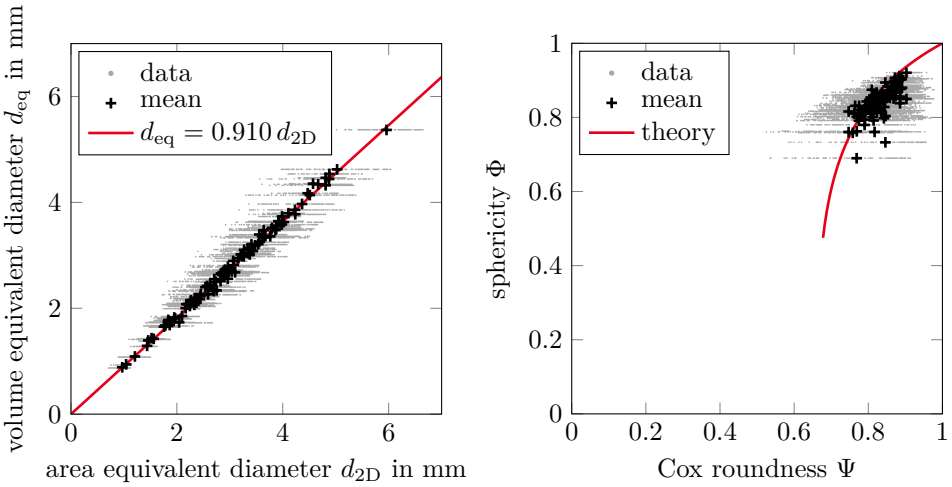

(a) Volume equivalent diameter d_{eq} of the convex hull as a function of the area equivalent diameter d_{2D} of its arbitrary projections

(b) Sphericity Φ of the convex hull as a function of the Cox roundness Ψ of its projections

Figure 2.12: Correlations of the main geometrical properties of the digital snowflakes. The plus signs indicate the mean of the two-dimensional descriptor of the 100 projections for each snowflake.

snowflakes is created and for each snowflake 100 projections on planes of random orientation are produced. This procedure yields 10 200 projections of artificial snowflakes. The three-dimensional models and the two-dimensional projections are analyzed with respect to various geometric properties.

Based on this data set, the correlations shown in Figure 2.12 are retrieved. In Figure 2.12a, the volume equivalent diameter d_{eq} of the convex hull is shown as a function of the area equivalent diameter d_{2D} of its projection. The volume equivalent diameter of the convex hull appears to be proportional to the area equivalent diameter of its projection. The linear fit exhibits excellent agreement. Recalling the dependency of the constant of proportionality on the particle sphericity illustrated in Figure 2.11a, this suggests that the convex hulls are similar and their shape does not change significantly with particle size.

In Figure 2.12b, the convex hull sphericity Φ is shown as a function of the Cox roundness Ψ of its projection. The numerically obtained data is compared with the theory developed for the simple convex bodies described by Equation 2.13, 2.18 and 2.19. The agreement of the mean Cox roundness of each snowflake and the simple convex body model is rather good. However, this observation is limited to the range of sphericities covered by the generated snowflakes. A comparable agreement is obtained when approximating the convex hull sphericity with the Cox roundness of its projection, i.e., $\Phi \approx \Psi$.

The identified relations can be used to estimate the volume equivalent diameter

and the sphericity of the convex hull of a particle. The area equivalent diameter and the Cox roundness can be evaluated from the two-dimensional convex hulls of projections of the particle. These measures can then be applied to approximate the three-dimensional descriptors required for the prediction of the drag of the particle.

Following this, the orientation of a snowflake in a flow can be accounted for by estimating the projected area $A_\perp$ normal to the relative velocity. The maximum projected area of the particle is approximated with the projected area of the circumscribed sphere of radius R. The ratio $A_\perp/A_\parallel \sim 4R^2/d_{\mathrm{eq}}^2$ can be obtained as a function of the Cox roundness of the projection from the theoretical considerations above by applying Equation 2.12, 2.18 and 2.19. The data set of the projections of artificial snowflakes is used to calculate the Cox roundness of the two-dimensional convex hull of the projection. The ratio $A_\perp/A_\parallel$ can then be calculated from the equations above. A comparison of the theoretically predicted values with the values obtained by the experiments is shown in Figure 2.13. In this statistic, the two side views captured in the experiments are treated as independent observations, which is based on the assumption that the particle does not assume a preferred orientation in the horizontal plane. This is encouraged by the fact that several particles rotate around the vertical axis as they move through the fluid. The theory yields a slight overprediction of the area ratio. This discrepancy can be explained by the fact that in a few experimentally observed cases, the area projected into the

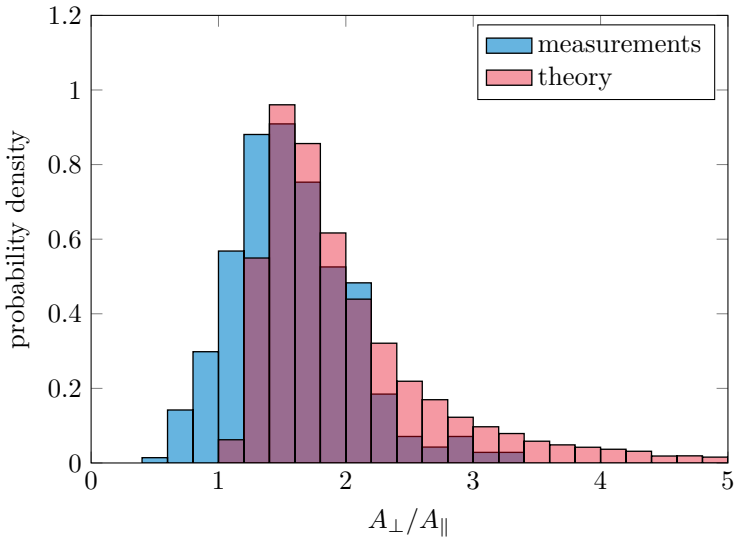

Figure 2.13: Histogram of the ratio $A_\perp/A_\parallel$ for the convex hull. The area $A_\perp$ results from the projection of the convex hull onto a plane normal to the relative velocity. Conversely, the area $A_\parallel$ results from a projection onto a parallel plane. The two depicted histograms allow a comparison of the experimental data with the data predicted by the theoretically constructed convex bodies.

direction of flow was slightly smaller than the projections observed from the side view. This is not accounted for in the theory. Nonetheless, considering that only a single projection is used to estimate the area projected in the direction of flow, the theory agrees remarkably well with the experiments. The calculated projected area $A_\perp$ can finally be used to approximate the crosswise sphericity $\Phi_\perp$ of the three-dimensional convex hull.

2.5 Comparison with natural snow

The results presented in the sections above are based on the artificial snowflakes described in subsection 2.1.1. To provide a final validation, the predicted fall speed of the snowflakes in the synthetic data set is compared to that of natural snowflakes. The fall speed is selected as measure for this validation since literature on the drag coefficients of natural snowflakes is sparse.

Barthazy and Schefold [12] investigated the falling of natural snowflakes and proposed a correlation between fall speed and the maximum dimension of the particle. Furthermore, they characterized the degree of riming and the type of single crystals composing the snowflake. In accordance with the data set described above, the data for aggregates of dendritic ice crystals are chosen from the data of Barthazy and Schefold. This large data set also provides information about the scatter in the fall speed among the particles, which is generally significant due to the unique complex geometry of snowflakes. To compare the synthetic data set presented in subsection 2.4.2 with the data of Barthazy and Schefold, the methods described above are applied to predict the drag coefficients and finally the terminal velocities of the particles. This evaluation is based on the area equivalent diameter and the Cox roundness of the convex hull from each of the more than 10 000 particle projections. The approach proposed above is then used to approximate the three-dimensional descriptors of the convex hull of the snowflake, which allows the prediction of the drag and the terminal velocity. In order to estimate the particle mass, the mass–size relationship established by Baker and Lawson [10] is applied. Thus, only information derived from the two-dimensional projections of the snowflakes is used.

The obtained fall speeds are shown in Figure 2.14. The colors indicated in the colorbar specify the distribution of the data resulting from the projections. The markers for the artificial snowflakes correspond to mean values obtained for each snowflake from the data set. The data of Barthazy and Schefold for moderately rimed and densely rimed aggregates of dendritic ice crystals are presented for comparison. Each data point corresponds to the median fall speed from the corresponding particle size class. The dashed lines represent the 17^{th} and 83^{rd} percentiles and indicate the scatter in the data. In addition, the correlations proposed by Barthazy and Schefold are illustrated.

The synthetic data set agrees well with the data set for natural snowflakes.

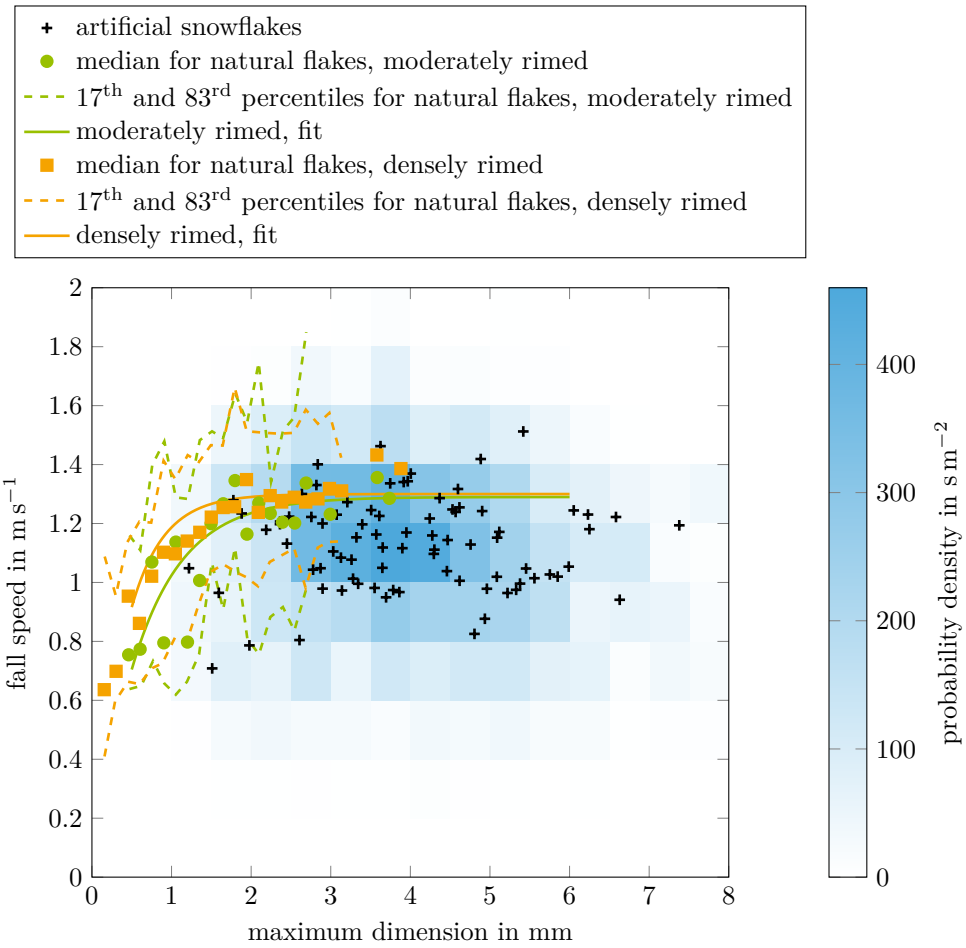

Figure 2.14: Comparison of the synthetic data set with data from Barthazy and Schefold [12] for natural snowflakes. The color indicated by the colorbar represents the distribution of the terminal velocities obtained from the generated particle projections. The markers for the artificial snowflakes correspond to the mean value obtained for each snowflake. The data of Barthazy and Schefold is represented by the median fall speed for each size class (squares and circles) and the 17$^{\text{th}}$ and 83$^{\text{rd}}$ percentiles (dashed lines). Furthermore, the fitted correlations proposed by Barthazy and Schefold is illustrated.

Both magnitude and scatter are comparable. While the artificial snowflakes are relatively large in comparison to the particles in the considered data set, Barthazy and Schefold noted that the fall speed tends to saturate as snowflakes get larger, i.e., no significant increase in fall speed is expected for larger particles. The good agreement of the synthetic data and the data for natural snowflakes confirms that the generated snowflakes can be considered representative of natural snowflakes. Furthermore, the calculation of the drag coefficient and the terminal velocity based on the convex hull of a two-dimensional projection yields satisfactory results. Finally, however, it should be noted that the snowflake mass has a significant influence on the fall speed.

2.6 Summary

The work presented in this chapter comprises an experimental investigation of the drag coefficient of snowflakes, the modeling of this drag coefficient and the reconstruction of the relevant snowflake geometries from particle projections. The experimental investigation is conducted with digitally generated and 3D-printed snowflakes. An approximation of the snowflake geometry with its convex hull has been proposed and it has been shown that the predictions of the drag force can be improved with this approach, while drastically simplifying the particle geometry. While it is unfeasible to measure the exact three-dimensional geometry of natural snowflakes, the convex shape can be obtained not only in the laboratory, but also in the field, as demonstrated by Leinonen et al. [110]. Furthermore, a simplified theoretical convex hull has been described and the correlation of its two-dimensional and three-dimensional descriptors has been derived. Finally, the digital snowflake models have been used to test the correlation of these two-dimensional and three-dimensional descriptors numerically. In the generated data set, the volume equivalent diameter of the three-dimensional convex hull and the area equivalent diameter of the two-dimensional convex hull of the projection show a very good agreement. Moreover, the Cox roundness of this two-dimensional data can be used to approximate the convex hull sphericity. The availability of multiple projections improves these predictions significantly.

The presented methods enable the estimation of the three-dimensional parameters relevant for drag calculations from two-dimensional projections of snowflakes. This approach circumvents the need for estimating the intricate three-dimensional shape of the snowflake and yields improved results in the range of Reynolds numbers relevant for snow. Furthermore, the developed model is not restricted to snowflakes but can be applied to other particles, which can be porous or impermeable. These results provide a valuable improvement in the computation of snowflake trajectories, which has significant benefits for the prediction of aircraft icing and weather phenomena.

3 Melting of snowflakes

The melting of ice particles plays a crucial role in aircraft icing and dictates whether ice crystals and snowflakes will adhere to surfaces upon impact. This is highlighted by the strong dependency of icing severity on melt ratio illustrated in Figure 1.6 on page 18. Thus, a comprehensive understanding of the melting process of these particles is of utmost importance. While adequate models exist for regular ice crystals, models describing the melting of snowflakes exhibit a high degree of empiricism, which imposes a severe limitation on their universality.

In this chapter, an experimental study of the melting of snowflakes and a theoretical model to describe this process are presented. First, the method for generating natural-like snowflakes and the setup for melting the particles are described. Second, the physical phenomena observed in the experiments are elucidated and the evolution of the particle size and shape are presented. Subsequently, the theoretical model is derived, which is finally validated with the experimental results.

This chapter is based on the article *Melting of fractal snowflakes: Experiments and modeling* by Köbschall et al. [104], published in the International Journal of Heat and Mass Transfer. The original contents have been edited for this work.

3.1 Experimental methods

To investigate the melting process of snowflakes, two experimental setups are required. The first apparatus is designed to produce natural-like snowflakes, while the second setup is dedicated to investigating the melting of snowflakes. In this section, first, the apparatus used for the production of snowflakes is presented. Second, the experimental setup used for the melting experiments is described.

3.1.1 Snowflake production

The experimental investigation of snowflake melting requires natural-like snowflakes that are available on demand and can be used in the experiments without risking prior melting or fragmentation. Although the achievable reproducibility is limited in the context of snowflakes, it is beneficial, if the flakes under investigation exhibit similar morphologies. Therefore, an apparatus has been designed, which is capable of producing snowflakes in a controlled environment in the laboratory.

Warm air is humidified by flowing over a containment filled with warm water. It is then transported through a pipe into a chest freezer, where droplets that have formed due to condensation are separated and the humid air is supplied to the

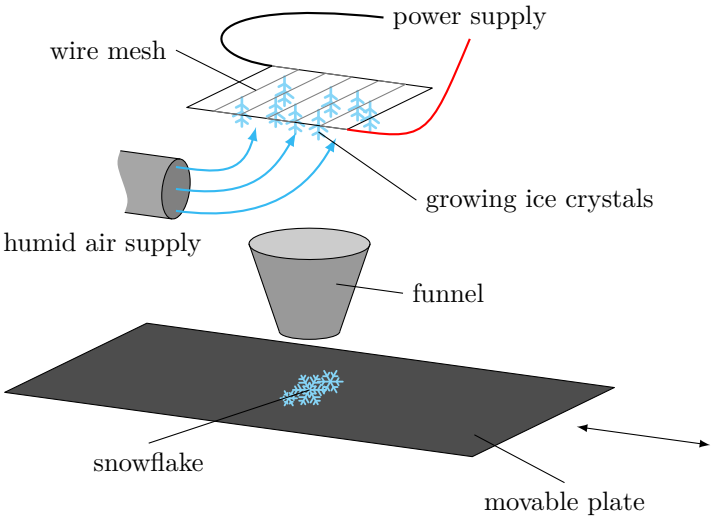

Figure 3.1: Snowflake production system consisting of a humid air supply, wires as nucleation sites and a funnel for aggregation.

apparatus shown in Figure 3.1. In this apparatus, the humid air is directed at a wire mesh, which acts as a nucleation site. On this wire mesh ice crystals form due to vapor deposition. Due to the significant supersaturation of the air with water vapor and the prevailing temperature, dendritic ice crystals grow. After the ice crystals on the wires reached a sufficient size, the ice is shed by shortly heating the wires with an electric power supply. The shed ice crystals fall into a funnel where they aggregate and form a snowflake, which is finally deposited on a movable plate.

Although the wires are only heated shortly, droplets can form and lead to solid ice spheres attached to the snowflakes. Since these ice spheres have a density which is significantly higher than that of natural snowflakes, the laboratory-generated snowflakes that exhibit these defects are excluded from the experiments.

Figure 3.2 shows exemplary laboratory-generated snowflakes in comparison with natural snowflakes from the data base of Grazioli et al. [66]. The laboratory-generated snowflakes correspond to aggregates formed of fragments of dendritic ice crystals. The morphology of the produced snowflakes is similar to those of the natural snowflakes. Both sets of snowflakes represent highly porous and fragile ice structures with thin branches extruding outwards.

3.1.2 Setup for the melting of snowflakes

A detailed investigation of the melting of snowflakes requires a continuous observation of the melting particle, which necessitates that the particle remains in the field of view of the camera. Previously, this has been realized by fixing the snowflake to

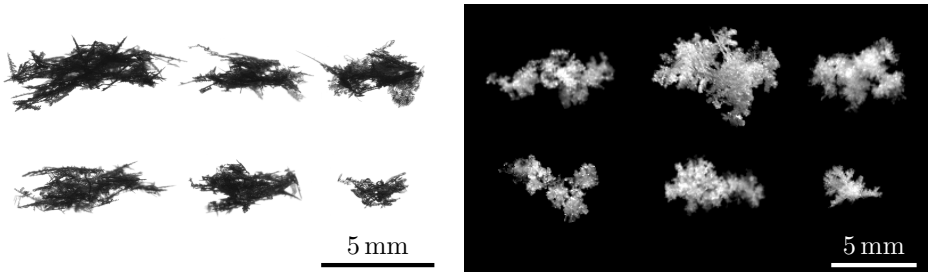

(a) Laboratory-generated snowflakes

(b) Natural snowflakes from the database of Grazioli et al. [66]

Figure 3.2: Comparison of the laboratory-generated snowflakes with natural snowflakes.

a string or in a mesh. However, the downside of this method is that the presence of these strings influences the shape evolution and the liquid water transport in the snowflake during melting. In order to minimize external influences on these aspects, an acoustic levitator is utilized in the present study. In the following, first, the acoustic levitator acting as the core of the experimental setup is presented and second, the warm air flow system and the measurement system are described.

Acoustic levitation makes use of standing acoustic waves, which transfer momentum to the levitated particle. This effect as well as its application in acoustic levitators is described in detail in literature [21, 5, 124]. The acoustic levitator constructed for this study generates the standing wave with multiple opposing ultrasonic transducers operated at 40 kHz. The design is based on the levitator proposed by Marzo et al. [124], which has been extended with an additional ring of transducers. The apparatus consists of 120 ultrasonic transducers positioned on two opposing spherical caps. Due to the additional ring of transducers in comparison to the design of Marzo et al., the levitated particle exhibits an increased stability against disturbances in the direction perpendicular to the levitator axis. The difficulty with nonspherical particles in acoustic levitation is that they tend to spin around the axis of the levitator. To counter this effect, the acoustic lock principle proposed by Cox et al. [40] is implemented and can be used to stabilize the orientation of the snowflake. For an improved lateral stability of the particle in the air flow, the axis of the levitator is aligned horizontally. This allows to supply the warm airflow from below the snowflake. Thus, the aerodynamic forces acting on the particle compete against gravity, enabling air speeds of up to $1.5\,\mathrm{m\,s^{-1}}$ without blowing the particle out of the field of view of the camera.

The influence of the acoustic field on the heat and mass transfer of a levitated particle has been investigated by Yarin et al. [204] and Junk et al. [89]. Yarin et al. [204] studied the effects of the acoustic field on the external flow supplied to the particle. They found that with increasing Reynolds number, the influence of the acoustic field on the flow decreases. The minimum Reynolds number in the present

experimental study exceeds the maximum Reynolds number in the study of Yarin et al. Therefore, no significant alteration of the warm airflow is expected. Junk et al. [89] gave recommendations to minimize effects of the acoustic field on heat and mass transfer processes. These recommendations – with regard to the drop aspect ratio and external flow – were followed in the present work. Furthermore, the experimental findings do not indicate any significant influence of the acoustic field on the melting process of the investigated snowflakes.

The experimental setup, which includes the acoustic levitator, a hot air supply, temperature and humidity sensors, a camera and a light source is shown in Figure 3.3. The illustrated setup is placed in a chest freezer to avoid melting of the snowflake prior to the start of the experiment. The acoustic levitator holds the melting snowflake in the warm air flow, which is supplied to the particle through insulated pipes from outside of the cold environment. The pipe has an inner diameter of 40 mm and its outlet is located approximately 30 mm in front of the snowflake. A screen is implemented in the pipe to provide a more uniform velocity distribution over the cross-section.

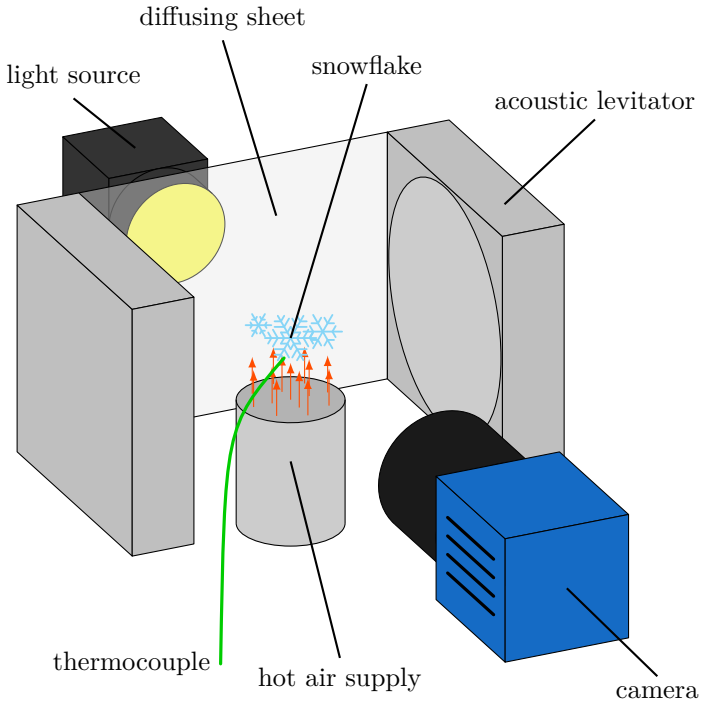

Figure 3.3: Experimental setup for the investigation of the melting of snowflakes. The setup consists of the acoustic levitator, a warm air supply, a thermocouple, a camera and a light source. The humidity sensor and the fan positioned upstream in the pipe are not illustrated here.

Depending on the desired experimental conditions, either ambient air, which is heated by a hot air blower, or dry pressurized air is used to melt the snowflake. This allows testing at different air temperatures and relative humidities. The insulated pipes are pre-heated before every experimental run by switching to a bypass for the warm air. The humidity of the incoming air is measured upstream in the pipe. The temperature is measured by a thermocouple placed at the outlet of the pipe just upstream of the snowflake. A small measurement tip of the thermocouple with a diameter of 0.15 mm enables a short response time. The initial temperature of the snowflake is assumed to be equal to the temperature of the air surrounding the particle prior to the start of the warm air flow.

For experimental runs with air that is not saturated with water vapor when reaching the snowflake, no condensation occurs in the insulated tube and the absolute humidity remains constant between the humidity sensor and the snowflake. Otherwise, if the temperature measured by the thermocouple is below the dew point, the air is assumed to be at saturation condition.

The relative humidity in the experimental runs ranges from dry air to fully saturated air and the air temperature was varied from 4 °C to 31.5 °C. The flow velocity ranged from $0.4\,\mathrm{m\,s^{-1}}$ to $1.4\,\mathrm{m\,s^{-1}}$ and has been measured with a thermal flow meter after the experimental run.

The melting snowflake is captured with a high-resolution camera at 60 frames per second and an opposing light source with diffusing sheet in order to obtain a uniform background.

Measurement of snowflake mass

The latent heat required to fully melt a snowflake is proportional to its mass, which is therefore expected to have a major influence on the melting process. In this study, the snowflake mass is determined from the volume of the resulting liquid drop, which is measured immediately after completion of melting. Rotational symmetry of the drop is assumed and the volume enclosed by rotating the contour of the drop is calculated. The volume is obtained for ten video frames shortly after melting, resulting in an average uncertainty of 3 % of the drop mass, which is typically in the order of 1 mg. For humid air this procedure yields an accurate estimation of the snowflake mass. However, for dry air an under-prediction of the initial snowflake mass is expected, since a significant amount of water sublimates or evaporates during the melting process. In their investigation of the melting of ice crystals Hauk et al. [74] extrapolated the initial ice crystal mass by characterizing the rate of evaporation of the resulting liquid drop. However, due to the vast change in the size of a melting snowflake, the surface area of the particle and thus the evaporation rate changes more drastically than for ice crystals. Hence, this procedure is not applicable here.

In order to improve the estimation of the initial snowflake mass for experimental runs conducted in dry air, the theoretical model proposed in this work and described

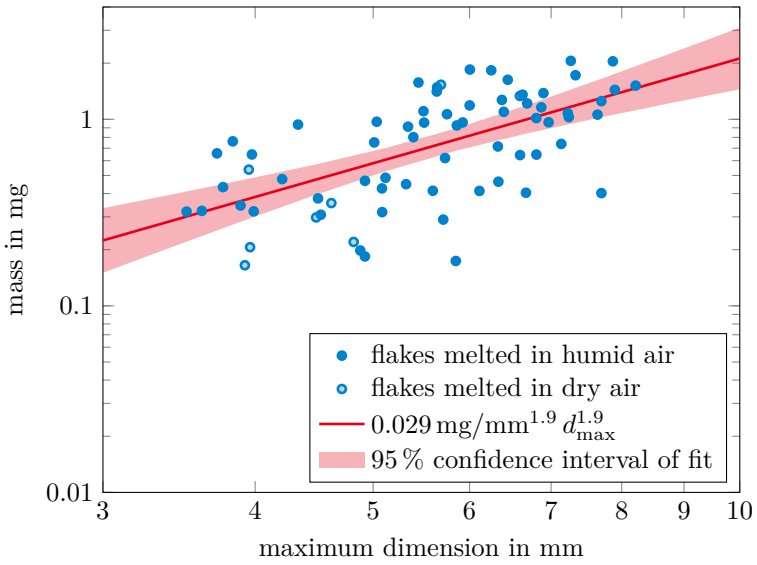

Figure 3.4: Snowflake mass as a function of the maximum dimension plotted for the laboratory-generated flakes. Snowflakes melted in air with a relative humidity of less than 30 % are indicated separately.

in section 3.3 is used. For these experimental runs, at first the initial snowflake mass is estimated and then the numerical model is solved for the particle mass at the experimentally measured melting duration. The initial snowflake mass estimate is then corrected and the corresponding particle mass at the melting duration is calculated. This procedure is iterated until the calculated particle mass matches the experimentally measured mass of the liquid drop. This iterative correction of the initial snowflake mass is only performed for experimental runs for which a significant mass of the snowflake is expected to evaporate.

The obtained snowflake masses are shown as a function of their maximum dimension in Figure 3.4. This graph shows a moderate correlation between mass and size, which is attributed to the variety of generated snowflakes. While some snowflakes appear as fine and fragile, others exhibit a more robust structure. Separating the generated snowflakes into different morphological classes could potentially improve the mass–size correlation.

The power law

$$m = \alpha d_{\mathrm{max}}^{\beta} \tag{3.1}$$

describing the relation between the snowflake mass m and its maximum dimension d_{max} can be estimated by linear regression of the logarithms of the measurements. Due to the large scatter in this mass–size relationship, the parameters α and β are subject to uncertainty.

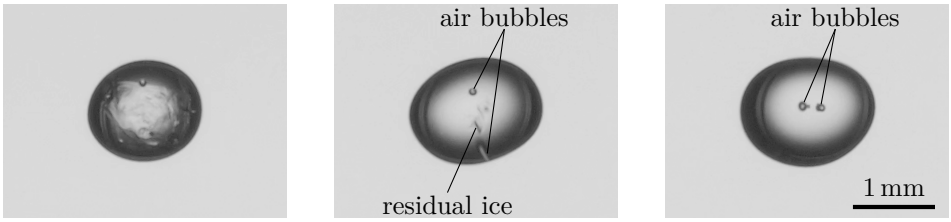

(a) Diffuse structure of remaining ice visible in drop

(b) Last frame with residual ice visible in drop

(c) Fully melted with remaining air bubbles

Figure 3.5: Detection of the first frame at which no residual ice is contained in the drop provides the melting duration of the snowflake.

The exponent in the mass–size power law given in literature for natural snow of similar morphology is well within the confidence bounds of the present fit. Locatelli and Hobbs [115] obtained an exponent of 1.9 for rimed aggregates and radiating assemblages of dendrites. Mitchell et al. [140] specify a value of 2.0 for aggregates of fragments of rimed dendritic crystals and for all snowflakes merged over all morphological classes.

Measurement of melting duration

The described experimental setup enables a detailed observation of the melting process of snowflakes in forced convection. However, in order to utilize the gathered data for the development and validation of a theoretical model, the duration of melting is required. While it is not feasible to accurately obtain the melted mass fraction throughout the melting process, the melting duration specifies the instant of time at which the snowflake has completely melted. This information can then be used to check and validate any model describing the melting process.

The high spatial resolution of the obtained videos provides a detailed insight into the liquid drop and enables the identification of any residual ice. An exemplary series of images from the final stage of a melting snowflake is depicted in Figure 3.5. Due to small differences in the refractive indices of liquid water and ice, the residual ice inside a liquid drop appears as a fuzzy inclusion that shrinks with time. In post-processing, the video frames are analyzed for remaining ice. The first video frame in which no ice is visible corresponds to the melting duration.

Conservative estimations of the measurement uncertainties are provided in Table 3.1. These uncertainties account for the oscillating motion of the snowflake due to the airflow and the acoustic field. Furthermore, the uncertainty in melting duration includes potential errors in the detection of the residual ice inside the liquid drop.

Table 3.1: Measurement uncertainties in obtained data.

Quantity	Uncertainty
Air temperature	$\pm 0.5\,°C$
Relative humidity	$\pm 1.5\,\%$
Air speed	$\pm 0.05\,m\,s^{-1}$
Drop mass	$\pm 3\,\%$
Melting duration	$\pm 0.25\,s$

3.2 Experimental results

In this section, the experimental results obtained by the melting of laboratory-generated snowflakes in forced convection in an acoustic levitator are presented. First, the phenomena that occur during snowflake melting are described and second, the trends for the evolution of the size and shape are analyzed.

3.2.1 Phenomena during snowflake melting

Figure 3.6 shows a series of images of an exemplary melting snowflake.

Since the initial temperature of the snowflakes in the experiments is below the melting point, the particle is first heated to 0 °C before the melting process starts. For particle sizes relevant for snowflake melting, variations in melting temperature and saturation vapor pressure due to the curvature of the particle can be neglected. Figure 3.6a depicts the initially dry snowflake at the start of the experiment. Due to the small Stefan number of the melting snowflake, the snowflake quickly reaches 0 °C and starts to melt.

Melting is then initiated at the outer branches of the snowflake. While in some cases, tiny droplets are visible at the tips of these branches, the produced meltwater is generally drawn quickly into the inside of the snowflake. This phenomenon has also been observed by Knight [102], Matsuo and Sasyo [130] and Mitra et al. [141]. This effect is associated with the porous structure of the snowflake and the high wettability of ice. The fine structures of the snowflake result in a high capillary pressure, which draws the liquid to the joints of the crystals and into the pores of the particle. Hence, it is difficult to visually identify liquid water on the particle for a large part of the melting process. This contrasts with the melting of a common ice crystal, where a liquid film quickly covers the particle [98].

Only at a later stage, when the pores of the snowflake are saturated with liquid water, a liquid layer becomes visible in Figure 3.6d. From this point on, the melting process is comparable to the melting of a single ice crystal. Surface tension shapes the growing liquid layer more spherical. While first cusps of ice can appear, as shown in Figure 3.6e, the liquid at some instant fully encloses the remaining ice. The particle then assumes an approximately spherical shape in this final stage of

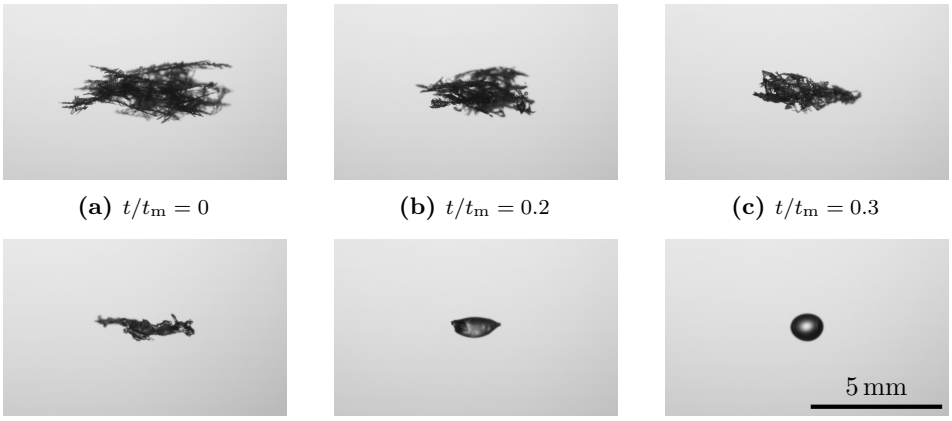

(a) $t/t_\mathrm{m} = 0$ **(b)** $t/t_\mathrm{m} = 0.2$ **(c)** $t/t_\mathrm{m} = 0.3$

(d) $t/t_\mathrm{m} = 0.4$ **(e)** $t/t_\mathrm{m} = 0.6$ **(f)** $t/t_\mathrm{m} = 1$

Figure 3.6: Melting process of an exemplary snowflake. The snowflake is initially fully frozen. Melting starts at the branches and then continues with the main ice frame. Finally, melting results in a liquid drop. The time is normalized with the melting duration t_m.

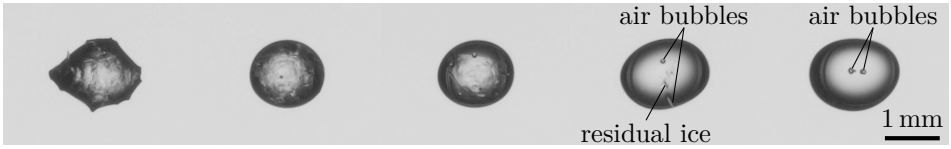

(a) **(b)** **(c)** **(d)** **(e)**

Figure 3.7: Final melting stage when the snowflake has already reached a spherical shape. The last stumps of the ice frame protruding out of the drop can be seen in (a). Subsequently, the remaining ice is fully enclosed by the drop. The last residual ice can be recognized in (d). The fully melted particle shown in (e).

melting.

This final stage of the melting process is shown in Figure 3.7 in more detail. The optical setup enables a clear view into the drop. Although the liquid already forms a spherical drop, it still contains residual ice, which continues to melt. In several cases, air bubbles are observed in the drop. These air bubbles form when pores are disconnected from the ambient air. However, their contributions to the total volume of the drop is negligible and thus does not significantly affect the estimation of the particle mass. In total 23 of 90 experimental runs exhibited air bubbles in the resulting drop.

In some experimental runs, breakup of the snowflake due to melting was observed. This occurs mostly for snowflakes that consist of multiple parts held together only by single branches of the crystals. Melting of the connecting branch leads to breakup of the snowflake, which typically occurs shortly after melting was initiated.

This is in contrast to a collapse of the snowflake, which can occur at a later stage of melting when crystal branches are pulled towards the core of the snowflake due to surface tension exerted by a thick liquid film.

Following breakup, usually at least one of the fragments is tossed out of the acoustic levitator, which restrains further evaluation of the experimental run. Therefore, runs for which a significant fraction of the snowflake mass is lost, are not included in the experimental results presented in the following. Due to this criterion, 18 of 90 experimental runs have been omitted from post-processing. However, while snowflakes that broke apart are not considered for post-processing, their melting behavior is not expected to differ qualitatively from the remaining snowflakes. Due to the morphology of the fragments, they can each be expected to melt similarly to an individual snowflake.

3.2.2 Size and shape evolution

In order to obtain a better insight into the dynamics of melting snowflakes, the evolution of the size and shape of the particles is analyzed. Figure 3.8 shows the evolution of various geometric descriptors of the melting snowflakes. Since this is a stochastic process due to the diversity of snowflake geometries, the graphs show the mean value and the standard deviation of all experimental runs. The limited number of geometric descriptors cannot describe the full complexity of the flakes. Therefore, a notable standard deviation can be anticipated. Nonetheless, the results illustrate several characteristic phenomena and provide a better understanding of the stages of snowflake melting.

The dimensionless descriptors are plotted as a function of time, which is made dimensionless with the melting duration of the snowflake. The maximum Feret diameter of the melting particle is nondimensionalized with the melted diameter of the flake. The melted diameter is defined as the diameter of the resulting drop and can be given by

$$d_\mathrm{m} = \sqrt[3]{\frac{6m}{\pi\rho_\mathrm{w}}} \tag{3.2}$$

with the density of liquid water ρ_w. The aspect ratio of the snowflake is defined as

$$AR = \frac{d_\perp}{d_\mathrm{max}} \tag{3.3}$$

where $d_\perp$ specifies the Feret diameter, which is orthogonal to the maximum Feret diameter d_max. The Cox roundness Ψ illustrates the smoothing of the particle contour and is defined in Equation 1.1 on page 5.

In Figure 3.8a it can be recognized that the maximum Feret diameter starts to decrease rapidly as soon as melting starts. The mean initial value shows that the initial maximum dimension of the flake is in average more than four times larger than the diameter of the resulting drop. After approximately two-thirds of the

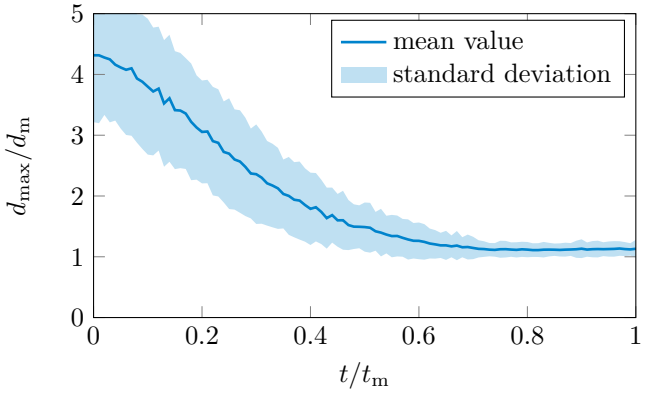

(a) Maximum Feret diameter

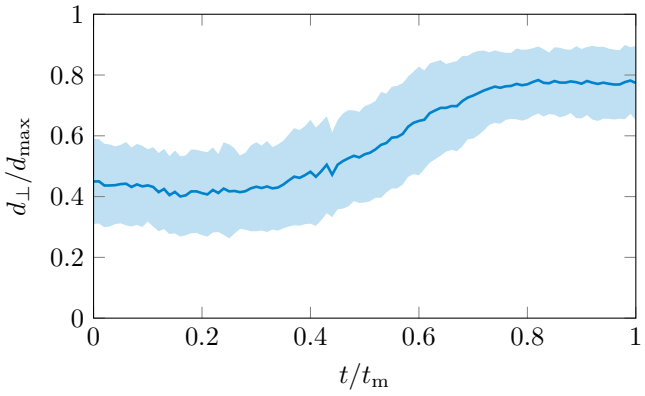

(b) Aspect ratio

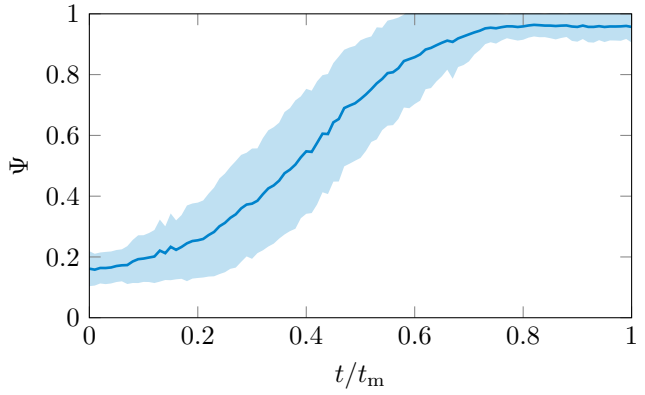

(c) Cox roundness

Figure 3.8: Evolution of dimensionless geometric descriptors of the melting snowflakes from all experimental runs plotted as a function of the time normalized with the snowflake melting duration.

melting process, the particle assumes a spherical shape and thus the dimensionless maximum diameter approaches unity. Due to the slight deformation of the drop in the acoustic field, the drop does not represent a perfect sphere, resulting in the maximum dimension being slightly larger than the diameter of a volume equivalent sphere, which corresponds to a ratio $d_{\mathrm{max}}/d_{\mathrm{m}}$ that is marginally larger than unity. Despite the liquid phase forming a spherical drop, it still contains residual ice, as shown in Figure 3.7.

Since all snowflakes eventually form a spherical drop, the standard deviation in the final melting stage is small. However, the scatter is much larger for the initially dry snowflake. This is due to the nonlinear relationship between the snowflake maximum dimension and its melted diameter. For a mass fractal dimension β smaller than three, the dimensionless maximum length depends on the absolute value of the maximum Feret diameter. Furthermore, variations in the factor α in the mass–size power law given by Equation 3.1 result in an increased scatter. Nonetheless, the drastic decrease in size and the extent of the stage in which the residual ice is fully enclosed by a spherical drop can be recognized clearly.

The aspect ratio of the melting snowflake is shown in Figure 3.8b. In contrast to the snowflake maximum dimension described above, the aspect ratio at first remains nearly constant. The snowflake simply appears to shrink, which can also be recognized in Figure 3.6a to 3.6c. This coincides with the stage in which meltwater is imbibed by the porous snowflake. The aspect ratio only increases when the pores are saturated and a liquid film covers the particle. The liquid water then affects the dimensions of the particle and leads to an increase in aspect ratio. This increase in aspect ratio can also be recognized in Figure 3.6e. In the final melting stage, the particle then again assumes a constant aspect ratio. This corresponds to the liquid phase forming an approximately spherical drop enclosing the residual ice. Due to the slight deformation of the drop in the acoustic levitator, the aspect ratio remains below unity, which would correspond to a perfect sphere.

The Cox roundness plotted in Figure 3.8c changes soon after the start of the melting process. The melting of the small branches leads to a significant decrease in the particle surface area and correspondingly to a decrease in the perimeter of its projection. This causes a drastic increase in the sphericity and the roundness. Thus, while the aspect ratio indicates that the particle simply shrinks, the contour of the particle is continuously smoothed due to the melting of the fine structures of the snowflake.

3.3 Theoretical study

In the following, a theoretical model for the melting of snowflakes is derived, which is based on the experimental observations presented above. Finally, the model predictions are compared to the experimental results.

3.3.1 Theoretical model

An adequate representation of the physics of melting snowflakes requires the modeling of two interlocked aspects: the heat and mass transfer and a geometrical model describing size and shape of the particle. Therefore, first, the structural model of the melting snowflake is described and second, the governing equations of heat and mass transfer are formulated for the melting process.

Structural model

The experimental observations presented above indicate that melting starts at the fine outer structures of the snowflake and the inner ice frame is at first not affected by melting. Therefore, structural rearrangements occur mostly at the outer surface of the particle. Snowflakes represent porous particles, where the ratio of flow velocity through the pores to the free stream is small, as shown in chapter 2. Furthermore, air flowing through the pores first has to pass the outer ice branches where it cools down, with the result that only little heat is transferred via the pores. Hence, the present model approximates that the melting front propagates from the outside of the particle towards its core.

Consider the growth of a snowflake as a process contrary to snowflake melting: Snowflakes are formed by aggregation of single snow crystals. A single snow crystal collides and interlocks with other crystals on its trajectory. Snow crystals adhering to the growing snowflake will likely attach to the outer branches. Thus, they will not significantly affect the inner structure of the flake, but lead to an increase in the size of the particle. The mass of the newly added crystal is hence deposited at the outside of the particle.

In contrast to the melting of a snowflake, its growth and the accompanying deposition of ice mass starts from its core and propagates outwards. The hypothesis underlying the structural model for the melting of snowflakes is that the process can be approximated as a reversed snowflake growth.

The deposition of ice mass during growth of a snowflake due to aggregation results in the snowflake exhibiting fractal aspects [88, 18, 82, 161]. These fractal aspects justify the use of a mass–size power law

$$m_\mathrm{i} = \alpha d_\mathrm{max,i}^{\beta}, \tag{3.4}$$

which is widely used in literature. Here the subscript i is introduced to refer to the ice phase of the particle. Since mass deposited during snowflake growth is not expected to significantly alter the inner structure of the flake, this mass–size relationship is applicable both to the snowflake prior and post collision with another ice crystal. Therefore, the power law cannot only be used to describe the bulk mass of the snowflake, but it is also applicable to characterize the mass distribution in the snowflake. This is illustrated schematically in Figure 3.9. Due to the similarity between snowflake growth and snowflake melting, this mass–size power law is used

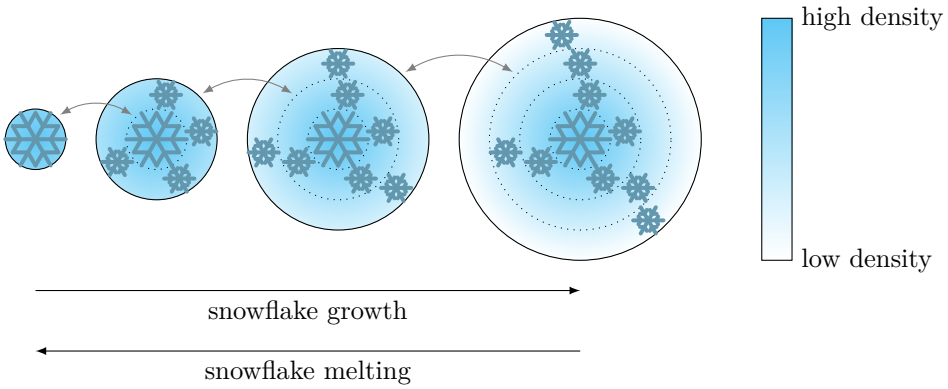

Figure 3.9: Schematic distribution of ice mass during growth and melting of a snow aggregate. The inner structure, indicated by the dotted circles, does not change during the process.

to describe the ice structure during the melting process.

To highlight the relation of the mass–size power law to the melting process, the temporal derivative of the power law can be considered. This is given by

$$\frac{\mathrm{d}m_\mathrm{i}}{\mathrm{d}t} = \alpha\beta d_\mathrm{max,i}^{\beta-1}\frac{\mathrm{d}d_\mathrm{max,i}}{\mathrm{d}t}. \tag{3.5}$$

The left-hand side of this equation can be interpreted as the negative melting rate of the snowflake, i.e., $\dot{m}_\mathrm{f} = -\mathrm{d}m_\mathrm{i}/\mathrm{d}t$ with the melting rate $\dot{m}_\mathrm{f}$.

As described in section 3.2, the generated meltwater is imbibed by the porous snowflake due to capillary forces. Therefore, in the first stage of melting, liquid water does not significantly contribute to the size and apparent shape of the particle. In the following stage, when a notable liquid film covers part of the surface, but the liquid does not yet form a spherical drop, the particle shape is affected by both the liquid and the ice. However, the particle size, given by its maximum dimension is still determined by the ice structure. Only in the last stage, when the residual ice is fully enclosed by a spherical drop, the particle size and shape are defined by the liquid phase. Due to the similar densities of ice and liquid water, the influence of the residual ice on the particle size can be neglected. This last stage of melting is initiated when the maximum Feret diameter of the ice frame reaches the diameter of the resulting liquid drop. Hence, the diameter of the resulting drop provides a lower bound for the maximum dimension of the melting particle. Accordingly, the maximum dimension of the melting particle can be expressed as

$$d_\mathrm{max} = \max(d_\mathrm{max,i}, d_\mathrm{m}). \tag{3.6}$$

This approach of calculating the size of the melting particle does not account for the full complexity of transient porous media flows. It is approximated that

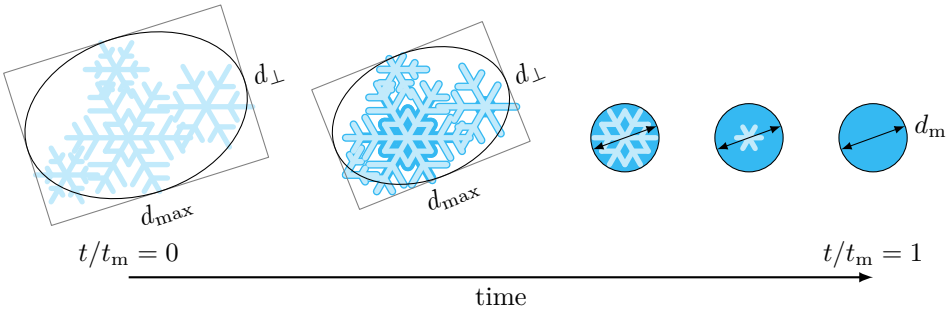

Figure 3.10: Approximation of the convex shape of a melting snowflake as an ellipsoid. The third axis of the ellipsoid is estimated as the geometric mean of the major and minor axes, i.e., $\sqrt{d_{\max} d_\perp}$. The aspect ratio defined as $AR = d_\perp / d_{\max}$ remains constant in the first stage of melting.

the meltwater is immediately redistributed within the porous snowflake. This requires a limited melting rate, since at very high melting rates, transient effects of the imbibition process could come into play and droplets could form at the outer branches.

The above model can be applied to calculate the evolution of the maximum dimension of a snowflake melting at a given melting rate. However, the melting rate is a function of the surface area of the particle, which is exposed to the warm air. Thus, a geometrical approximation of the snowflake is required in order to calculate the surface area.

As argued above, only a minor fraction of the convective heat transfer to the particle occurs in the pores of the snowflake. Therefore, the inner surface area of the pores does not have to be taken into account by the heat and mass transfer model. This manifests itself in the fact that melting takes place mainly on the outside of the snowflake. Moreover, due to the Chilton-Colburn analogy between heat transfer, mass transfer and momentum transfer, the same arguments that justify the use of the convex shape approximation for the calculation of the drag coefficient in section 2.3 can be applied here for heat and mass transfer coefficients. It should be noted that these convex shapes must be interpreted as porous bodies in order for them to enable the imbibition of meltwater.

For simplicity and in order to describe the geometry with a minimum number of descriptors, the snowflake is approximated as an ellipsoid. Compared to a sphere, an ellipsoid offers more flexibility in describing very elongated or flat particles. Nonetheless, only few parameters are sufficient to define the geometry of an ellipsoid. A two-dimensional representation of the shape approximation of a melting snowflake with an ellipse is illustrated in Figure 3.10.

The major axis of the ellipsoid is given by the maximum Feret diameter $d_{\max}$ of

the particle. The minor axis is defined by

$$d_\perp = AR\, d_{\max} \tag{3.7}$$

with the particle aspect ratio AR. Commonly only two-dimensional projections of natural snowflakes are available and the three-dimensional descriptors are not known. Therefore, the intermediate axis of the ellipsoid is approximated by the geometric mean of the major and minor axis, i.e., $\sqrt{d_{\max} d_\perp}$. This approximation has already been suggested by Magono and Nakamura [121]. With the aspect ratio the intermediate axis can be written as $\sqrt{AR} d_{\max}$. However, in cases where the three-dimensional geometry of a snowflake is known, the factor in front of the maximum Feret diameter can be substituted with the corresponding aspect ratio.

The ellipsoid used for approximating the convex shape of the particle is now fully defined by the maximum Feret diameter and the aspect ratio. While the maximum Feret diameter can be obtained by the equations above, the aspect ratio is modeled based on experimental findings and geometrical considerations.

The experimental results presented above, indicate that the aspect ratio of a melting snowflake remains approximately constant in the first stage of melting, i.e., until the liquid phase starts to affect the apparent shape of the particle. The instant at which the aspect ratio is influenced by the liquid phase is estimated from the volume of the ellipsoid, as explained in the following. The volume of the resulting liquid drop marks the lower bound for the ellipsoid volume, since the particle in this state exhibits the maximum bulk density throughout the melting process. Since the density of liquid water and ice are similar and the liquid phase is expected to influence the apparent shape at the instant when all pores are saturated with meltwater, an inequality can be formulated. The ellipsoid volume must be greater than or equal to the drop volume. The aspect ratio is then considered equal to the initial aspect ratio of the dry flake until the ellipsoid volume reaches the drop volume, which marks the instant from which the liquid is assumed to significantly affect the shape of the melting snowflake. Subsequently, the aspect ratio is calculated such that the ellipsoid volume equals the drop volume.

This procedure yields an aspect ratio, which is constant at first, then gradually increases and remains at unity once the residual ice is fully enclosed by the meltwater. This is in qualitative agreement with the experimental results presented above.

Heat and mass transfer model

Initially, the snowflake can have a temperature below 0 °C. In this case, the particle will first heat up to the melting temperature before the ice starts to melt. The ratio of sensible heat required for this process to the latent heat needed to melt the particle is given by the Stefan number. For the experiments conducted in this study, the Stefan number is much smaller than unity, which indicates that sensible heat plays a minor role when compared to latent heat.

Heat conduction inside the particle is neglected in the following for two reasons: First, when the outer branches of the snowflake start to melt and meltwater is imbibed by the porous snowflake, the transported meltwater will quickly heat up the inner structure of the snowflake to the melting temperature. Second, the Biot number of the particle is small, which indicates that the process is dominated by convective heat transfer at the particle surface rather than heat conduction inside the particle. Therefore, the particle temperature can be approximated as uniform.

The energy balance of a melting snowflake can then be written as

$$h_\mathrm{h} A(T_\mathrm{a} - T_\mathrm{m}) = \dot{m}_\mathrm{f} L_\mathrm{f} - h_\mathrm{m} \rho_\mathrm{a} A(\omega_\mathrm{a} - \omega_\mathrm{s}) L_\mathrm{v} \tag{3.8}$$

where T_a denotes the air temperature, T_m the melting temperature, ω_a the vapor mass fraction of the incoming air, ω_s the vapor mass fraction at the particle surface, h_h the heat transfer coefficient, h_m the mass transfer coefficient, A the particle surface area, ρ_a the air density, $\dot{m}_\mathrm{f}$ the melting rate, L_f the latent heat of fusion and L_v the latent heat of evaporation. The left-hand side of this equation represents the convective heat transfer from the warm air to the particle. The first term on the right-hand side represents latent heat due to melting of ice and the second term corresponds to latent heat due to evaporation. The air at the particle surface is assumed to be saturated with water vapor. Evaporation can withdraw heat from the particle and conversely, condensation can transfer heat to the particle.

The surface area of the particle, over which heat is transferred and water evaporates, is calculated from the geometrical approximation as an ellipsoid described above.

The heat transfer coefficient of the ellipsoid is approximated by that of a volume equivalent sphere. The sphericities of the ellipsoids representing the laboratory-generated snowflakes are close to unity. Therefore, deviations of the heat transfer coefficient of a sphere are expected to be small. Thus, the heat transfer coefficient and the mass transfer coefficient are calculated from correlations for the Nusselt number and Sherwood number of a sphere, respectively. The diameter of a sphere with a volume equal to that of the ellipsoid defined above is given by

$$d_\mathrm{eq} = \sqrt{AR}\, d_\mathrm{max}. \tag{3.9}$$

This volume equivalent diameter designates the characteristic length for calculating the Reynolds number Re, Nusselt number Nu and Sherwood number Sh. The utilized correlations proposed by Frössling [58] are given by

$$Nu = \frac{h_\mathrm{h} d_\mathrm{eq}}{k_\mathrm{a}} = 2 + 0.552 Re^{1/2} Pr^{1/3} \tag{3.10}$$

$$Sh = \frac{h_\mathrm{m} d_\mathrm{eq}}{D_\mathrm{v,a}} = 2 + 0.552 Re^{1/2} Sc^{1/3} \tag{3.11}$$

with the thermal conductivity of air k_a, Prandtl number Pr, diffusivity of water vapor in air $D_\mathrm{v,a}$ and Schmidt number Sc.

Rearranging the energy balance given by Equation 3.8 and utilizing the Nusselt number and Sherwood number to estimate the heat and mass transfer coefficients yields

$$\frac{\mathrm{d}m_\mathrm{i}}{\mathrm{d}t} = -\frac{A}{d_\mathrm{eq} L_\mathrm{f}} \left[Nu k_\mathrm{a} (T_\mathrm{a} - T_\mathrm{m}) + Sh D_{\mathrm{v,a}} \rho_\mathrm{a} (\omega_\mathrm{a} - \omega_\mathrm{s}) L_\mathrm{v} \right], \tag{3.12}$$

which represents an ordinary differential equation for the calculation of the ice mass of the particle. In this equation, the particle surface area A and the volume equivalent diameter d_eq have to be obtained from the structural model described above. Furthermore, the Nusselt number and Sherwood number are functions of the Reynolds number and thus also depend on the particle size.

In order to evaluate the model, Equation 3.12 can be solved numerically for which the size of the residual ice must be obtained from the mass–size power law given by Equation 3.4. Alternatively, Equation 3.5 can be used to eliminate the melting rate from Equation 3.12, which yields a differential equation for the size of the residual ice.

3.3.2 Model validation

To validate the proposed model, it is compared with the experimental results in the following.

The experimental conditions, which include the air temperature, the humidity and the relative velocity of the particle to the airflow, are available from the measurements. Furthermore, the model requires the initial maximum Feret diameter of the snowflake, its aspect ratio and its mass as input parameters. In addition, the parameters α and β in the mass–size power law have to be obtained. Since these parameters are related to the mass and the maximum dimension of the snowflake, one of these quantities can be calculated when the other three are known. For natural snowflakes, for which the mass has not been measured, the initial mass can be estimated by evaluating the mass–size power law with the parameters α and β for the corresponding morphological class taken from literature. However, as the masses of the laboratory-generated snowflakes used in the experiments are known and the mass fractal diameter β is assumed to be the same for all snowflakes, the parameter α can be calculated from the mass–size power law.

Accordingly, the mass fractal dimension β represents the only free parameter that cannot be obtained for each individual snowflake by direct measurement. In theory, this can be retrieved by fitting a power law to the mass–size relationship, as shown in Figure 3.4. However, while this approach yields precise values for natural snowflakes of the same morphological class as demonstrated in literature, variations in the laboratory-generated snowflakes introduce a notable uncertainty in the experimentally obtained mass fractal dimension. Nonetheless, the fitted mass–size relation provides confidence bounds in which the true parameter is expected.

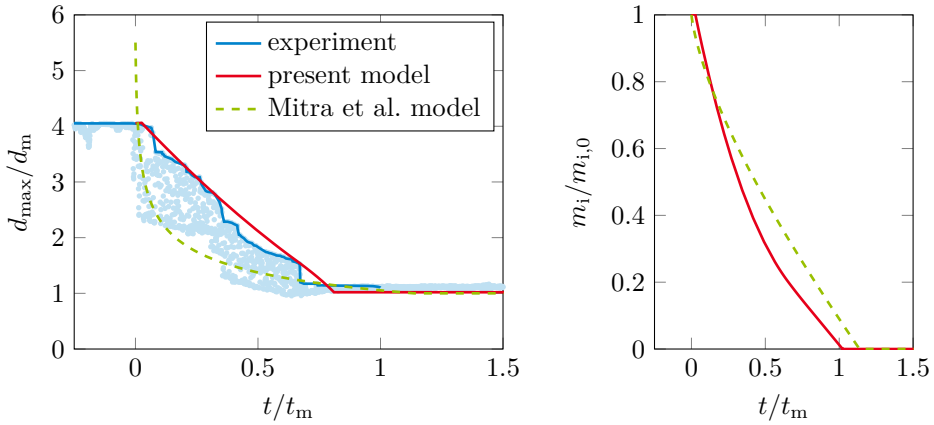

(a) Predicted size evolution **(b)** Predicted evolution of ice mass

Figure 3.11: Model validation with the evolution of the maximum Feret diameter for an exemplary experimental run (a) and the numerically predicted mass fraction of the remaining ice (b). The time is normalized with the experimentally measured melting duration.

Following a parameter study, the value $\beta = 2$ is found to show the best agreement with the experimental results. This value is well within the confidence bounds of the fitted mass–size relationship and is consistent with values for snowflakes of similar morphology found in literature.

In Figure 3.11a, the evolution of the maximum dimension of an exemplary snowflake is shown in comparison to the model prediction. Each data point represents the maximum Feret diameter measured from the two-dimensional projection captured by the camera in one video frame. However, the model is based on the three-dimensional maximum Feret diameter, which must be greater than or equal to the two-dimensional value. Thus, the evolution of the three-dimensional maximum Feret diameter is approximated by the upper envelope of the data points. The numerically predicted size evolution matches the experimentally measured values well. In general, the model prediction agrees well with the experimentally measured size evolution for the entire data set.

Furthermore, the evolution of the maximum dimension predicted by the model of Mitra et al. is shown in Figure 3.11a. This model does not take the initial size of the snowflake into account, but instead calculates the size from a prescribed initial bulk density. Hence, the initial value does not match the experimentally measured value. Moreover, the model of Mitra et al. mostly underestimates the maximum dimension.

Finally, in Figure 3.11b, the mass fraction of the remaining ice as predicted by the two models is shown as a function of time. However, these predictions cannot be validated by experimental measurements directly, since the melted fraction

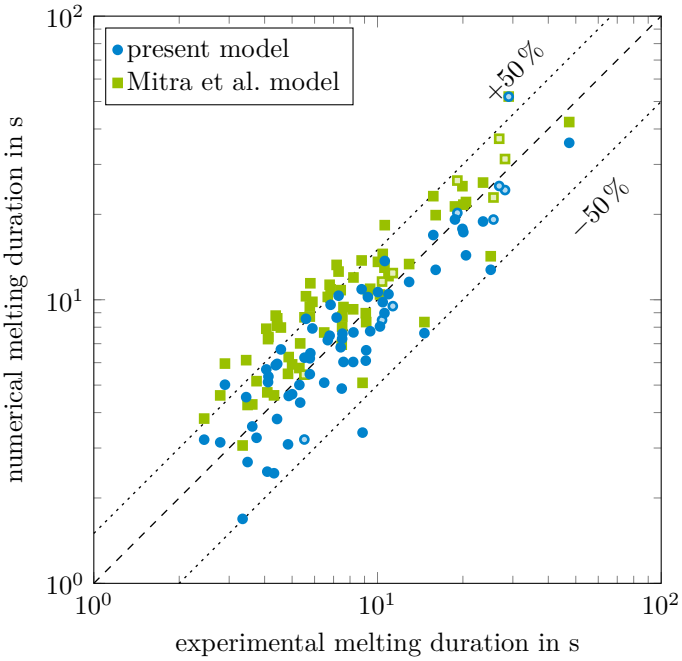

Figure 3.12: Comparison of the numerically predicted melting durations with the experimentally measured melting durations. Snowflakes melted in dry air are indicated separately in lighter colors.

of the snowflake is not accessible from the experiments. Nonetheless, the total duration of the melting process can be obtained from the model as well as from the experiments, which can be used to further validate the proposed model.

Figure 3.12 shows a comparison of the numerically predicted melting durations with the experimentally measured durations for all experimental runs. The comparison is performed for the present model as well as for the model of Mitra et al. While the scatter is similar for both models, the model of Mitra et al. slightly overpredicts the melting duration. In average, the newly proposed model appears to fit the data well.

The deviations between the melting durations predicted by the present model and those measured from the experiments is mostly attributed to the fact that the laboratory-generated snowflakes only moderately followed the assumed mass–size relationship. In comparison to the laboratory-generated snowflakes, natural snowflakes were usually found to show a better agreement with the mass–size power law. One potential cause is that not all fractal aspects of natural snowflakes are represented in sufficient detail in the artificial snowflakes. Furthermore, the utilized snowflakes could be assigned to different morphological classes, which could lead to a stronger correlation in the mass–size relationship. An improved agreement of

the snowflakes with the mass–size power law would presumably result in a more accurate prediction of the melting process.

A major difference between the present model and the model of Mitra et al. is in the underlying assumptions. The model of Mitra et al. is based on empirical correlations for the size, shape and density of the melting snowflake. Each of these quantities is assumed as a linear function of the melted mass fraction of the snowflake. Due to this formulation, the model of Mitra et al. does not take the initial snowflake size into account. Furthermore, the model does not consider the individual morphological classes of snowflakes.

In contrast, the model developed in the present study is based on a mass–size power law, which is widely accepted for the description of snowflakes and various other types of aggregates. Furthermore, the model takes the initial size and aspect ratio of the snowflake into account and makes use of this information by constructing an ellipsoid to approximate the convex shape of the particle. Finally, the new model can be applied to snowflakes of various morphological classes by employing the corresponding values for α and β, which can be found in literature. Thus, the model is not only applicable to snow aggregates but also to graupel and common ice crystals, which can be represented by higher mass fractal dimensions.

3.4 Summary

An experimental setup for the observation of the melting process of snowflakes in forced convection has been developed and used to quantify the particle shape evolution during melting. Based on the experimental findings, a novel theoretical model has been derived to describe the melting of snowflakes. The proposed model accounts for the imbibition of the generated liquid water by the porous particle due to capillary forces. Therefore, the liquid water does not contribute to the apparent shape of the particle during the first melting stage. This enables using the mass–size relationship for the morphological class of the snowflake for modeling the particle size evolution.

The model is validated by comparing the predicted evolution of the particle maximum dimension with the experimental measurements. A further validation is provided by the comparison of the theoretically predicted and experimentally measured melting duration. The model predictions exhibit a good agreement with the experimental results, which indicates an adequate representation of the relevant physical phenomena.

A finer classification of the generated snowflakes could yield a stronger correlation of snowflake mass and size for the different morphological classes. This would result in a more precise mass fractal dimension, which appears as an exponent in the mass–size power law, and could lead to an improved prediction of the melting process.

The proposed model requires less empirical correlations than previous models

in literature. The major assumption underlying the model is that the particle follows a mass–size power law, which is widely accepted in literature. The model formulation allows to account for different snowflake morphologies and sizes. The appropriate parameters of the mass–size relationship for various morphological classes of snowflakes can be found in literature. By using suitable values, the model is also applicable to other ice particles such as graupel, hailstone or single crystals. The experimental findings and the proposed model enable an improved prediction of icing in snow conditions and can enhance models for weather prediction.

Part II

Liquid water transport in porous ice layers

4 Imbibition into granular ice layers

Water transport in granular ice and snow layers plays a critical role in aircraft icing and in various other applications, including the prediction of wet snow avalanches, glacier evolution and icing of structures such as solar panels, power lines and other devices exposed to cold environments [196, 83, 53]. However, the phenomena related to water distribution in granular ice layers and the influences of the properties of the medium are still not fully understood.

In this chapter, the imbibition of water into a melting granular ice layer is experimentally investigated. In order to study this effect, a capacitive sensor is designed to quantify the liquid distribution in the porous medium. The developed measurement device is employed to characterize the effects of porosity, grain size and volume flux supplied by melting of the ice.

First, the experimental methods, consisting of the production of the porous ice layers, the sensor and the setup for melting the samples are described. Second, the phenomena observed in the experiments are reported and wetting of the pores is delineated. Finally, the measured liquid distribution and the effects of porosity, grain size and volume flux are analyzed.

4.1 Experimental methods

The investigation of the water transport in granular ice layers requires reproducible specimen with known properties, a measurement instrument, which is capable of resolving the water content in space and time, and an experimental setup to conduct the experiments under controlled conditions.

In this section, first the methodology for the production of granular ice layers is described. Second, the design of the sensor is outlined and the calibration of the device is explained and finally, the experimental setup in which the sensor is employed is presented.

4.1.1 Granular ice layer production

For the investigation of the water transport in a melting granular ice layer, the specimen should be reproducible and their porosity and ice crystal grain size distribution need to be specified. Therefore, at first ice crystals need to be produced and characterized. Subsequently, the ice crystals are compressed to a granular ice layer with a known porosity.

The production of ice crystals, their characterization and the further processing

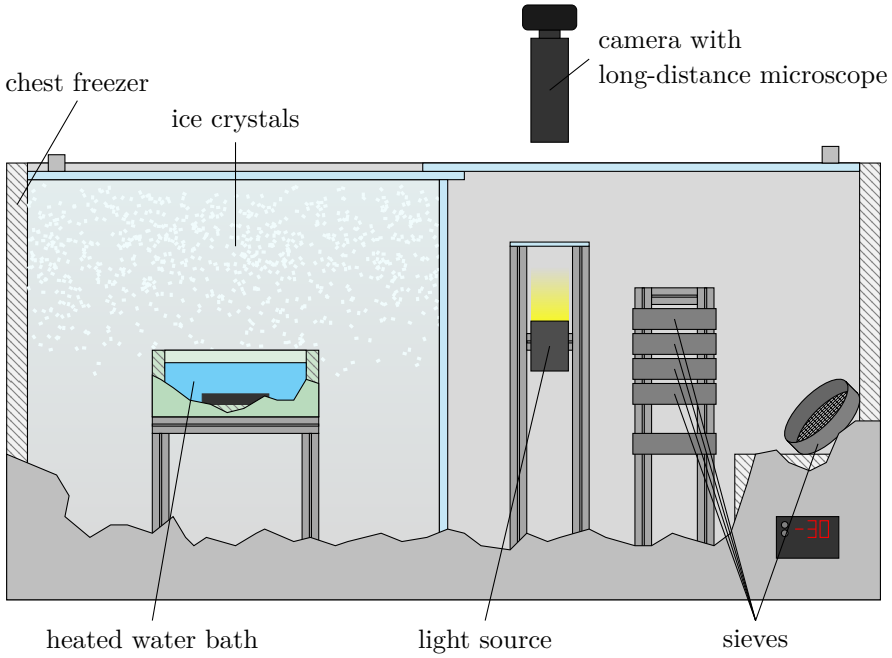

Figure 4.1: Chest freezer divided in two parts: The ice crystal production on the left and the crystal characterization setup, sieves and ice layer mold on the right.

to a granular ice layer takes place in a chest freezer, which is shown in Figure 4.1. In order to generate ice crystals for the experiments, a heated containment with filtered water is placed inside a sealed compartment of the chest freezer for multiple hours. The water evaporates and humidifies the air in the chest freezer. Consequently, water desublimates on the cold chest freezer walls and a frost layer grows. The type of ice crystals that grows is determined by the temperature and degree of supersaturation at the location of desublimation. Due to a temperature stratification inside the chest freezer, the walls exhibit a temperature that increases with height, which leads to a variety of ice crystals that are formed and which are similar to those identified in clouds.

These ice crystals are scraped off the walls and transported to a less humid environment in a second compartment of the freezer where they are sieved. Multiple sieves with different mesh sizes are used to separate the ice crystals into several crystal grain size classes. The five utilized sieves have mesh sizes of 900 µm, 710 µm, 600 µm, 450 µm and 154 µm. The sieving procedure is performed analogously to the steps described in DIN 66165-2:2016-08 [52]. The topmost sieve of 900 µm mesh size is used to filter all large ice crystals, which are not used for the experiments. Similarly, none of the very small ice crystals that fall through the last sieve with a mesh size of 154 µm are used in the experiments. Within seconds after the sieving,

the ice crystals sinter together and form larger agglomerates. Prior to any further processing these agglomerates are disrupted by shaking the sieve again. To ensure repeatability and to prevent a significant change of the particle morphology due to sublimation and desublimation, the produced ice crystals are used within a few hours.

Characterization of ice crystals

In the following, an analysis of the grain size distribution is presented. The single ice crystals determine the microscopic structure of the pores in the granular layer, which can affect the imbibition process. Therefore, a characterization of the ice crystals on each sieve is performed. For this purpose, the sieved ice crystals are placed on a glass plate above a light source. The ice crystals are then recorded with a camera and a long-distance microscope positioned outside of the chest freezer. Exemplary ice crystals from different sieves are shown in Figure 4.2. The laboratory-generated ice crystals appear similar to natural ice crystals as they exist in ice clouds.

For an accurate characterization of the ice crystal size and shape distribution, more than one thousand ice crystals have been captured per mesh size. These photographs have subsequently been analyzed with respect to their area equivalent diameter and Cox roundness. The obtained probability density function of the

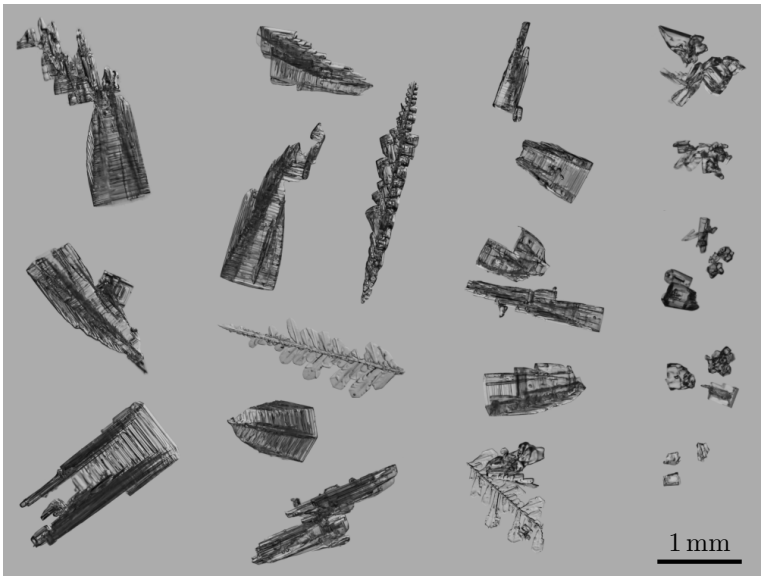

Figure 4.2: Exemplary ice crystals produced in the chest freezer and remaining on the different sieves. Each column corresponds to a mesh size, which are 710 µm, 600 µm, 450 µm and 154 µm (from left to right).

area equivalent diameters of the ice crystals from each sieve is shown with a fitted log-normal distribution in Figure 4.3. The probability density function of the log-normal distribution is given by

$$f(d) = \frac{1}{\sqrt{2\pi}\sigma d} \exp\left(-\frac{(\ln d - \mu)^2}{2\sigma^2}\right), \tag{4.1}$$

with the parameters μ and σ. The median ice crystal grain sizes are measured as 240 µm, 583 µm, 647 µm and 867 µm.

Similarly, the Cox roundness is evaluated as a measure for the sphericity of the ice crystals. The data for the sieved ice crystals are shown in Figure 4.4. It appears that the smallest ice crystals are slightly more spherical than the other ice crystals. However, the median Cox roundness is close to 0.6 for all mesh sizes.

Granular ice layer properties

Following the production and sieving of the ice crystals, the particles are placed into a mold with a cross-section of 30 mm × 30 mm. The mass of the ice crystals in the mold is weighed in order to determine the porosity of the final ice layer. The ice crystals in the mold are then compressed to a thickness of 3.1 mm. By weighing the amount of ice, the porosity, i.e., the void volume fraction of the granular ice layer can be controlled and is commonly within 1 % of the target value.

This procedure enables the generation of granular ice layers with a known porosity and grain size distribution. In order to investigate the homogeneity of the produced ice layers, micro-computed tomography scans of multiple ice layers are performed. An exemplary section of an ice layer is presented in Figure 4.5. An analysis of the scans suggests a uniform porosity on length scales sufficiently larger than the particle size. Furthermore, following a comparison of different scans, no indications for particle fragmentation have been detected. Therefore, it is assumed that the particle size distribution prior compression of the crystals closely resembles the grain size in the produced granular ice layer.

4.1.2 Capacitive sensor design

The sensor developed in this study is based on the measurement of the capacitance between two electrodes. The measured capacitance depends linearly on the effective relative permittivity of the medium between the electrodes, which in turn, is a function of the liquid volume fraction of the granular ice layer. At the utilized excitation frequency of the electric field, the relative permittivity of liquid water is much higher than that of ice and air, enabling a quantification of the local water content with the developed sensor.

The idea underlying a space and time resolving water content sensor is to distribute multiple sensor and ground electrode pairs over the height of an ice layer

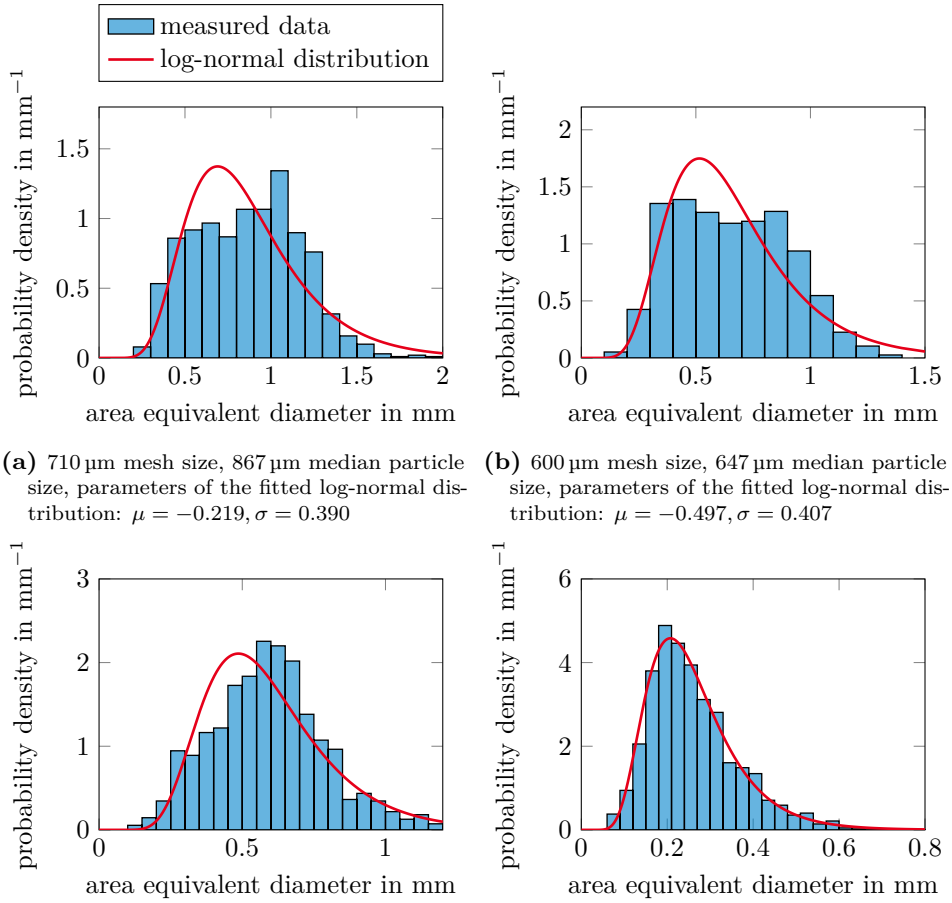

(a) 710 µm mesh size, 867 µm median particle size, parameters of the fitted log-normal distribution: $\mu = -0.219, \sigma = 0.390$

(b) 600 µm mesh size, 647 µm median particle size, parameters of the fitted log-normal distribution: $\mu = -0.497, \sigma = 0.407$

(c) 450 µm mesh size, 583 µm median particle size, parameters of the fitted log-normal distribution: $\mu = -0.588, \sigma = 0.364$

(d) 154 µm mesh size, 240 µm median particle size, parameters of the fitted log-normal distribution: $\mu = -1.422, \sigma = 0.389$

Figure 4.3: Probability density functions and fitted log-normal distributions for the area equivalent diameters of the ice crystals on the different sieves.

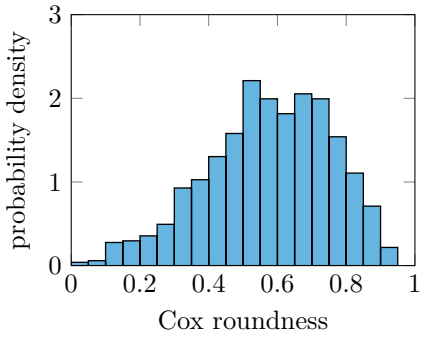

(a) 710 µm mesh size, median Cox roundness of 0.585

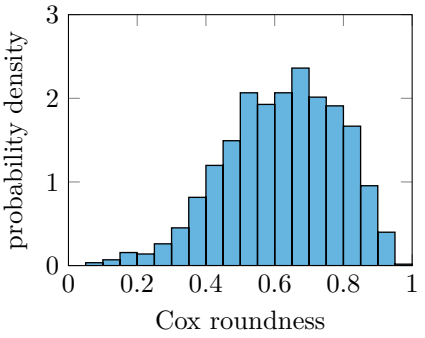

(b) 600 µm mesh size, median Cox roundness of 0.631

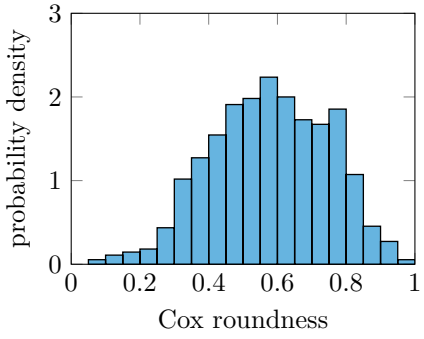

(c) 450 µm mesh size, median Cox roundness of 0.578

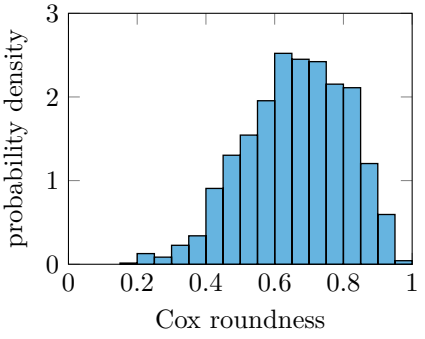

(d) 154 µm mesh size, median Cox roundness of 0.669

Figure 4.4: Probability density functions for the Cox roundness of the ice crystals on the different sieves.

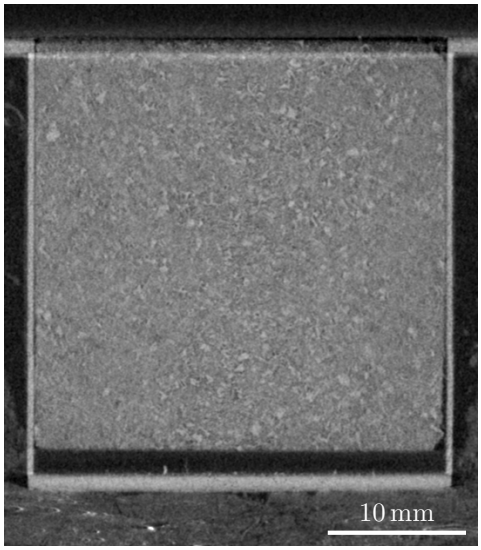

Figure 4.5: Micro-computed tomography scan of an exemplary ice layer with a porosity of 0.3 and a median ice crystal grain size of 647 µm. The specimen is enclosed in an insulating housing to prevent melting.

and thus sample the time resolved water content at different positions. Hence, the number of electrodes on the device determines the spatial resolution.

In order to maintain an unobstructed view on the melting ice layer, the sensor is designed on a single printed circuit board (PCB), which can be positioned on one side of the sample, while visual observation is possible from the opposite side. In contrast to a parallel plate capacitor, the electrodes are located in the same plane and the fringe capacitance is utilized to indirectly measure the liquid volume fraction in the ice layer. In Figure 4.6a, a set of electrodes and the geometrical arrangement is illustrated. The set of electrodes consists of one sensor electrode (red) surrounded by two ground electrodes (green) on the PCB with an ice layer in front of it, which is represented by the partially transparent blue block. Figure 4.6b shows a cross-section of the domain, indicating the electric field lines penetrating the ice layer. The illustrated field lines are obtained from a simulation of the electric field. Due to symmetry, only half of the geometry is simulated and depicted. The simulation is based on a simplified geometry and any coupling with neighboring sensor strips is neglected. The electrical flux density field obtained from the simulations can be used to calculate the capacitance between the electrodes.

In Figure 4.6 it can be recognized that the electric field lines are denser near the plane of the electrodes than further in the ice layer, visualizing a higher electric flux density near the electrode plane. Hence, the sensor sensitivity is decreasing with increasing distance to the electrode plane. Therefore, in order to interpret the measured capacitance as an average value over the thickness of the ice layer,

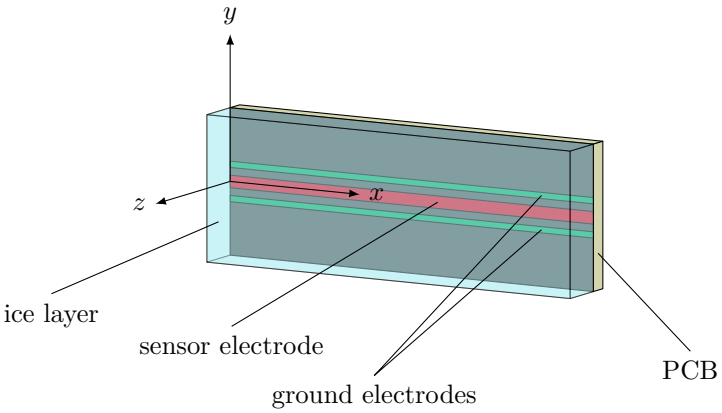

(a) Geometry of the electrodes and positioning of the ice layer

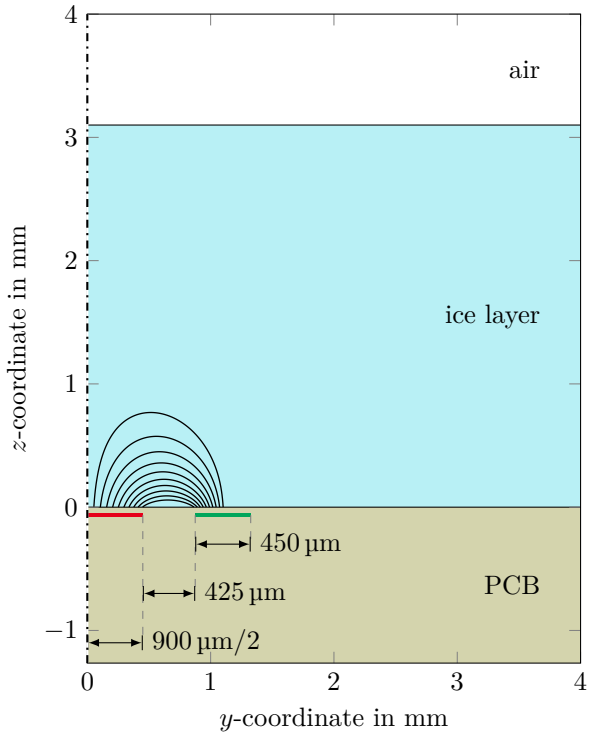

(b) Two-dimensional representation with electric field lines

Figure 4.6: Alignment of a single set of sensor and ground electrodes with an ice layer in front (a). Visualization of the electric field lines in the ice layer in a two-dimensional representation on one side of the plane of symmetry (b).

the distribution of liquid water in the direction perpendicular to the sensor plane, i.e., the vertical direction in Figure 4.6b, must be approximately uniform. This imposes a condition that must be met in the design of the experimental setup.

Electrode dimensions

In a parameter study, the influences of the sensor and ground electrode width as well as the gap width between them are investigated. The aim of the parameter study is to determine the optimum electrode dimensions, such that the difference in capacitance due to the presence of water wetting the ice layer is maximized. However, the measurement range of the capacitance-to-digital converter (FDC1004 from Texas Instruments) used to evaluate the capacitance should not be saturated. Furthermore, to achieve a sufficient spatial resolution of the sensor, it is beneficial to place the sensor strips densely together. In the following, the findings from the parameter study are summarized.

While a small gap width increases the capacitance of the system, it also significantly reduces the depth to which the electric field penetrates the ice layer. Conversely, the sensitive region should not be larger than the thickness of the ice layer to minimize the parasitic capacitance introduced by the field beyond the medium.

The effect of the width of the ground electrode on the capacitance appears to be small. Therefore, this width can be reduced to save space and improve the spatial resolution.

The width of the sensor electrode has a significant effect on the measured capacitance. However, the width has to be be limited to maintain a sufficient spatial resolution.

Based on these considerations and after testing of a prototype, the sensor electrode width was set to 900 µm and the widths of the ground electrodes to 450 µm. The gap width was set to 425 µm, which yields a distance of 2.2 mm until the pattern repeats, which defines the spatial resolution. The final dimensions of the electrodes are shown in Figure 4.6b.

Since the magnitude of the electric field increases in the vicinity of the electrode plane, the sensor is highly sensitive to liquid water getting in contact with the sensor surface. For granular ice layers close to saturation, when a thick liquid film covers the entire surface of the ice grains in contact with the sensor, the sensor can get partially wetted, which causes a sharp increase in measured capacitance and inhibits the evaluation of the signal. This limits its application to specimen well below saturation.

Sensor layout

For the realization of the sensor, a PCB is designed, which incorporates twelve sensor electrodes and the electronics to evaluate the capacitances. The latter

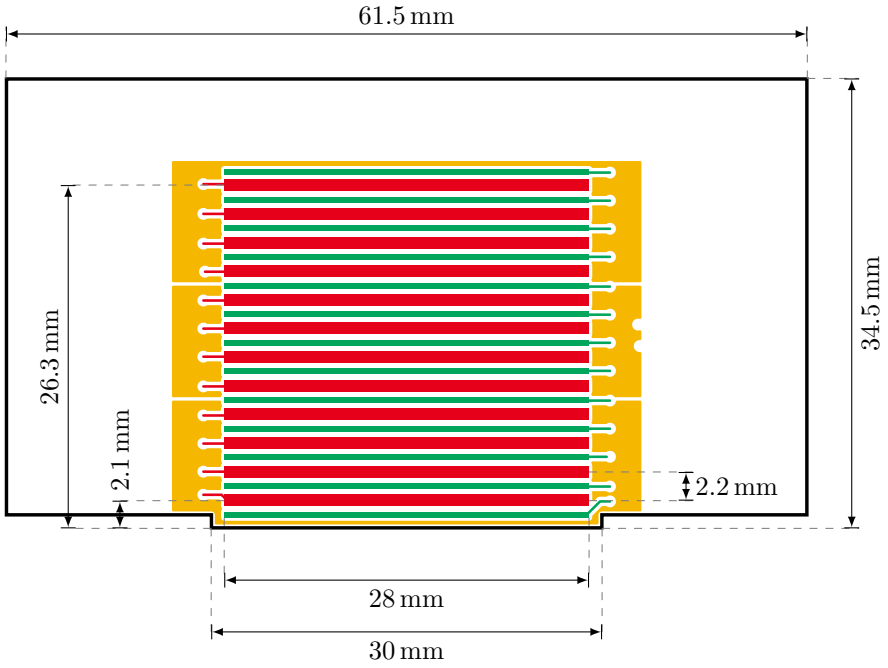

Figure 4.7: Schematics of the electrode layout on the sensor PCB. A copper layer with alternating ground (■) and sensor electrodes (■) and part of the shielding (■) surrounding the electrodes.

is achieved with three capacitance-to-digital converters (FDC1004 from Texas Instruments) and an I^2C multiplexer to address the capacitance-to-digital converters individually. Each of the capacitance-to-digital converters provides four channels to measure capacitances and an active shield, which can be used to minimize parasitic capacitances between the electrodes and other parts in the vicinity of the sensor.

The PCB consists of three copper layers. The top layer is covered by a 50 µm thick prepreg layer, i.e., a fiberglass mat with resin, which is used to smooth the surface of the 18 µm thick copper structure comprising the electrodes. On top of the prepreg layer, an approximately 15 µm thick black solder mask, i.e., a polymer coating, provides a high contrast between the PCB and the granular ice. The top copper layer with the twelve electrode pairs is shown in Figure 4.7. This copper layer also contains part of the shielding, which reduces the parasitic capacitance between the electrodes and the surroundings. Below this copper layer follows a 1.2 mm thick layer of FR-4, i.e., a glass-reinforced epoxy laminate, after which a copper layer with shielding follows. This way, the electronic components placed at the back of the PCB do not affect the measurement of the electrodes on the front. Another layer of prepreg is followed by a final copper layer with traces for the electronic components, which then follow the solder mask on the backside.

The center of the bottom sensor electrode is located 2.125 mm above the bottom edge of the PCB and the top most sensor electrode is centered at 26.325 mm above the bottom edge. Sensors are placed every 2.2 mm. As mentioned above, the sensor electrodes have a width of 0.9 mm and the ground electrodes have a width of 0.45 mm each.

At the back of the PCB, a connector is used to link the I^2C multiplexer and the connected capacitance-to-digital converters to a microcontroller, which acquires the data and communicates with a computer.

4.1.3 Sensor calibration

The calculation of the distribution of liquid water from the obtained capacitances is performed in two steps: First, possible offsets in capacitance and sensitivity are eliminated and second, the standardized capacitance readings are converted to liquid volume fractions by making use of knowledge of the total liquid volume inside the granular ice layer from the captured video.

Due to minor variations in routing on the sensor PCB and its proximity to the heating film, differences in sensitivity and offsets in capacitance can arise among the sensor strips. To standardize the capacitance readings, the sensitivities of the sensor strips are assessed by measuring the capacitances acquired when different materials with varying relative permittivities are positioned in front of the sensor. Samples include air, PTFE (polytetrafluoroethylene), acrylic glass, polyamide and gypsum. Due to the linear relationship between capacitance and relative permittivity, the relation between the different capacitances of the sensor strips is linear. Thus, a linear regression of the data points provides offset and sensitivity of each sensor strip. The sensor strips are then standardized to provide the same output value when exposed to the same material and therefore the same relative permittivity.

The standardized capacitance is defined such that it equals zero at the start of the experiment, by subtracting the initial value at each experiment.

The second calibration step requires a relationship between the standardized capacitance reading and the liquid volume fraction of the segment of the ice layer in front of the sensor strip. One possible approach is to convert the capacitance to a relative permittivity and then use a relationship like that proposed by Currie and Fuleki [44] to calculate the liquid fraction. However, the relative permittivity of ice at the excitation frequency of 25 kHz used by the capacitance-to-digital converters differs significantly from that of air. Therefore, the function to convert the relative permittivity to a liquid fraction will also depend on the porosity of the ice layer, which complicates the calibration procedure.

In the present work, a different approach is proposed, which is based on the knowledge of the total liquid volume in the granular ice layer. A video recording of the melting ice layer is synchronized with the capacitance measurement. Therefore, the amount of melted ice an thus the total liquid volume can be obtained via image

processing at any given time. The liquid volumes measured by each sensor strip must sum up to this total liquid volume at each instance in time.

The standardized capacitance is a function of the liquid volume fraction, which however is not known beforehand. This relationship is approximated by a Taylor polynomial

$$v_{\mathrm{liq}}(C_{\mathrm{std}}) = b_0 + b_1 C_{\mathrm{std}} + b_2 C_{\mathrm{std}}^2 + b_3 C_{\mathrm{std}}^3 + \mathcal{O}(C_{\mathrm{std}}^4), \tag{4.2}$$

with the liquid volume fraction v_{liq} and the standardized capacitance C_{std}. The coefficients b_0, b_1, b_2 and b_3 have to be obtained by combining the knowledge of the capacitance readings and the total liquid volume.

Following the experimental procedure described above, the initial liquid volume fraction is zero everywhere in the ice layer. Furthermore, according to its definition, the standardized capacitance equals zero at the start of the experiment. Thus, it follows that the coefficient b_0 is zero.

The sum of the volume of liquid in front of each of the twelve sensor strips must be equal to the total volume of liquid in the granular ice layer at each point in time. This can be expressed as

$$V_{\mathrm{liq}}(t) = \sum_{i=1}^{12} v_{\mathrm{liq}}(C_{\mathrm{std},i}(t)) V_i(t) \tag{4.3}$$

with the total liquid volume V_{liq}, time t and the volume of the porous medium in front of each sensor strip V_i. The latter is a function of time, since the sensor strips can be uncovered when the ice layer slides down during melting. Making use of the Taylor polynomial up to terms of third order, this equation can be rewritten as

$$V_{\mathrm{liq}}(t) = b_1 \sum_{i=1}^{12} C_{\mathrm{std},i}(t) V_i(t) + b_2 \sum_{i=1}^{12} C_{\mathrm{std},i}(t)^2 V_i(t) + b_3 \sum_{i=1}^{12} C_{\mathrm{std},i}(t)^3 V_i(t), \tag{4.4}$$

which can be written as a matrix equation

$$\begin{bmatrix} V_{\mathrm{liq}}(t_1) \\ V_{\mathrm{liq}}(t_2) \\ \vdots \\ V_{\mathrm{liq}}(t_N) \end{bmatrix} = \sum_{i=1}^{12} \begin{bmatrix} C_{\mathrm{std},i}(t_1) V_i(t_1) & C_{\mathrm{std},i}(t_1)^2 V_i(t_1) & C_{\mathrm{std},i}(t_1)^3 V_i(t_1) \\ C_{\mathrm{std},i}(t_2) V_i(t_2) & C_{\mathrm{std},i}(t_2)^2 V_i(t_2) & C_{\mathrm{std},i}(t_2)^3 V_i(t_2) \\ \vdots & \vdots & \vdots \\ C_{\mathrm{std},i}(t_N) V_i(t_N) & C_{\mathrm{std},i}(t_N)^2 V_i(t_N) & C_{\mathrm{std},i}(t_N)^3 V_i(t_N) \end{bmatrix} \cdot \begin{bmatrix} b_1 \\ b_2 \\ b_3 \end{bmatrix}. \tag{4.5}$$

This equation represents a system of linear equations with three unknowns b_1, b_2 and b_3 and N equations, where N corresponds to the number of available video frames after the start of the experiment. The equation, which would correspond to the initial condition, i.e., $V_{\mathrm{liq}}(t_0) = 0$, is not included here, since it was already used to determine $b_0 = 0$. Due to the large number of captured video frames, the system of equations is overdetermined, which allows to evaluate the coefficients

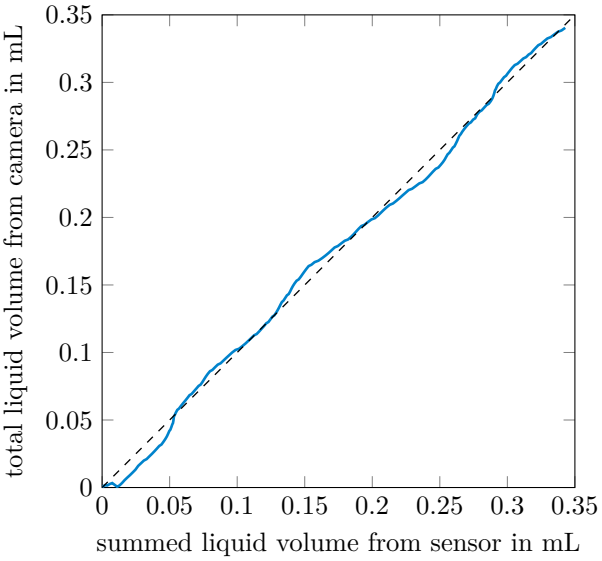

Figure 4.8: Comparison of the total liquid volume in a granular ice layer with the sum of the liquid volumes measured by the sensor. The total liquid volume is evaluated by processing the melted fraction of the ice layer from a video. The dashed line corresponds to perfect agreement. The maximum deviation in the depicted data is 12 µL.

such that the sum of squared residuals is minimized. This least squares approach provides a robust result for the coefficients of the Taylor polynomial. Furthermore, for increased robustness, the residuals are weighted with a bisquare scheme.

Once the coefficients are obtained, the Taylor polynomial given by Equation 4.2 can be evaluated to calculate the liquid volume fraction at each sensor strip. Figure 4.8 shows a comparison of the total liquid volume in a granular ice layer calculated from the image processing and the sum of the sensor readings. The good agreement throughout the experimental run with only three fitted parameters indicates that the utilized Taylor polynomial is able to adequately express the relation between standardized capacitance and liquid volume fraction.

With this method, the conversion from capacitance to liquid volume fraction can be performed for each experimental run individually. This provides the benefit that the conversion is independent of the ice layer porosity and grain size. Furthermore, the *in situ* calibration minimizes errors due to differences in the positioning of the ice layer and other variations in the experiments.

4.1.4 Experimental setup

In order to investigate the imbibition of meltwater into a granular ice layer, a controlled environment is required to conduct the experiments. This is realized in an experimental setup, which utilizes the granular ice layer under investigation

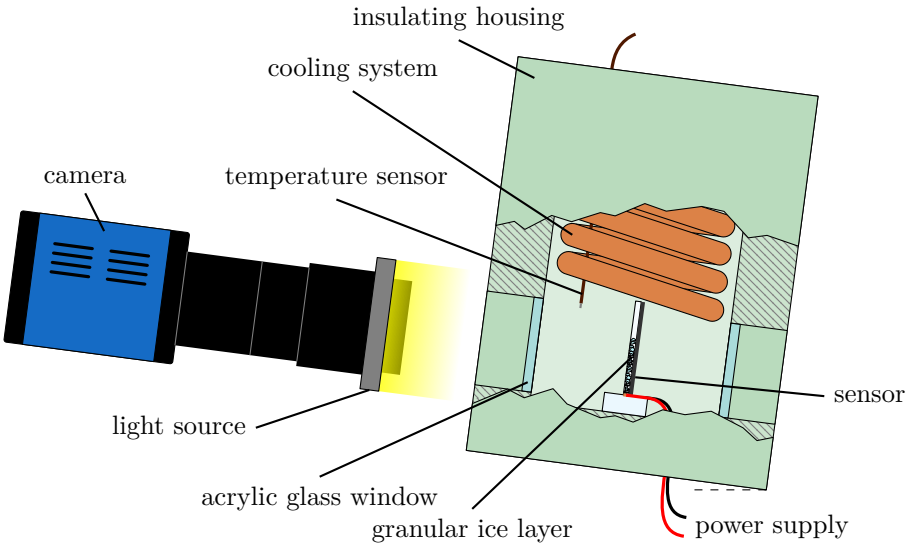

Figure 4.9: Observation system and temperature controlled housing containing the setup depicted in Figure 4.10.

and consists of the sensor described above, a heating film to melt the ice layer and a camera to observe the process. With the exception of the camera, all of these parts are placed in a temperature controlled environment. In the following, first, the housing and camera system are described and second the setup inside the temperature controlled environment is illustrated.

Housing and observation system

A cold environment allows conducting the experiments under controlled ambient conditions. A camera records the melting and imbibition process. The experimental setup is shown in Figure 4.9.

The ice layer and sensor installation are placed in an insulating housing with transparent windows and a copper tube coil through which a coolant is pumped. The temperature inside the housing is controlled to $-0.5\,°C$, which prevents inadvertent melting and ensures a negligibly small Stefan number. Due to the small Stefan number, only a negligible volume of liquid water refreezes when transported through the ice layer. Hence, the mass of ice that melts corresponds to the mass of liquid water contained in the granular ice layer. A camera, which is synchronized with the capacitive sensor, records the melting process. The camera is positioned outside of the insulating housing and captures the experiment through an acrylic glass window. A ring light surrounding the camera lens provides lighting. Polarizing filters reduce reflections from the hydrophobic films holding the ice layer. Tracking the top edge of the melting granular ice layer enables the evaluation of the volume

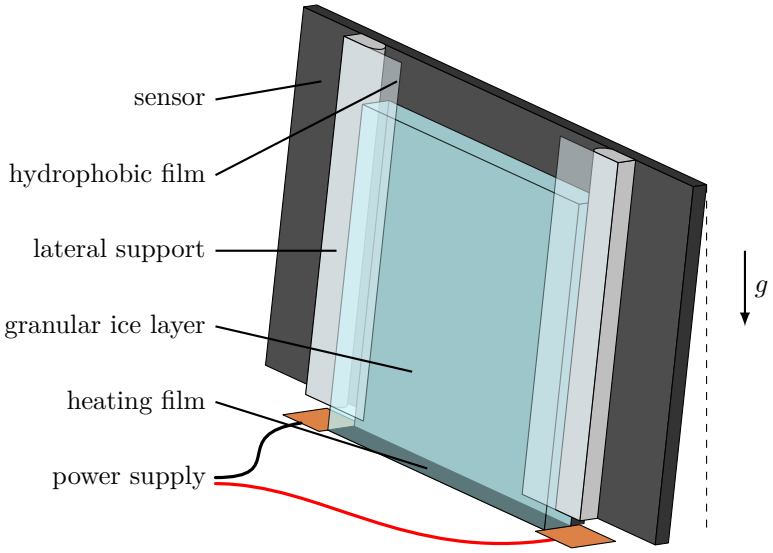

Figure 4.10: Positioning of the ice layer in front of the sensor and on the heating film.

of melted ice, from which the total liquid volume distributed in the ice layer can be calculated for each video frame. Knowing the liquid volume sets the basis for the sensor calibration described in subsection 4.1.3.

Ice layer melting setup

The produced granular ice layer is placed at the core of the experimental setup, which is illustrated in Figure 4.10. The ice layer is positioned upright in front of the sensor and held in position by a lateral support made of polyamide and hydrophobic FEP (fluorinated ethylene propylene) films. The latter ensures that the ice layer remains in contact with the sensor. Additionally, the entire setup is inclined by an angle of 10°. A heating film, supporting the ice layer from below, is utilized to melt it during the experimental run. The heating film is connected to a laboratory power supply to provide a constant heating power.

When the power supply is switched on, the bottom face of the granular ice layer melts and the generated liquid water is imbibed into the medium. Subsequently, the ice layer slides down and thus stays in contact with the heating film and the sensor throughout the experimental run. This provides a continuous heating, which is supplied to the ice layer and results in a constant melting rate.

As described in subsection 4.1.2, the distribution of liquid water in the direction perpendicular to the sensor plane must be approximately uniform. This condition can be considered fulfilled due to the small thickness of the ice layer of 3.1 mm in relation to the height of the ice layer of 30 mm and taking into account the spacing of the sensor electrode centers of 2.2 mm. Furthermore, the experiment is essentially

one-dimensional, since melting occurs at the entire bottom face. Moreover, the measured capacitance can be considered an average over the entire length of each electrode of 28 mm.

4.2 Observed phenomena

The irregular morphology and random packing of ice crystals in the granular ice layer lead to a diverse range of phenomena observed during the imbibition process. These are investigated in a parameter study involving various porosities, grain sizes, and melting rates.

Ice layer porosities of 0.3, 0.4 and 0.5 are studied. The median ice crystal grain sizes of the sieved crystals are 240 µm, 583 µm, 647 µm and 867 µm. The granular layers resemble compressed snow layers and it is expected that the porosity is in the range of natural ice accretions. By adjusting the heating power used to melt the granular ice layer, the volume flux of meltwater can be controlled. The volume flux specifies the liquid flow rate per cross-sectional area. The investigated range of volume fluxes extends from $5\,\mu m\,s^{-1}$ to $30\,\mu m\,s^{-1}$.

An exemplary image of an ice layer which is partially wetted by meltwater is depicted in Figure 4.11a. Due to the similar refractive indices of liquid water and ice, the wetted regions in the ice layer appear darker than the dry region, which allows tracking the wetting front, qualitatively highlighted by the dashed red line. On a macroscopic level, the imbibition process in the present experiments can be considered as one-dimensional, since the wetting front is approximately horizontal. Therefore, each video frame can be summarized by a single column where the grayscale values represent averages along horizontal lines. As a result, the temporal evolution of one experiment can be illustrated in a single image as shown in Figure 4.11b. In this figure, the grayscale columns for all time steps are concatenated along the horizontal axis. The wetted part of the granular ice layer is represented by the propagating darker region, separated from the dry medium by the fitted dashed red line. The top edge of the melting ice sample can be identified by the boundary to the black background.

Due to a negligibly small Stefan number, the ice begins to melt as soon as the bottom of the sample is heated and the granular layer slides down and thus stays in contact with the heating film. The linear decrease of the top edge of the ice layer corresponds do a constant volume flux of meltwater. The generated meltwater is driven into the porous layer by capillary forces. The wetting front appears to propagate into the granular ice layer at a constant velocity. However, this observation is limited to the time and length scales observed in the present experiments. In an alternative scenario where the porous medium is exposed to a liquid pool, inertial forces affect the imbibition process on a short time scale after contact occurs [56]. However, this is not observed in the present experiments, which is partially attributed to the time and length scales investigated, but foremost to

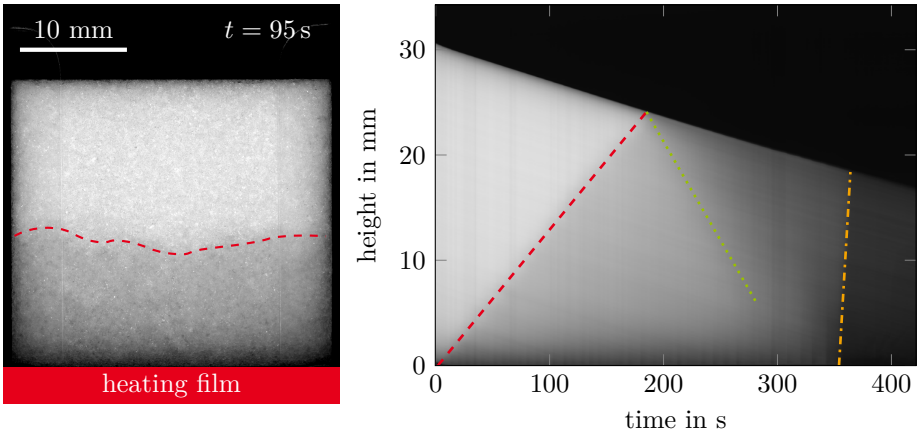

(a) Exemplary image of a partially wetted granular ice layer **(b)** Two-dimensional representation of an experimental run

Figure 4.11: Exemplary image of a partially wetted granular ice layer (a) and the temporal evolution of the experiment, where each column corresponds to a video frame (b). The dashed red line qualitatively highlights the wetting front. The green and orange lines separate regions of increased saturation. The ice layer has a porosity of 0.4, the median grain size is 240 µm and melting results in a volume flux of $19\,\mu\mathrm{m\,s^{-1}}$.

the different boundary conditions. The supply of liquid water is limited by the rate by which the ice layer is melted. Therefore, only a finite volume flux is provided, which restricts the imbibition. Furthermore, the complex pore structure results in a large tortuosity, i.e., the path that the liquid has to travel between two points is significantly greater than the length of a straight line connecting those points. Therefore, any effects due to inertia are expected to decay on a short distance.

The linear trend in the wetting front position suggests that gravity plays a minor role in the water distribution. This is in contrast to previous studies of water transport in snow, which focus on larger scales up to several meters, where gravity has a significant influence [65, 37, 163].

Exemplary images of the propagating wetting front for two ice layers with different porosity are depicted in Figure 4.12. The dashed line qualitatively indicates the contour of the wetting front. These profiles reveal the flow pattern in the granular medium. The present experiments indicate that the observed patterns are correlated with the porosity of the granular layer. At a low porosity of 0.3, the contour appears smooth and the wetting velocity remains uniform across the width of the sample, as shown in Figure 4.12a. In contrast, a high porosity of 0.5 leads to the emergence of a more complex structure, resulting in a larger spatial variability of the propagating liquid front, which can be recognized in Figure 4.12b. The flowing liquid exhibits an erratic path, characterized by sudden changes in direction, abrupt halts and the spontaneous emergence of new structures. The observed structures only appear

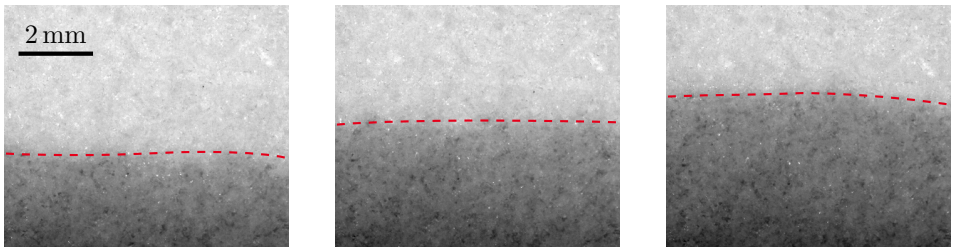

(a) Granular ice layer with a porosity of 0.3

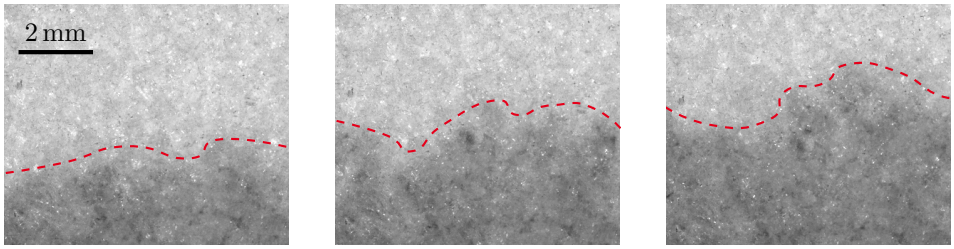

(b) Granular ice layer with a porosity of 0.5

Figure 4.12: Characteristic wetting fronts during imbibition at different porosities. The dashed lines highlight the approximate contour of the wetting front. The three images in each depicted experiment correspond to time steps of 10 s. The granular layers are composed of ice crystals with a median grain size of 583 µm and imbibe a volume flux of 16 µm s^{-1}.

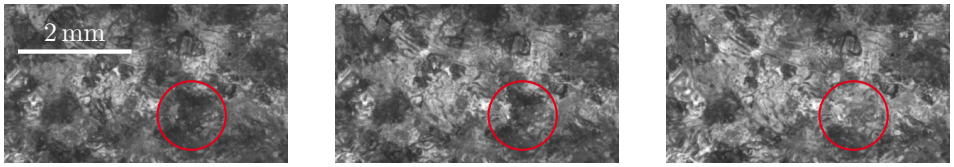

Figure 4.13: Flooding of larger pores after the wetting front reached the end of the granular ice layer. To better visualize the remaining pores, the melting granular ice layer in this experiment is illuminated by a light source at the back of the specimen. Dark regions correspond to pores, some of which are gradually filled with liquid. The depicted images are acquired at time steps of 5 s.

on a small scale and the large scale flow can therefore be assigned to the matrix flow regime, which is in contrast to preferential flow, as described by Schneebeli [162] and Waldner et al. [191]. Waldner et al. [191] attributed the initiation of preferential flow, which is characterized by flow fingers propagating through the granular medium, to microstructural defects in the snow. The emergence of more complex structures in the wetting front can be interpreted as a pre-stage of flow fingers in preferential flow.

A similar effect is observed regarding the grain size of the crystals composing the granular ice layer. For the smallest investigated ice crystal grains with a median size of 240 µm, the wetting front is significantly smoother than for the largest investigated grain size with a median size of 867 µm. However, within the studied parameter range, the effect of grain size is less pronounced than that of porosity. An influence of grain size on the emergence of preferential flow patterns was previously described by Katsushima et al. [91].

Once the wetting front reaches the top of the ice layer, pore saturation continues to increase as the top edge of the ice layer enforces a vanishing flux. Therefore, water flowing towards the top edge is accumulated and saturation appears to increase from top to bottom. This is highlighted by the dotted green line in Figure 4.11b.

Finally, as indicated by the dashed dotted orange line in Figure 4.11b, saturation continues to increase close to saturation. Larger pores that were not previously flooded are infiltrated, leading to higher saturation. An exemplary series of images captured to highlight this phenomenon is shown in Figure 4.13. In the experiment shown in this figure, the ice layer was illuminated by backlighting to better highlight the residual air. Therefore, pores with low saturation appear dark while pores with high saturation appear bright in these images. The circle in the images marks one of the pores that are being infiltrated in the sequence.

Eventually, meltwater is no longer imbibed, suggesting that pores either are saturated with liquid or contain trapped air bubbles. Visual observation indicates that the wet ice layer contains numerous trapped air bubbles, suggesting that snap-off occurs as a result of the liquid flow along the corners.

4.3 Wetting front velocity

During primary imbibition, when water first wets the initially dry granular ice layer, the wetting front propagates at a constant rate, as was shown in Figure 4.11b. The velocity of the wetting front relative to the ice specimen is shown in Figure 4.14 as a function of the volume flux supplied by melting of the ice layer. The different markers indicate individual measurements with ice layers of different porosity. These measurements indicate that the wetting front velocity is primarily determined by the influx of liquid. No significant influence of porosity can be identified. Similarly, the grain size of the ice crystals – which is not shown in the figure – does not have a significant influence on the wetting front velocity.

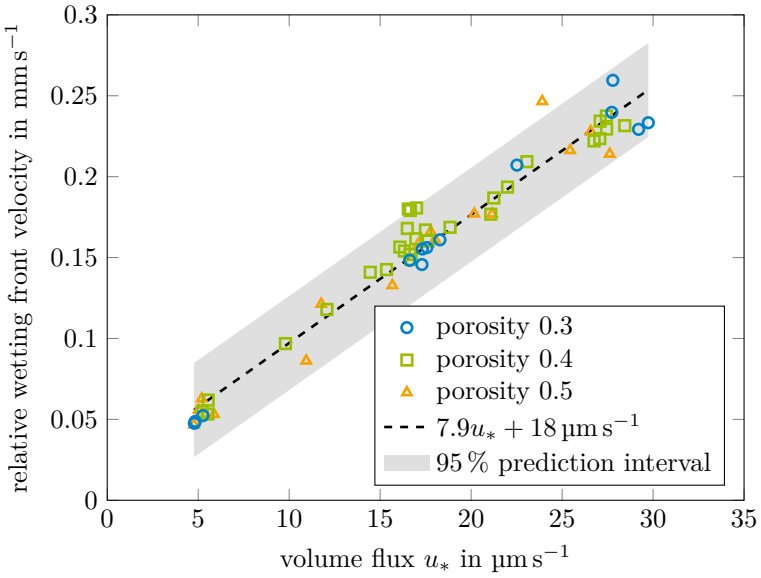

Figure 4.14: Relative wetting front velocity as a function of volume flux introduced at the heating film.

One would have expected the capillary pressure to increase with decreasing porosity while keeping the grain size constant, which would lead to a higher wetting front velocity. However, this trend is not observed in the experiments. A possible explanation for this phenomenon is that the pores are not saturated and water only flows along the network of corners and grooves of the porous medium. Hence, the capillary pressure is determined by the geometry of this network and not by the pore volume. The network of surface groves in turn, is governed by the morphology of the ice crystals. Since the ice crystal morphology is similar for the different classes of ice crystal grain size, neither porosity nor grain size has a significant influence on the wetting front velocity.

4.4 Liquid distribution

The developed capacitive sensor enables the measurement of the liquid distribution in the melting granular ice layer. The results of an exemplary experimental run are shown in Figure 4.15a in form of the saturation at each sensor strip as a function of time. The horizontal axis specifies time, the vertical axis specifies the vertical position and the color indicates the corresponding saturation. Since the sensor is highly sensitive to direct contact with water, there exists an upper limit for the measurable saturation, which in turn imposes a restriction on the duration that is evaluated. The characteristics of the depicted experiment can be considered

as representative for all experiments in the investigated parameter space. Since the experiment starts with a dry ice layer, the saturation initially equals zero. As the ice layer melts, the saturation at the bottommost sensor strip increases as water is imbibed by the ice layer. Successively, the saturation at one sensor strip after another increases. A linear fit of the wetting front obtained from the video is indicated by the dashed line. Due to the spacing of 2.2 mm between the sensor strips, instabilities in the wetting front as they are illustrated in Figure 4.12 are not resolved by the sensor.

The saturation profile in the granular ice layer is shown in Figure 4.15b. The illustrated data corresponds to the data shown in Figure 4.15a. However, the representation in Figure 4.15b provides a better comprehension of the liquid distribution. The increased saturation measured at a height of 13.1 mm and 15.3 mm from 120 s on, reflects a measurement error occurring at these sensor strips at increasing saturation in several experimental runs. The repeatability of the experimental runs is limited and variations of up to 20 % of the indicated saturation occur. The variations are larger at the first sensor strip right above the heating film, since in some cases a minor air gap developed when the granular ice layer does not perfectly slide downwards. Nonetheless, the measured trends in saturation are consistent in repeated runs. To account for the variability of the acquired data, the figures shown in this section depict the mean values obtained from a minimum of three experimental runs.

The saturation in the wetted region of the granular ice layer decreases with height. It can be recognized that the pores are not saturated at any time during the experiment before the wetting front reaches the top edge of the specimen. However, this observation is limited to the investigated granular ice layers with an initial height of 30 mm. It can be expected that ice layers of significantly larger height, such that the effect of gravity has to be considered, will eventually reach saturation at the bottom of the specimen. Similarly, an increased saturation can be expected at higher volume fluxes, beyond the range investigated in this study.

While the liquid profile in the vicinity of the wetting front approaches zero, it does not exhibit a sharp boundary, but appears to decay gradually. This phenomenon is most pronounced shortly after the start of an experiment. With progressing time, the liquid profile shows an approximately linear decrease with increasing height in the wetted region.

Two approaches can explain the liquid profile in the melting granular ice layer. First, the porous medium can be modeled as a bundle of capillaries, as proposed for example by Washburn [194] and Coléou et al. [35]. Due to the complex pore geometry, the capillaries have to be considered as having different diameters. The wetting liquid will then preferentially infiltrate the finer capillaries, resulting in a higher velocity in comparison to the flow in the larger capillaries. Hence, the liquid levels will spread out during imbibition, which yields a decrease in saturation with increasing height. Second, due to the complicated network of pores and surface

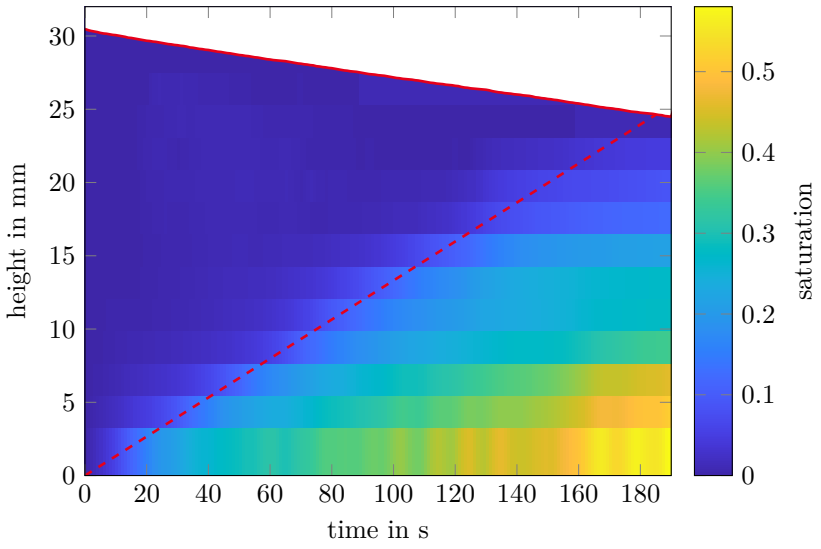

(a) Colorized saturation with superimposed wetting front position obtained from the video

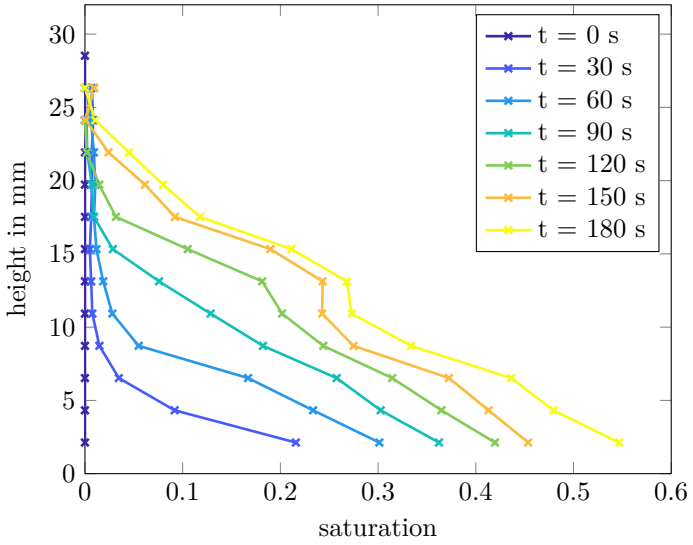

(b) Saturation profiles at different time instants

Figure 4.15: Saturation in the melting granular ice layer as a function of space and time. The granular ice layer in the depicted experiment has a porosity of 0.4, is composed of ice crystals with a median grain size of 647 µm and melting results in a volume flux of 17 µm s^{-1} at the bottom of the specimen.

grooves, the wetting liquid can follow different flow paths, which are dictated by the geometry of the pores. This yields a stochastic propagation of water in the granular ice layer, which results in a spread out liquid profile.

The conducted parameter study allows to investigate the different influences of porosity, grain size and volume flux on the water distribution within the ice layer. These effects are discussed in the following.

4.4.1 Influence of ice layer properties

In this subsection, the influences of the properties of the granular ice layer on the liquid distribution are described, focusing first on the effect of porosity and second on the effect of ice crystal grain size.

The saturation in melting granular ice layers with porosities of 0.3, 0.4 and 0.5 is depicted in Figure 4.16. The depicted experimental runs are conducted with ice layers composed of ice crystals with a median grain size of 583 µm and are subjected to a volume flux of $17\,\mu m\,s^{-1}$.

It can be recognized that an increasing porosity yields a decrease in saturation. This is attributed to the increased pore volume available for the liquid. At an increased porosity, the same volume of meltwater occupies a smaller fraction of the pore volume, which results in a decrease in saturation. Interestingly, this change in saturation does not significantly influence the propagation of the wetting front, as it was demonstrated in Figure 4.14.

The influence of the ice crystal grain size composing the granular ice layer is depicted in Figure 4.17. In this figure, the saturation profiles of granular layers with median grain sizes ranging from 240 µm to 867 µm are presented. The illustrated experiments are conducted at a porosity of 0.4 and a volume flux of $17\,\mu m\,s^{-1}$. For clarity, the saturation profiles are only shown for a single time instant of 60 s after the start of the experiment. The data should be interpreted with caution due to the noticeable scatter. However, the same trend is reflected in the data corresponding to different points in time. The depicted data suggest that the decrease in saturation is less steep for larger ice crystals. This is presumably attributed to an increased permeability with larger grain sizes, which is also reflected in the Carman-Kozeny model for the permeability of a granular medium [41].

4.4.2 Influence of volume flux

Furthermore, it is of interest how the volume flux of water supplied to a porous ice layer affects its saturation profile. Literature on imbibition into dense ice layers is scarce, however, Coléou et al. [35] measured the liquid distribution in snow columns brought in contact with a liquid pool by optically analyzing sections of

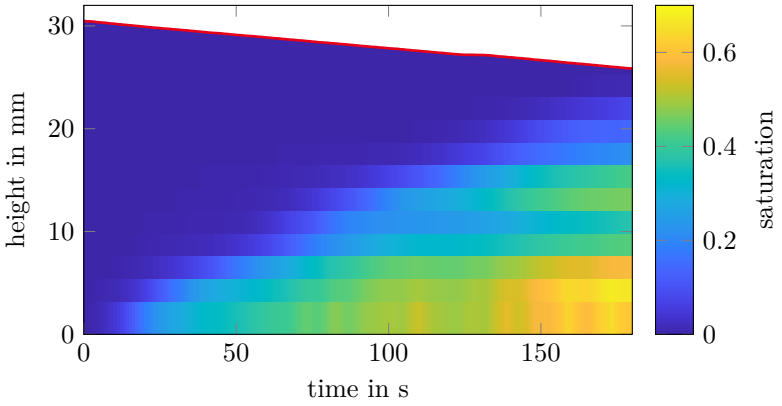

(a) Melting ice layer with a porosity of 0.3

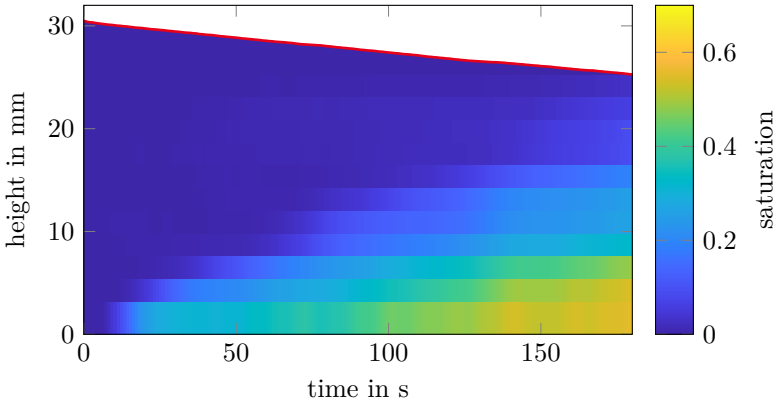

(b) Melting ice layer with a porosity of 0.4

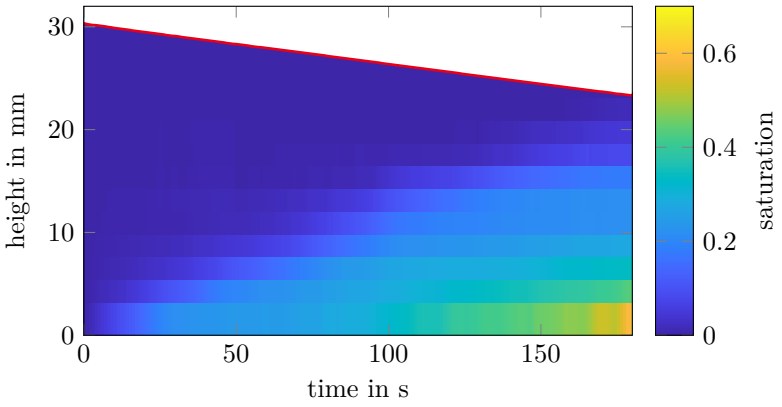

(c) Melting ice layer with a porosity of 0.5

Figure 4.16: Influence of porosity on the saturation of the pores in an ice layer composed of ice crystals with a median diameter of 583 µm. The melting induced volume flux at the bottom of the ice layer is 17 µm s^{-1}.

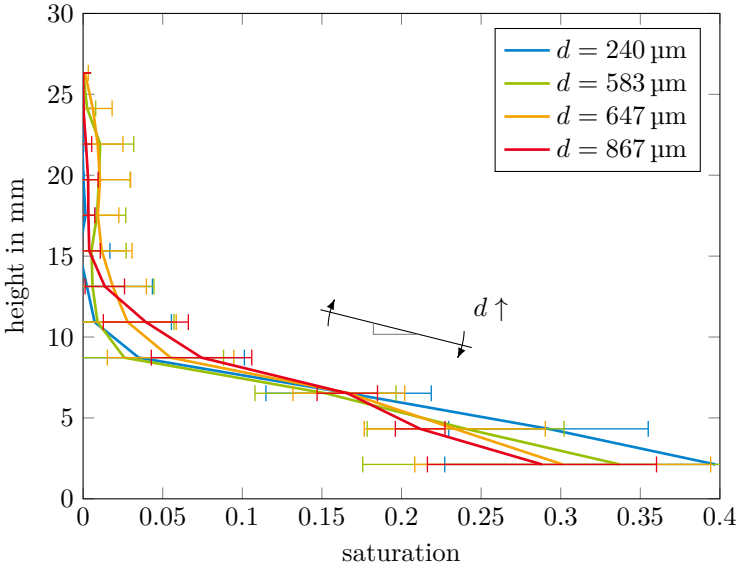

Figure 4.17: Influence of grain size d of the ice crystals composing the granular ice layer on the saturation profile at the same time instant. The error bars represent the 95 % confidence bounds. The trends indicate a steeper decrease in saturation with decreasing grain size. For clarity, the saturation profiles are only shown at one single time instant of $t = 60\,s$. The same trend is reflected in the data corresponding to different times. The specimen have a porosity of 0.4 and the influx of water is $17\,\mu m\,s^{-1}$.

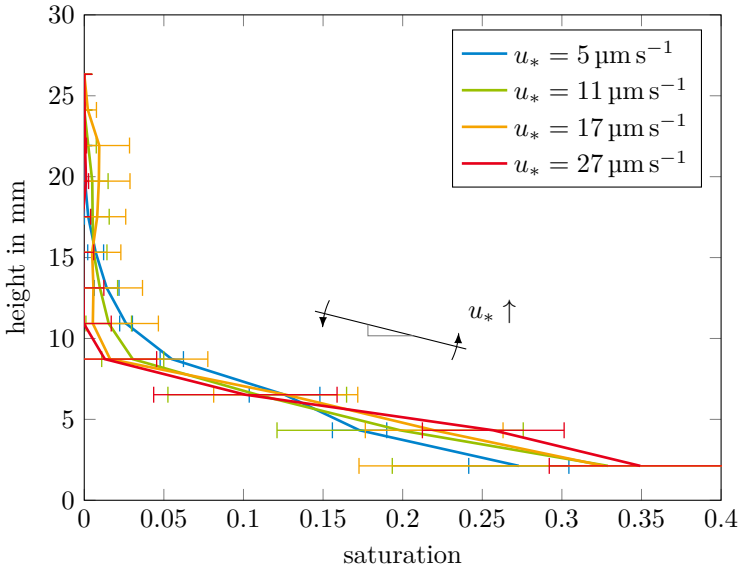

Figure 4.18: Influence of volume flux supplied to the granular ice layer illustrated at a time instant with identical liquid water content. The error bars represent the 95 % confidence bounds. The trends indicate a steeper decrease in saturation with increasing volume flux. For clarity, only one set of saturation profiles is shown, which corresponds to a dimensionless time $\tau = 0.029$, as defined by Equation 4.6. The same trend is reflected in the data corresponding to different times. The specimen have a porosity of 0.4 and a median grain size of 583 µm.

the snow. In their experiments, the volume flux is high, since the liquid pool provides an unrestricted water supply. They specify the distance over which the pores transition from fully saturated to dry as approximately 2 cm. While they did not provide the porosity of the examined snow samples, the described process of gathering the sample suggests that the porosity is significantly higher than those investigated in the present work. In contrast to the observation of Coléou et al., in the present work, the granular ice layers at the highest investigated porosity of 0.5 are significantly below saturation in the entire sample having a vertical dimension of approximately 23 mm when the wetting front reaches the top edge. The important distinction between the present experiments and the study of Coléou et al. is that in the present study the liquid supply is limited by the melting rate. This qualitative difference suggests an influence of the volume flux supplied to the ice layer, affecting the saturation gradient inside the porous medium. The volume flux is varied systematically between $5\,\mu m\,s^{-1}$ and $27\,\mu m\,s^{-1}$ in order to study its effect on the water distribution.

In the following, the influence of volume flux on the saturation profile is investigated. In order to compare the saturation profiles at different input fluxes, the time has to be scaled such that the same total liquid volume is distributed in the

granular layer. Therefore, the dimensionless time

$$\tau = t\frac{u_*}{h} \tag{4.6}$$

is introduced. Here, t represents time, u_* the volume flux and h the initial ice layer height of 30 mm. The purpose of this scaling is solely to enable the comparison of the liquid profiles at different input fluxes. This comparison is shown in Figure 4.18 for different volume fluxes resulting from a change in heating power introduced by the heating film. The depicted experiments correspond to granular ice layers with a porosity of 0.4 and a median grain size of 583 µm. The saturation profile is shown for four volume fluxes of $5\,\mu m\,s^{-1}$, $11\,\mu m\,s^{-1}$, $17\,\mu m\,s^{-1}$ and $27\,\mu m\,s^{-1}$ at an exemplary dimensionless time $\tau = 0.029$. While the total volume of liquid in the granular ice layers is the same, the distribution of liquid differs. The decrease in saturation with increasing height is steeper for higher volume fluxes. For clarity, only a single set of liquid distributions is shown. However, the same trend is reflected in the profiles at different time instants and volume fluxes. This confirms the dependence of the water distribution on the supplied volume flux. The saturation profile is not only determined by the available liquid volume, but also by time. When granular ice or snow layers are in contact with a water pool, the pores are saturated shortly behind the wetting front, as observed by Coléou et al. A limited water supply, as investigated in the present experiments, results in a significantly extended region below saturation. In this configuration, the influx and the time for liquid to distribute affect the saturation profile. A further regime is observed in the experiments when the heating is abruptly switched off. In this case, the wetting front decelerates significantly. However, wetting does not stop and water continues to spread in the ice layer. These results are qualitatively consistent with the expected trends predicted by Richards' equation, which describes diffusion-like water transport [156].

4.5 Summary

A novel capacitive sensor has been developed, which is capable of resolving the liquid distribution in a porous medium. The sensor provides a time and space resolved measurement of the liquid content and has been applied to characterize the water transport in a melting granular ice layer. Additionally, the melting process and the wetting front during imbibition of the meltwater have been recorded and analyzed.

By melting the granular layer, a constant volume flux was supplied and imbibed by the porous medium. The contour of the wetting front was found to be affected by both the porosity and grain size. The porosity was varied from 0.3 to 0.5 and the median grain size ranged from 240 µm to 867 µm. An increase in these properties results in a rougher wetting front. The liquid was observed to flow in an erratic

path, characterized by local abrupt changes in direction, sudden halts and the formation of new structures.

The constant volume flux imbibed by the granular ice layer resulted in a constant wetting front velocity. Within the investigated parameter range, the wetting front velocity appeared to increase linearly with an increasing volume flux. No significant influence of porosity or grain size have been identified.

Once the wetting front reaches the end of the ice layer, water accumulates and saturation further increases. Towards the end of the experimental run, previously unfilled larger pores are infiltrated. Due to corner flow along the network of surface grooves, air bubbles get trapped in the wet granular medium.

The sensor reveals that the saturation decreases with increasing distance to the heating film. In the investigated parameter range, the pores are not saturated with liquid prior to the wetting front reaching the top edge of the granular ice layer. However, different parameters have been found to influence the saturation profile. Saturation increases with decreasing porosity, since the same liquid volume is distributed in a smaller pore volume. The saturation profiles of granular ice layers, subjected to different volume fluxes but measured at the same total liquid content, demonstrate the influence of volume flux. An increase in volume flux yields a sharper decline in saturation. This finding aligns with the research conducted by Coléou et al. [35], who observed a shorter distance between saturated and dry pores compared to the present experiments, when their sample was brought into contact with a liquid pool, which is expected to yield a larger volume flux. Similarly, the influence of the grain size of the ice crystals composing the granular layer has been investigated. An increase in grain size was found to result in a shallower decrease in saturation, which is suspected to be caused by an increasing permeability of the ice layer pore network.

The presented findings offer valuable insights into the imbibition process of meltwater into granular ice layers and emphasize the influences of porosity, grain size and volume flux. These results can be utilized to refine model parameters in numerical tools, thereby improving the accuracy of the predicted liquid distribution within granular ice layers and enable accounting for the properties of the porous medium. Consequently, these results can contribute to a better comprehension of various phenomena, including, for instance, the icing of structures, the forecasting of avalanches and the prediction of the evolution of glaciers.

5 Liquid distribution in ice accretions

Liquid water plays a crucial role in the formation of ice accretions due to ice crystal icing, whether it is transported in the airflow or generated by the melting of ice on a heated substrate. Previous studies have examined ice accretion due to partially melted particles and several instruments exist that are designed specifically to measure the melt ratio in the flow [143, 113, 175]. However, a lack of instrumentation currently exists to quantify the liquid water in an accretion generated from melting ice on a heated substrate. Thus, information gathered on the physical phenomena associated with this process is limited, particularly for wet bulb temperatures below zero, where the transport and distribution of liquid water within the ice layer are key drivers of the accretion process. This chapter aims to address this gap by advancing the instrumentation of icing wind tunnels and enhancing the understanding of ice crystal icing on heated substrates. Part of this chapter has been submitted to the International Journal of Heat and Mass Transfer.

For this study, a novel methodology based on capacitive measurement is proposed to quantify the distribution of liquid water in an ice accretion. The developed instrument is employed in an icing wind tunnel where experiments are conducted to measure the thickness of the accreted ice and the liquid distribution. The thickness and three-dimensional geometry of the ice accretion are captured by shadowgraphy and stereo vision. The data from the capacitive sensor and the accretion geometry are combined to quantify the relationship between sticking efficiency and liquid fraction at the accretion front. A parameter study has been conducted to determine the effects of wet bulb temperature of the airflow, heat flux at the substrate and ice water content on accretion thickness, liquid distribution and sticking efficiency.

The experiments were performed in the Braunschweig icing wind tunnel in cooperation with Yasir A. Malik. This wind tunnel is capable of simulating various conditions for ice crystal icing. In this chapter, first the experimental methods, which include the newly developed capacitive sensor, are presented in section 5.1. Second, the observed shape of the accretion is described in section 5.2. Subsequently, the evolution of the ice thickness is discussed in section 5.3, followed by the analysis of the distribution of liquid water in section 5.4. Finally, in section 5.5, the relation between sticking efficiency and liquid volume fraction at the accretion front is presented.

5.1 Experimental methods

The methods presented in chapter 4 aim at emulating the melting of an ice or snow accretion, both of which represent granular ice layers. While these experiments

enable a detailed investigation under well controlled conditions, some aspects of real ice accretions cannot be recreated. Therefore, in order to closer resemble realistic ice accumulations as they occur in the framework of aircraft icing, experiments to quantify the liquid fraction of ice accretions grown in an icing wind tunnel are conducted. These experiments are carried out in the icing wind tunnel of Technische Universität Braunschweig. In this section, first, an overview of the experimental facility and its capabilities are presented and second, the sensor developed for this study and the experimental setup in which it is employed are described.

5.1.1 Experimental facility

In the following, an overview of the Braunschweig icing wind tunnel is presented. Additional information on the wind tunnel and its capabilities can be found in the work of Bansmer et al. [11]. The experimental facility can be divided into two subsystems: The temperature controlled wind tunnel and the ice crystal generation and conveyance system.

Icing wind tunnel

A cross-section of the icing wind tunnel is illustrated in Figure 5.1. The ice crystals are supplied via a pipe from a cold chamber located above the wind tunnel. The test section has a cross-section of $0.5\,\mathrm{m} \times 0.5\,\mathrm{m}$. The wind tunnel is cooled by a refrigeration unit connected to a heat exchanger in the wind tunnel. The relative humidity cannot be directly regulated. However, by cooling the air in the closed return wind tunnel, the air becomes saturated with water vapor, resulting in a relative humidity of 100 %. The maximum air speed reached in the test section is $40\,\mathrm{m\,s^{-1}}$. The Braunschweig wind tunnel does not offer the possibility to simulate altitude conditions. Hence, the static pressure during the experimental runs is equal to the ambient pressure.

To date, the wind tunnel has not been calibrated with respect to the melt ratio at positive wet bulb temperatures.

Ice crystal generation and conveyance system

As indicated in Figure 5.1, the ice crystals used for the experiments are supplied to the air flow with a pipe from a cold chamber above the wind tunnel. The ice crystals are generated in a cloud chamber, which is illustrated in Figure 5.2 and located in the cold chamber. The cloud chamber works by injecting atomized water in a balloon, in which the nucleation of ice crystals is triggered with pulses of pressurized air. The generated ice crystals are collected in a chest freezer below the balloon.

The produced ice crystals are loaded into a dosing system, which disperses the crystals on a sieving machine. The sieved ice crystals are then transported by an

airflow from below the sieve through a pipe into the wind tunnel.

During the commissioning of the Braunschweig icing wind tunnel the ice crystals in the test section have been characterized. A comparison of natural ice crystals in different cloud regions with the ice crystals in the wind tunnel is shown in Figure 5.3. The ice crystals exhibit a similar morphology and some particles resemble aggregates, which are typical for snow. Further details on the comparison, which include the mass–size distribution, can be found in the work of Bansmer et al. [11].

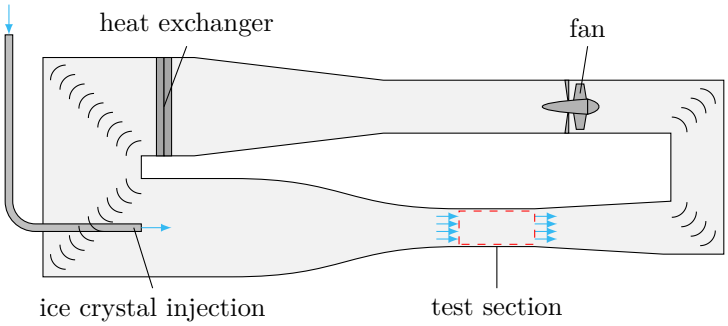

Figure 5.1: Overview of the Braunschweig icing wind tunnel. The cold chamber in which the ice crystals are produced is located above the wind tunnel.

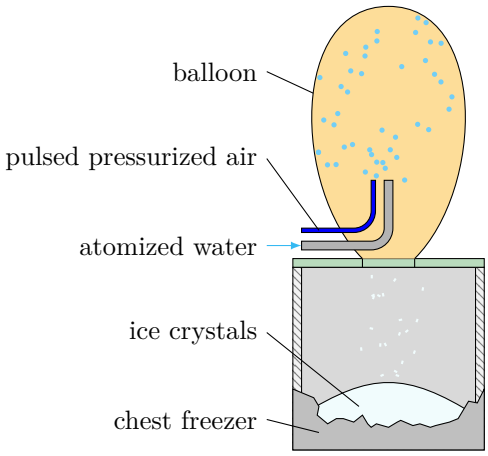

Figure 5.2: Cloud chamber for ice crystal generation inside a cold chamber located above the icing wind tunnel. Nucleation of the freezing of cold atomized water is initiated by pulses of pressurized air.

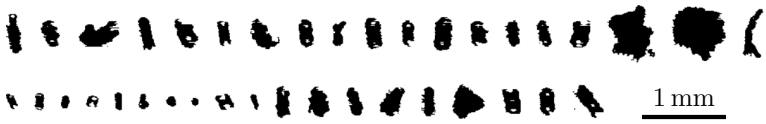

(a) Convective cloud region, 80 µm median mass diameter, $3\,\mathrm{g\,m^{-3}}$ ice water content and −10 °C air temperature

(b) Stratiform cloud region, 150 µm median mass diameter, $1.2\,\mathrm{g\,m^{-3}}$ ice water content and −10 °C air temperature

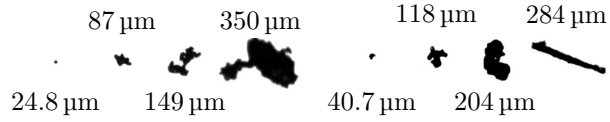

(c) High speed imaging of particles in the wind tunnel at 0 °C and −5 °C and their mass diameters

(d) Particles in the wind tunnel, 79 µm median mass diameter, $3.2\,\mathrm{g\,m^{-3}}$ ice water content and −15 °C air temperature

Figure 5.3: Natural ice crystals in different cloud regions recorded during the Darwin Campaign, (a) and (b), and ice crystals in the Braunschweig icing wind tunnel, (c) and (d), for comparison. (Adapted from Bansmer et al. [11], published under CC BY 4.0)

5.1.2 Measurement of the liquid distribution

In the following, the experimental methodology for obtaining the distribution of liquid water in an ice accretion is described. A capacitive measurement technique is developed and the designed sensors are placed in the test section of the wind tunnel. In addition to the measurements with these sensors, the ice accretion process is recorded with multiple cameras, which enables a reconstruction of the three-dimensional geometry of the ice layer.

First, the capacitive measurement technique developed for this study is presented and second, the test article and setup of the measurement equipment are described.

Capacitive sensor design

Two capacitive sensors have been developed to quantify the liquid fraction in the ice accretion growing on the test article in the wind tunnel. While the measurement principle is identical to that of the sensor described in subsection 4.1.2, the aim and thus the requirements for this sensor are different. The previously described sensor resolves the spatial distribution of liquid water in a granular ice layer by measuring the liquid fraction at different locations along the direction of liquid water transport. However, this cannot be applied in wind tunnel experiments without affecting the accretion process.

Currie and Fuleki [44] utilized a capacitive sensor to quantify the liquid volume fraction of an ice accretion grown at positive wet bulb temperatures on an approximately adiabatic test article. Since for fringe fields, the magnitude of the electric field decreases with increasing distance to the electrodes, they had to assume a uniform distribution of liquid water in order to interpret the sensor readings. While this might be valid for an adiabatic substrate, a heated substrate introduces a nonuniform distribution of liquid water. Therefore, multiple sensors are required to obtain information on the profile of liquid fraction. The two sensors described in this section aim at quantifying the liquid volume fraction in two different regions in the ice layer. One sensor is focused on the region close to the substrate, while the other sensor covers a larger distance to the substrate. Combining the data from the two sensors enables the estimation of the water distribution.

This difference in comparison to the previous sensor utilized in chapter 4 is reflected in the requirements for the current sensor. Since no spatial resolution is obtained from different electrode pairs, only a single electrode pair is needed. Furthermore, no minimization of the electrode width and gap width is required, which previously was demanded to improve the spatial resolution.

In order to allow for a wider measurement range, an LCR meter (Rohde & Schwarz HM8118) is used for the acquisition of the capacitances. Due to the wide measurement range, the sensor layout does not have to be optimized with respect to the absolute values of the occurring capacitances. The uncertainty in the measured values is given as a relative uncertainty. Therefore, the sensor design is focused on

the relative change in capacitance due to the presence of liquid water in front of the sensor.

The utilized LCR meter offers only one single channel for measuring capacitances. Since the measurement at a single electrode pair does not provide information about the distribution of liquid water, the experiment needs to be repeated with the second sensor. While as a matter of principle it would be possible to incorporate both sensor layouts in a single test article, this would introduce further difficulties. The two pairs of electrodes would have to be distributed on the test article such that they do not interfere with each other. Thus, the two sensors would have to be located in separate regions on the substrate. Nonuniformities in the accreted ice layer, e.g., due to spatial nonuniformities in the incoming ice water content, could lead to incomparable measurements. Moreover, measuring a second capacitance would require an additional LCR meter. Hence, two sensors are designed and after measuring with one of the sensors, it is exchanged and the experiment is repeated. This procedure relies on the repeatability of the experiments, which is found to be adequate for this approach.

The electrodes of the sensors are designed as interdigitated fingers. The widths of the electrodes and the gaps between them are optimized based on a numerical parameter study. The number of fingers in this pattern is finally determined by the size of the sensor plate. To obtain information about the distribution of liquid water, different parameters are selected for the two required sensors. Following the numerical parameter study, the electrode widths and the gap widths of the first sensor are set to 2 mm each. The second sensor has electrode and gap widths of 0.5 mm each. Since the two sensors are differentiated by the range in which they are sensitive, the sensors are in the following referred to as large-scale and near-wall sensor, respectively. The layout of the two sensors is depicted in Figure 5.4.

The sensitivity decays with increasing distance to the sensor. This function is derived from the numerical simulations of the electric field and subsequently normalized such that the integral over the entire domain equals unity. This normalized sensitivity represents a weighting function $w(z)$, which specifies how the material at the corresponding distance to the substrate contributes to the capacitance. Figure 5.5 presents the normalized sensitivity for each sensor.

Since the magnitude of the electric field decreases with increasing distance to the sensor, the capacitance is mostly determined by the relative permittivity close to the substrate. For the large-scale sensor, any ice accretion beyond 5 mm will result in a change in capacitance of 1 % or less. Since this distance corresponds to the expected ice layer thickness, no significant disturbance from the surroundings is anticipated. The near-wall sensor focuses on the region close to the substrate. For this sensor, the wet ice located further than 1 mm away from the substrate only contributes to the measured capacitance by 1 %.

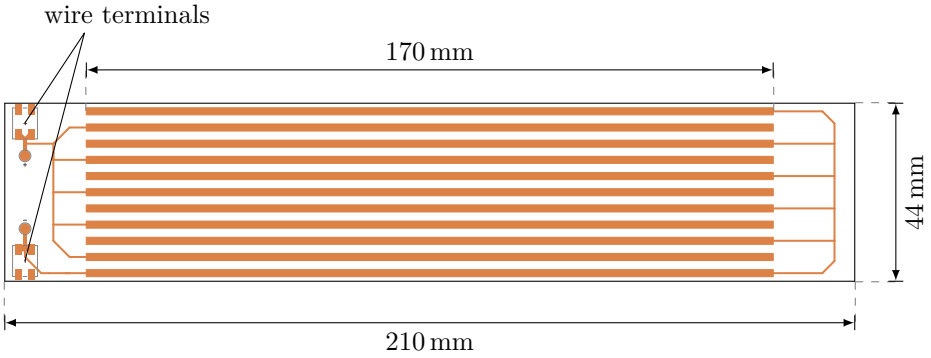

(a) Large-scale sensor with electrode widths and gap widths of 2 mm

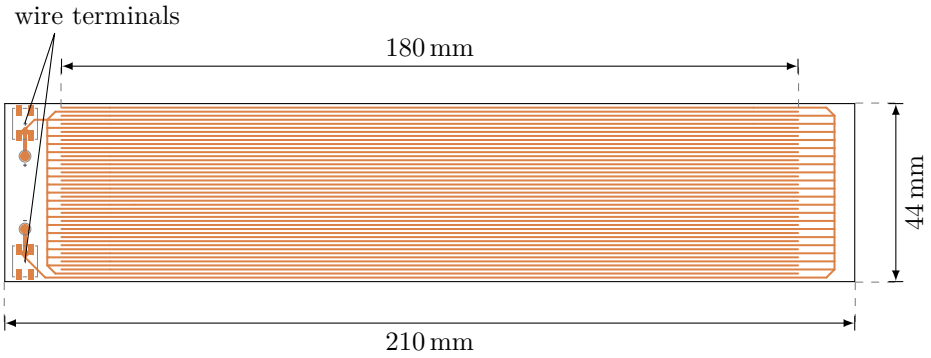

(b) Near-wall sensor with electrode widths and gap widths of 0.5 mm

Figure 5.4: Schematics of the two sensors with the wire terminals for connecting the measurement device on the left and the copper traces acting as electrodes in the center.

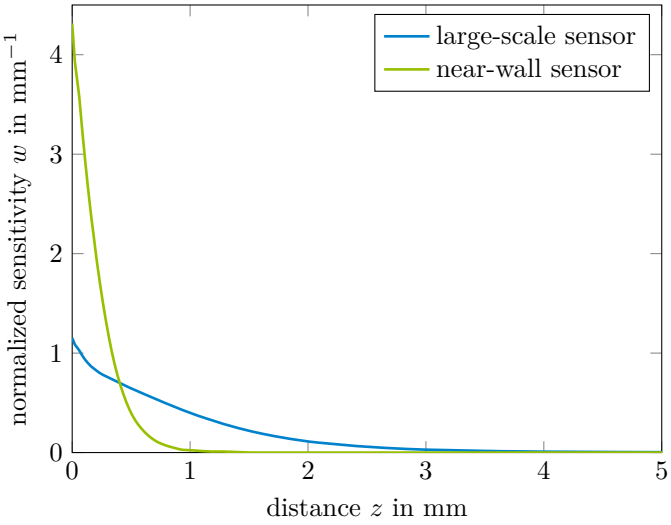

Figure 5.5: Sensor sensitivities normalized such that their integrals over the whole domain equals unity.

Procedure for obtaining the liquid distribution

Three steps are required to convert the measured capacitance values to a liquid volume fraction inside the ice accretion: First, a correlation that relates the liquid volume fraction to the dielectric properties of wet granular ice layers is required. Second, the measured capacitance values obtained by the two sensors need to be related to relative permittivity values. This requires a calibration of the sensors. Third, since the liquid water is not distributed uniformly within the ice layer, the distribution must be calculated from the readings of the two sensors.

Dielectric properties of a wet granular ice layers As outlined in the literature review on dielectric properties of wet ice layers in subsection 1.2.6, no existing equation adequately describes the relationship between the relative permittivity of a granular ice layer across the entire range, from a dry medium to a fully saturated medium. Therefore, in this work, two correlations are combined: One for the lower liquid volume fractions and another for higher liquid volume fractions.

In a comparison of different models for the effective relative permittivity of a wet granular ice layer with the measurements obtained by Currie and Fuleki [44], the model of Bruggeman showed the best agreement as it is applicable to higher liquid volume fractions than other theory-based models. Thus, for low and intermediate liquid volume fractions, the relative permittivity is calculated from the Bruggeman model fitted to the data of Currie and Fuleki in this regime. The fitted depolarization factors are $\boldsymbol{\zeta} = [0.744, 0.128, 0.128]$.

At percolation, the liquid phase forms a cluster and the effective relative permittivity is significantly larger than the value predicted by the Bruggeman model. On a macroscopic scale, the ice accretion can be considered statistically isotropic. Thus, the model of Hashin and Shtrikman can be applied to describe the effects of cluster formation at percolation. Hence, in the present work, the relative permittivity at high liquid fractions is approximated with the upper Hashin-Shtrikman bound defined by Equation 1.19 on page 23. This describes the percolation cluster formed by the liquid phase and treats the ice as inclusions.

In the regime close to the percolation threshold, the two models are blended according to the following formula:

$$\varepsilon_\mathrm{r} = \frac{1}{2}\left[1 - \tanh\left(\frac{v_\mathrm{liq} - v_\mathrm{liq}^*}{\delta}\right)\right]\varepsilon_\mathrm{r,B} + \frac{1}{2}\left[1 + \tanh\left(\frac{v_\mathrm{liq} - v_\mathrm{liq}^*}{\delta}\right)\right]\varepsilon_\mathrm{r,HSU} \quad (5.1)$$

Here v_liq^* describes a threshold for the blending and δ describes the width of the blending. These parameters are fitted to the experimental data of Currie and Fuleki. This equation is also in qualitative agreement with measurements of the relative permittivity of wet soil [114, 94].

Figure 5.6 shows the experimental data of Currie and Fuleki [44], the Bruggeman model with the depolarization factors fitted to this data, the Hashin-Shtrikman bounds and the equation above. In addition, the lower and upper Wiener bounds are shown, which correspond to a laminate perpendicular to the electric field and a laminate parallel to the electric field, respectively.

The fitted model given by Equation 5.1 agrees well with the experimental data. Furthermore, the model is theoretically justified for liquid fractions below percolation as well as for high liquid fractions above percolation. For liquid volume fractions close to the percolation threshold, the employed equation represents an empirical fit.

Conversion from capacitance to relative permittivity As it is common for similar moisture measurements in soil and other porous media, the ice accretion is approximated as a capacitor and a resistor connected in parallel [16, 44]. Parasitic capacitances can be modeled as an additional capacitor in parallel to the ice layer. The parasitic capacitances include the capacitance between the electrodes and the heater, which is at the back of the sensor as well as other capacitances resulting from the wiring or other effects. An equivalent circuit is illustrated in Figure 5.7.

The capacitance of the modeled system is given by

$$C = C_0 + C_\mathrm{g}\overline{\varepsilon}_\mathrm{r}, \quad (5.2)$$

where C_0 summarizes all parasitic capacitances and C_g is from here on called geometric capacitance, since it is only a function of the geometry of the electrodes. $\overline{\varepsilon}_\mathrm{r}$ denotes the effective relative permittivity of the ice layer, weighted according to the sensitivity profile of the sensor. This corresponds to the relative permittivity

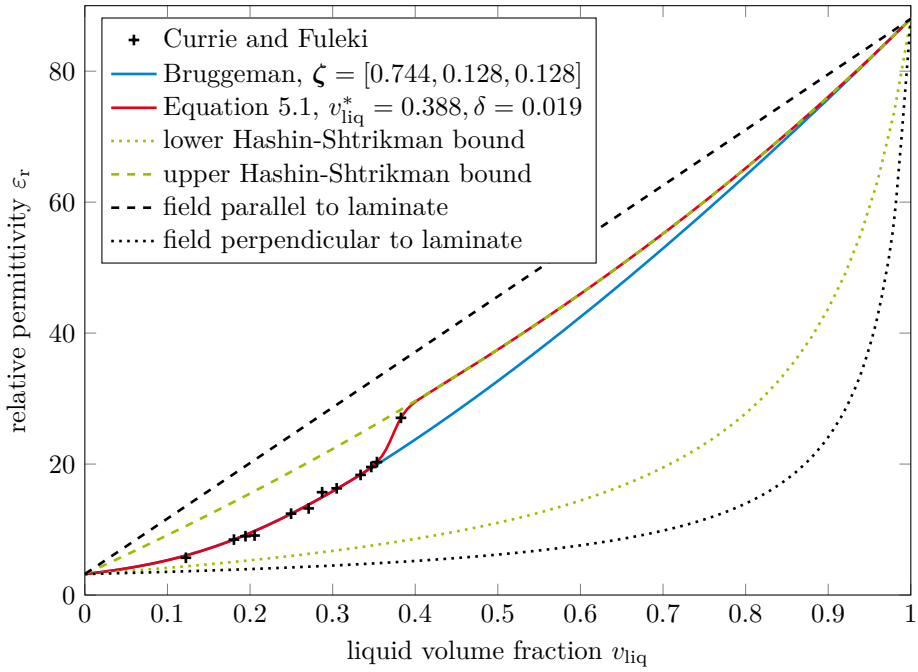

Figure 5.6: Comparison of the fitted dielectric mixing law with the experimental data of Currie and Fuleki. The dashed and the dotted lines correspond to the upper and lower bounds, respectively.

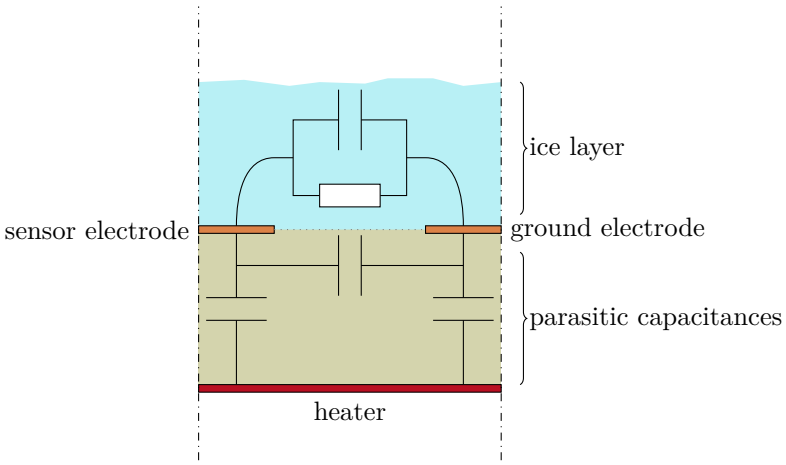

Figure 5.7: Approximation of the capacitive measurement setup as an electrical circuit with the ice layer as a capacitor and resistor in parallel and the parasitic capacitances as another capacitor in parallel to the ice layer.

of a homogeneous medium, which would cause the same capacitance reading, if it replaced the ice accretion. This can be expressed as

$$\overline{\varepsilon}_\mathrm{r} = \int_0^\infty w \varepsilon_\mathrm{r} \mathrm{d}z \tag{5.3}$$

where the weighting function w and the local effective relative permittivity ε_r of the ice layer can both be a function of the distance z to the sensor.

The parameters in Equation 5.2 can be obtained from two measurements with media with known relative permittivities. This allows calibrating the sensor with respect to the relative permittivity. In the present work, the utilized media are air with a relative permittivity of approximately one and isopropanol with a relative permittivity of approximately 20 at 20 °C. Measurements with different materials confirm the linear trend. In these cases the relative permittivity of the medium in front of the sensor is uniform, i.e., $\overline{\varepsilon}_\mathrm{r} = \varepsilon_\mathrm{r}$. Isopropanol is chosen because its relative permittivity is similar to that of a wet ice accretion. With these measurements, the geometric capacitance C_g and the parasitic capacitance C_0 can be calculated. Since the electrode layout of the two utilized sensors is different, the sensors exhibit distinct parasitic capacitances C_0, geometric capacitances C_g and normalized sensitivity profiles $w(z)$. Furthermore, the relative permittivity in the ice layer is not uniform, due to a nonuniform distribution of liquid water. Correspondingly, the measured effective relative permittivity $\overline{\varepsilon}_\mathrm{r}$ of the two sensors is different.

While the parasitic capacitances must be obtained from an experiment in order to include all effects and the exact geometry, the geometric capacitance can also be calculated from numerical simulations. Table 5.1 gives a comparison of the geometric capacitance obtained from experiments and from the simulation.

Table 5.1: Geometric capacitance obtained from the experiments and from simulations.

	geometric capacitance in pF		
	experiment	simulation	relative deviation
large-scale sensor	7.516	7.263	−3.4 %
near-wall sensor	25.245	26.031	+3.1 %

The good agreement between the experimentally and numerically obtained geometric capacitance confirms the reliability of the numerical simulation. With this confidence, the weighting function w utilized in Equation 5.3 can be obtained from the numerical simulations performed for the design of the sensors. The normalized sensitivity used as the weighting function is shown in Figure 5.5 on page 108.

Once the parasitic capacitance C_0 and the geometric capacitance C_g are known, the relative permittivity $\overline{\varepsilon}_\mathrm{r}$ of an effective medium in front of the sensor can be

obtained from Equation 5.2. This can be done for each of the sensors.

In conjunction with the numerically obtained weighting functions w due to the sensitivity range of each sensor, Equation 5.3 provides information on the distribution of liquid water in the ice layer. The two sensors yield a system of two nonlinear equations for the local relative permittivity ε_r.

Numerical algorithm for estimating the liquid distribution The correlation given by Equation 5.1 relates the liquid volume fraction v_liq of an ice accretion to its relative permittivity ε_r. Furthermore, the methodology described above enables the conversion of the capacitances, which are measured with the two sensors, to effective relative permittivities $\overline{\varepsilon}_{\mathrm{r},1}, \overline{\varepsilon}_{\mathrm{r},2}$ weighted according to the sensitivity profiles. These relations enable the estimation of the distribution of liquid volume fraction in the ice accretion. The procedure, which provides the liquid distribution is described in the following.

In this work, the distribution of the liquid volume fraction over the thickness of the ice accretion is approximated as linear. This linearization is limited to small ice thicknesses, in which no significant deviation from the linear profile is anticipated. The liquid volume fraction in the ice layer can then be written as

$$v_\mathrm{liq} \approx v_\mathrm{liq,0} + (v_\mathrm{liq,s} - v_\mathrm{liq,0})\frac{z}{h} \tag{5.4}$$

with the liquid volume fraction at the substrate $v_\mathrm{liq,0}$, the liquid volume fraction at the outer surface of the ice accretion $v_\mathrm{liq,s}$, the distance to the sensor surface z and the mean ice thickness h, which is obtained from a three-dimensional scan of the ice accretion. This equation contains two unknown parameters $v_\mathrm{liq,0}$ and $v_\mathrm{liq,s}$, which can be obtained from the above system of two nonlinear equations. It should be noted that although the equation is expressed in terms of the liquid fractions at the substrate and outer surface, these values cannot be measured explicitly. This imposes a limitation especially for ice accretions thicker than the sensitivity range of the sensors. For thick ice layers, the obtained liquid fraction at the outer surface can be interpreted as an extrapolation of the linear trend measured close to the substrate.

The algorithm yielding the unknown coefficients in Equation 5.4 is illustrated in Figure 5.8. The procedure starts from an initial guess of the liquid volume fraction at the substrate $v_\mathrm{liq,0}$ and at the accretion surface $v_\mathrm{liq,s}$. The linear distribution of liquid water given by Equation 5.4 is then evaluated at numerous sampling points within the ice layer, i.e., $0 \leq z \leq h$. Subsequently, the local values of the liquid volume fraction are converted to relative permittivities with the means of Equation 5.1. This yields a distribution of the relative permittivity in the ice accretion. The relative permittivity beyond the ice accretion, i.e., $z > h$, is set to unity. Equation 5.3 can then be evaluated for each of the two sensors by making use of the corresponding weighting function w due to the different sensitivity ranges. Finally, the obtained weighted average of the relative permittivity is compared to

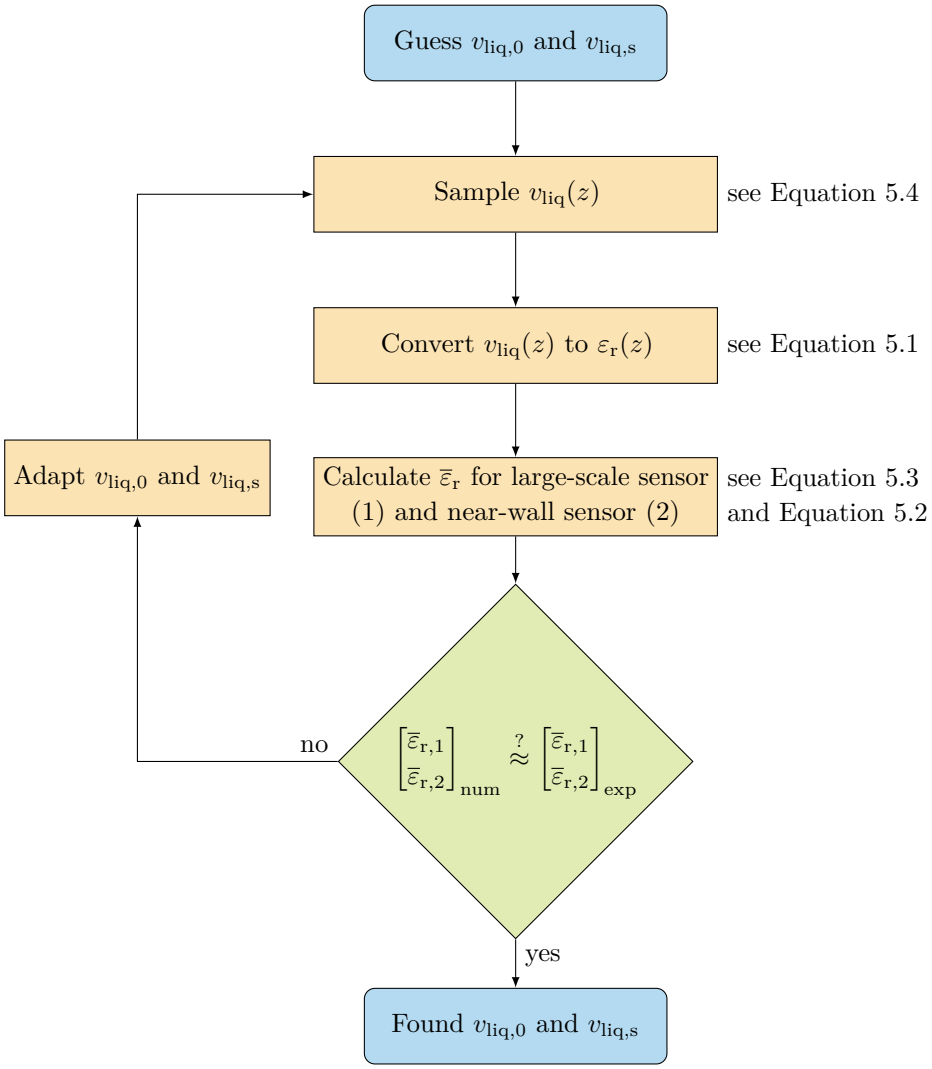

Figure 5.8: Flowchart for the determination of the distribution of liquid volume fraction in the ice accretion.

the corresponding experimental value calculated from Equation 5.2 for each sensor. If the difference between the numerically yielded values and the experimental values is negligibly small, the solution is found and the utilized parameters $v_{\mathrm{liq},0}$ and $v_{\mathrm{liq,s}}$ describe the distribution of liquid water. If the difference of numerically and experimentally obtained values exceeds the tolerance, the parameters are adapted and the next iteration starts with sampling of the expected liquid fractions.

Setup of the measurement equipment

The developed sensors are embedded in a test article, which resembles a flat plate, aligned normal to the airflow. The test article is placed in the test section of the wind tunnel with a width of 0.5 m. In the following, the structure of the test article and the setup of the measurement equipment are described.

The electrodes of the sensors are coated on an aluminum nitride substrate. This ceramic material acts as an electrical insulator and at the same time exhibits a high thermal conductivity of approximately $200\,\mathrm{W\,m^{-1}\,K^{-1}}$. To protect the copper traces that represent the electrodes from corrosion and potential short circuits, a black solder mask is applied to cover the electrodes. The aluminum nitride plate has a length of 210 mm, a width of 44 mm and a thickness of 9 mm. The plate is fixed in a polyamide holder that is used to position the sensor in the center of the test section. The cross-section of this structure is illustrated in Figure 5.9. It incorporates a heating film attached to the back of the aluminum nitride substrate to provide a uniform heat flux to the plate. Thermal insulation at the back of the heater minimizes the heat loss to the back. An aluminum plate and the back of the polyamide holder provide a rigid structure and keep the sensor plate in its position. Similarly, the polyamide side walls hold the sensor and limit the heat loss to the sides. The dimensions and the thermal conductivities of the these materials are listed in Table 5.2.

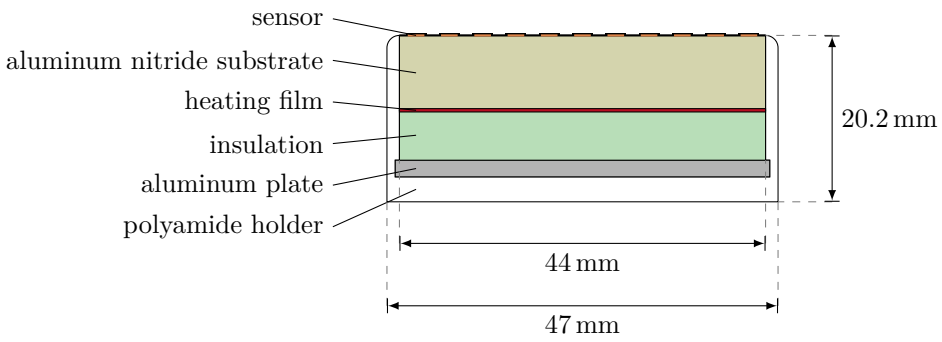

Figure 5.9: Structure of the test article. The thickness of each layer is provided in Table 5.2.

Table 5.2: Thickness and approximate thermal conductivity of the components in the test article.

	Thickness in mm	Thermal conductivity in $\mathrm{W\,m^{-1}\,K^{-1}}$
Aluminum nitride substrate	9	200
Heating film	0.2	–
Insulation	6	0.20
Aluminum plate	2	235
Polyamide side walls	1.5	0.25
Polyamide back wall	3	0.25

The resulting thermal resistance of the aluminum nitride plate is much smaller than the thermal resistances of the thermal insulation at the back and the polyamide walls at the side. Furthermore, the insulation is connected in series with the aluminum plate and the back of the polyamide holder. Thus, the back and the side walls can be considered as adiabatic. Hence, it can be approximated that all heat supplied by the heating film is transferred to the sensor surface and the ice accretion.

A Pt1000 temperature sensor is attached to a corner of the sensor plate to track the temperature evolution of the substrate. Due to the measurement being limited to the local temperature at the corner of the plate and due to imperfections in the heat transfer between the plate and the temperature sensor, the temperature readings only serve as qualitative data.

The plate is placed in the test section such that sensor is aligned normal to the incoming airflow. A view from the wind tunnel nozzle onto the sensor in the test section is depicted in Figure 5.10.

The setup of the measurement equipment is illustrated in Figure 5.11. The heater is connected to a laboratory power supply located outside of the wind tunnel. The wires are enclosed in the polyamide holder. Coaxial cables are attached to the wire terminals on the front surface of the sensor and pass through the polyamide holder. Electrically insulating polyimide tape is applied to protect the wire terminals and the opening in the sensor holder from ice crystals and liquid water. The coaxial cables are connected to an LCR meter outside of the test section. The LCR meter (Rohde & Schwarz HM8118) evaluates the capacitance.

The excitation frequency of the electric field was set to 200 kHz, which corresponds to the maximum frequency supported by the LCR meter. The effective voltage of the sinusoidal signal was set to 1.5 V. The capacitance is measured at a sampling rate of approximately 8 Hz.

The optical setup for the observation of the ice accretion process consists of three cameras and two light sources: Two cameras provide stereo vision for a

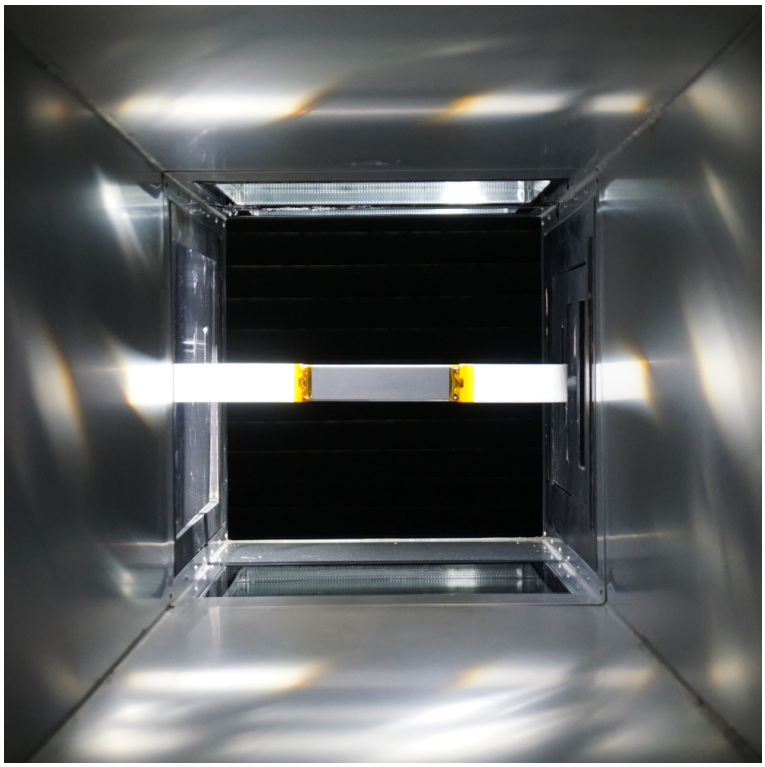

Figure 5.10: Test article in the test section as seen from the wind tunnel nozzle. The sensor can be seen in black in the center of the white polyamide frame. Yellow polyimide tape protects the wire terminals on the sensor.

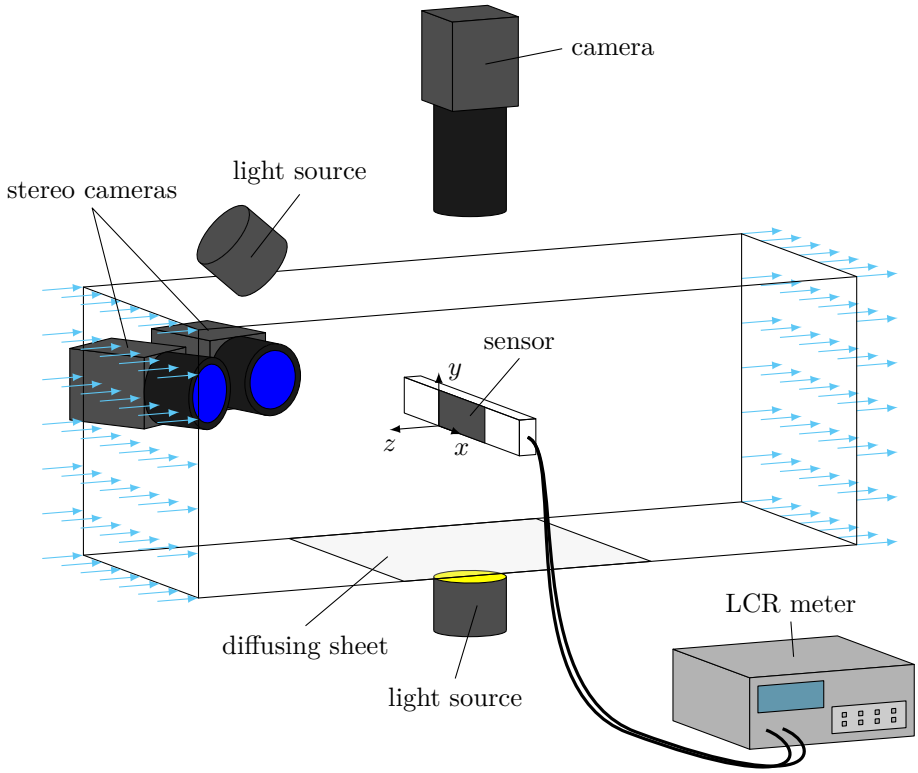

Figure 5.11: Measurement equipment and setup in the icing wind tunnel.

three-dimensional reconstruction of the ice accretion and a third camera observes the accretion process from above the test section. A detailed assessment of the application of stereo vision to ice accretions can be found in the work of Connolly [36]. The cameras in the present stereo vision setup record the accretion process from an oblique perspective and have an angle of approximately 20° between their lines of sight. These recordings are used to generate a three-dimensional reconstruction of the ice layer to assess its shape and evaluate the mean thickness. The light source for the stereo vision setup illuminates the ice layer from an oblique angle from above and the second light source is combined with a diffusing sheet and is located below the test section. The light source below the test section and the top view camera enable shadowgraphy of the ice accretion.

5.2 Observed ice accretion shape

The following sections present the experimental results. First, the directly observable quantities are described. In the present section, the typical shape of the ice accretion is discussed. In the next section, the evolution of the thickness of the ice accumulation is presented. Subsequently, the liquid distribution, considered as the primary driver for ice layer growth, is analyzed. Finally, the sticking efficiency, which links these quantities, is discussed.

In the following, the typical shape evolution and the final three-dimensional ice layer are described. The three-dimensional reconstructions are provided by stereo vision. The evolution of the ice shape is illustrated in Figure 5.12. The depicted curves correspond to the mean profile of the ice accretion at different time instants. The ice layer has a rather uniform thickness at the beginning of the accretion process. However, as time progresses, a peak develops at the stagnation point. Numerical simulations of particle trajectories performed at the aerospace research

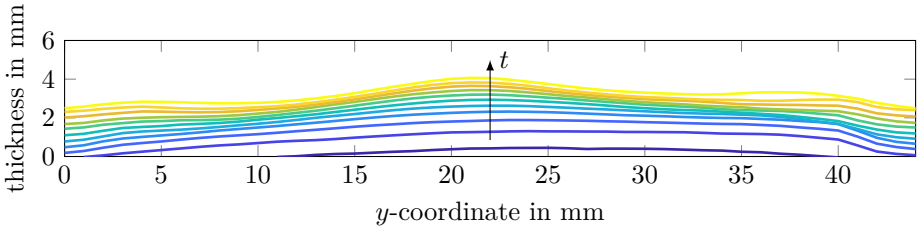

Figure 5.12: Profile of the accretion at different time steps after the start of the ice cloud. The depicted curves represent the mean thickness in the spanwise direction within the sensitive area of the sensor. The bottom curve corresponds to a time of 20 s and the top curve corresponds to 120 s after the start of the experiment. The time increment between the curves is 10 s. The peak at the stagnation point becomes more pronounced toward the end of the experimental run.

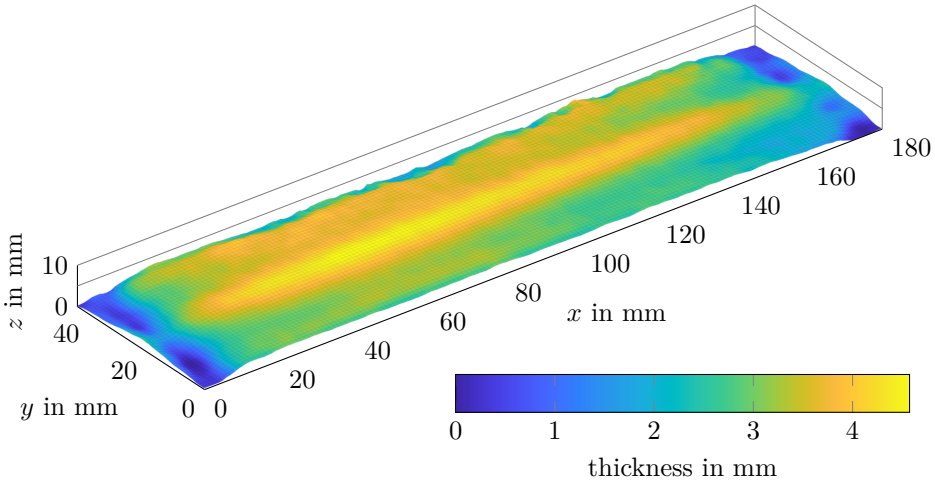

Figure 5.13: Ice accretion 120 s after the start of the ice cloud. The depicted experimental run was conducted with a heat flux of 7.2 kW m^{-2}, an air temperature of −5 °C, a flow velocity of 40 m s^{-1} and an ice water content of 3.9 g m^{-3}.

center ONERA indicate that this effect is not caused by the collection efficiency, i.e., the location of impact due to the particle trajectories. Instead, the formation of the peak is presumably attributed to erosion of the ice accretion due to the impacting ice crystals. This effect is most pronounced toward the end of the experimental run. However, the effects of erosion are limited. This is supported by theoretical considerations of erosion phenomena where the rate of erosion is proportional to the square of the tangential velocity component of the impacting particles [13, 186, 123]. Since the test article is a flat plate normal to the incident flow, the tangential velocity component of the ice crystals is small. The tangential velocity component vanishes at the stagnation point, which results in a negligible erosion rate and the formation of the peak. This neglects erosion effects due to normal impacts, which are typically not considered in accretion modeling [13, 186, 123].

A three-dimensional reconstruction of an exemplary ice accretion at the end of the experimental run of 120 s is depicted in Figure 5.13. The accretion profile is reasonably well approximated by a uniform thickness. Deviations occur at the stagnation point and towards the edges of the plate. The decreased ice thickness at the edges of the accretion in the spanwise direction is due to the polyimide tape used to protect the wiring of the sensor. These regions are located outside of the sensitive region of the sensor and therefore do not affect the measurement of the capacitive sensor.

Since only the sensor plate is heated, no ice accretes at the polyamide holder at negative wet bulb temperatures. However, part of the meltwater flows towards the edges of the plate where runback ice forms. This is more pronounced at higher

heat fluxes.

In the following, the accretion thickness is specified in terms of the thickness at the stagnation point and the mean thickness. The stagnation point thickness is averaged over the span of the plate and can be obtained from shadowgraphy and stereo vision. The mean thickness corresponds to the volume of the ice accretion on the sensor divided by the base area. When assuming a constant density for the ice accretion, the mean thickness is also proportional to the accreted mass. Since the mean thickness is based on the three-dimensional geometry of the accretion, it can only be obtained from stereo vision.

5.3 Evolution of accretion thickness

The evolution of the thickness of the ice accretion with time is presented in Figure 5.14. The stagnation point thickness provides a comparison of the two measurement techniques. Stereo vision relies on the detection of features in the images. However, the clean substrate does not exhibit a sufficient number of features for the three-dimensional reconstruction. The ice layer can be detected more reliably once it covers the entire surface and the ice layer reached a certain thickness. The rough structure of the accreted ice leads to further features that can be recognized by the algorithm. Therefore, the ice layer thickness determined by stereo vision is only shown starting from 30 s after the start of the ice cloud. From this instant on, shadowgraphy and stereo vision are in agreement within typically ± 0.2 mm.

The icing process observed in the present study can be divided into three stages with respect to the evolution of the ice layer thickness:

In the first stage, starting with the onset of the ice cloud, impinging ice crystals cause the formation of droplets on the heated substrate and lead to a decrease of the substrate temperature. During this stage, meltwater accumulates on the surface and forms clusters that eventually result in a liquid film.

Once the substrate surface reaches 0 °C, the second stage commences and ice accretes, spreads over the substrate and grows rapidly in thickness. For the experimental conditions shown in Figure 5.14, the inception of ice accretion occurs approximately 20 s after the ice crystals are introduced. Following this abrupt increase, the rate at which the accretion grows decreases.

In the third stage, the ice thickness continues to increase at an approximately constant rate. This stage concludes the experiments conducted in this study. In the present study, the growth rate is defined as the temporal derivative of the accretion thickness at the stagnation point. This provides a measure for the icing severity. The growth rate derived from the data in Figure 5.14 is shown in Figure 5.15. Since the growth rate decreases asymptotically, a distinct point in time which marks the transition from stage II to stage III cannot be determined. The time instance of 50 s indicated in the figures should therefore only be regarded as an approximate

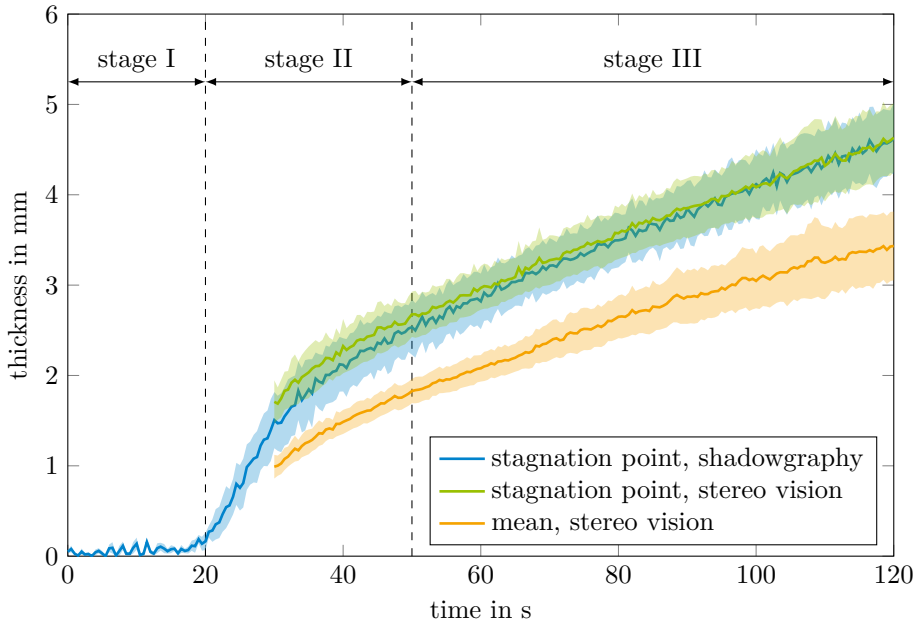

Figure 5.14: Ice accretion thickness as a function of time. The maximum thickness was measured by stereo vision as well as by shadowgraphy. The average thickness requires a three-dimensional measurement and is thus only obtained from stereo vision. The shaded areas indicate the 95 % confidence intervals obtained from ten experiments. The experimental runs were conducted at a heat flux of $7.2\,\mathrm{kW\,m^{-2}}$, an air temperature of $-5\,°\mathrm{C}$, a flow velocity of $40\,\mathrm{m\,s^{-1}}$ and an ice water content of $3.9\,\mathrm{g\,m^{-3}}$.

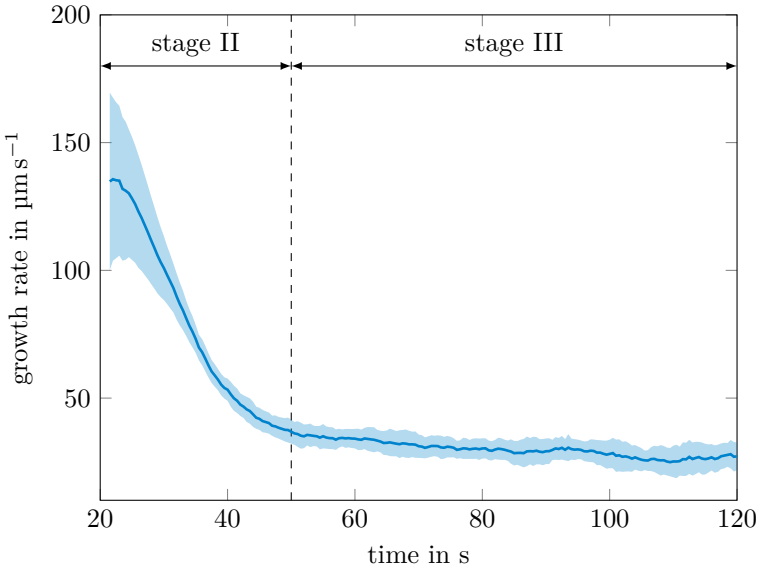

Figure 5.15: Growth rate obtained from the evolution of the accretion thickness at the stagnation point for the same experimental conditions as in Figure 5.14.

value.

The wet bulb temperature, the substrate heat flux and the ice water content have been systematically varied in a parameter study. The investigated wet bulb temperature ranges from −15 °C to +2.5 °C. The heat flux averaged over the sensor surface extends from 4.5 kW m^{-2} to 12.8 kW m^{-2} and the ice water content is in the range of 3.7 g m^{-3} to 7.6 g m^{-3}. These parameter ranges are deemed typical for ice crystal icing. To assess the repeatability, each experiment has been performed at least four times. In the following, the effects of these parameters on the accretion thickness are discussed.

The experiments conducted at a positive wet bulb temperature exhibit a behavior that is qualitatively different from that at negative wet bulb temperatures. The corresponding evolution of the ice accretion thickness is shown in Figure 5.16 with the 95 % confidence interval obtained from four experimental runs. At these experimental conditions, the ice particles already partially melt in the airflow. Stage I is not significantly affected by this change, since the surface of the substrate first has to decrease to 0 °C before an accretion starts to form. Following the inception of ice accretion, the ice layer grows rapidly. However, since the partially melted particles supply liquid water, the growth rate is not limited by the transport of liquid water through the ice layer. Therefore, no significant decrease in growth rate can be observed for the experimental runs conducted at 2.5 °C.

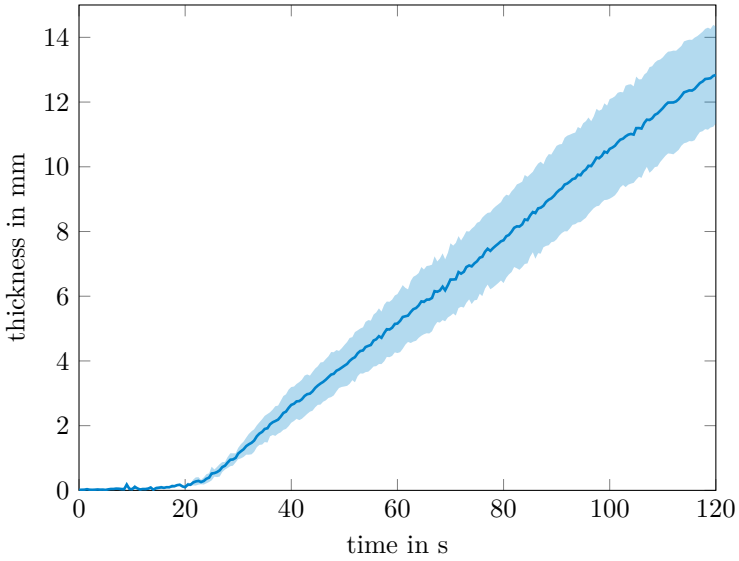

Figure 5.16: Ice accretion thickness at the stagnation point as a function of time at a positive wet bulb temperature. The experimental runs were conducted at a heat flux of $7.2\,\mathrm{kW\,m^{-2}}$, an air temperature of $2.5\,°\mathrm{C}$, a flow velocity of $40\,\mathrm{m\,s^{-1}}$ and an ice water content of $4.0\,\mathrm{g\,m^{-3}}$.

An overview of the influences of wet bulb temperature, heat flux and ice water content on the accretion thickness is presented in Figure 5.17. In this figure, the accretion thicknesses at the stagnation point are compared at an arbitrary time after the onset of accretion. A more detailed understanding of these trends is provided by the analysis of the liquid distribution in the ice accretion and the resulting sticking efficiencies which are discussed in the subsequent sections 5.4 and 5.5. It should be noted that the depicted trends are the result of all three stages of ice accretion. An increase in air temperature and heat flux lead to a delayed onset of accretion, resulting in more liquid water accumulating on the test article. As a consequence, the rapid growth of the ice layer in stage II is more pronounced and sustained for a longer period of time and thus also affects the subsequent thickness evolution.

The influence of wet bulb temperature on the ice layer thickness 80 s after the onset of accretion is shown in Figure 5.17a. An increasing temperature yields an increase in accretion thickness.

The effect of the heat flux supplied to the substrate on the accretion thickness is presented in Figure 5.17b. An increasing heat flux yields an increasing ice layer thickness since more liquid water is transported to the accretion front.

Finally, the influence of ice water content on the accretion thickness is shown in Figure 5.17c. The rising trend is attributed to the increasing supply of ice crystals.

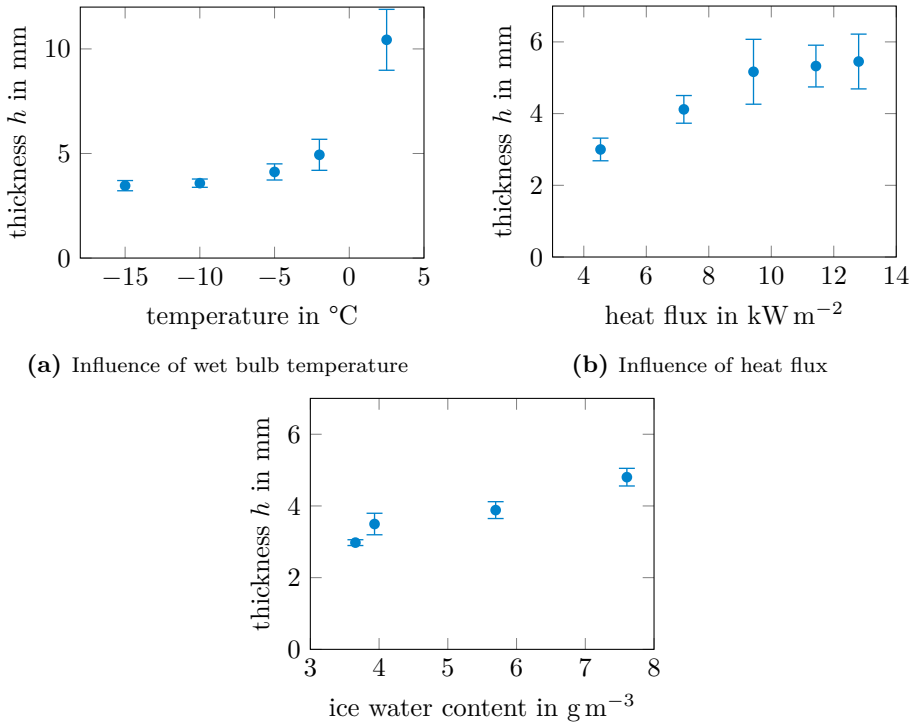

(a) Influence of wet bulb temperature

(b) Influence of heat flux

(c) Influence of ice water content

Figure 5.17: Influences of the wet bulb temperature, the heat flux and the ice water content on the stagnation point ice thickness at a fixed time after the inception of ice accretion. For figures (a) and (b) the thickness was evaluated at an arbitrary time of 80 s after ice inception and for figure (c) the time was set to 60 s. The error bars in this figure, and in the figures that follow, represent the 95 % confidence interval.

5.4 Distribution of liquid water

Since ice crystal icing is only enabled by the presence of liquid water, it is expected that the liquid volume fraction of the ice accretion determines the accretion process. The newly developed measurement technique and the procedure described in subsection 5.1.2 enable the quantification of the distribution of liquid water in the ice accretion.

Figure 5.18 shows the evolution of the liquid volume fractions at the substrate and at the outer surface of the accretion. The procedure which yields the liquid distribution does not return reliable results for very thin ice layers. Therefore, the graphs displayed in Figure 5.18 start with a delay with respect to the inception of accretion.

In stage II, the liquid volume fraction at the surface of the ice layer decreases drastically. This coincides with the rapid increase in accretion thickness seen in Figure 5.14 and the decrease in growth rate seen in Figure 5.15. This suggests that the liquid fraction at the surface determines the sticking efficiency, i.e., the fraction of the impinging ice crystals that sticks to the surface. Prior to the inception of ice accretion an abundance of liquid water is available on the surface of the substrate, since the residue of impacting particles is completely melted due to a substrate temperature above 0 °C. This large amount of liquid water enables a large number of ice crystals to stick to the surface. With the formation of the ice accretion, newly

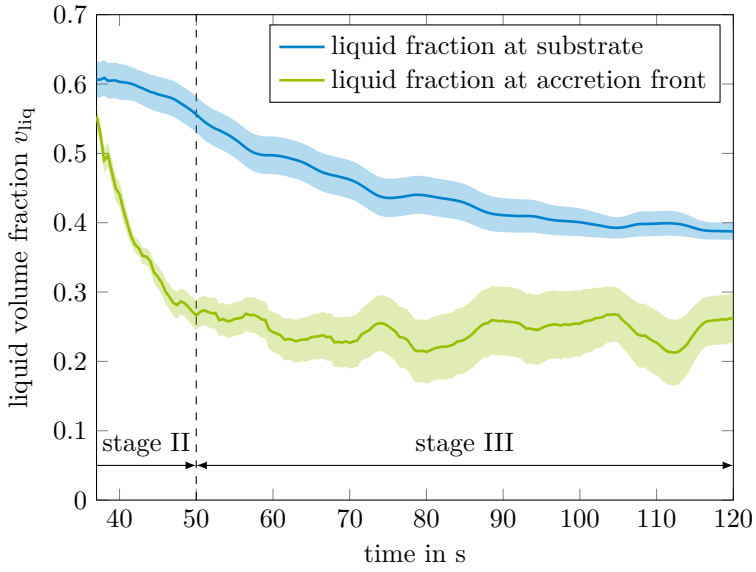

Figure 5.18: Measured liquid volume fractions at the substrate and at the outer surface of the ice accretion. The experimental conditions correspond to those specified for Figure 5.14.

adhering ice crystals withdraw heat from the liquid on the substrate. This causes freezing of a fraction of the liquid water on the substrate, which reduces the liquid volume fraction on the surface. The reduced liquid fraction on the surface then causes a decrease in sticking efficiency.

In stage III, which is defined by a constant growth rate, the liquid fraction at the outer surface remains constant. The liquid fraction at the surface of the ice accretion approaches a value of approximately 25 %. Due to the increasing distance of the accretion front from the sensor, the obtained values have a higher uncertainty in comparison to the values at the substrate. The experimental methodology approximates the distribution of the liquid fraction as linear, which might no longer be valid for thicker ice layers. Furthermore, in experiments with thicker ice layers, the accretion front may leave the sensitivity range of the sensors.

The constant liquid volume fraction at the accretion surface results in a constant growth rate. This indicates that the liquid water content at the surface reached an equilibrium. On the one hand, meltwater flows from the interface to the heated substrate through the ice layer to the accretion front. This supplies liquid water to the surface. On the other hand, ice crystals adhering to the accretion bind liquid water, which reduces the liquid fraction. Furthermore, convective heat transfer to the cold airflow removes latent heat from the accretion and can cause refreezing of meltwater. A constant rate of growth prevails when these effects are in equilibrium.

The liquid fraction at the interface of the substrate and the ice accretion decreases continuously during the experimental run. A large amount of meltwater has accumulated on the substrate prior to the inception of accretion. As the ice layer grows, more and more water is drawn from the substrate surface. This enables the rapid increase of the ice layer thickness at the beginning of stage II.

The liquid fraction at the substrate continues to decrease in stage III. However, the value appears to level out. For the experimental conditions depicted in Figure 5.18, the liquid fraction at the substrate appears to asymptotically approach a value of approximately 39 %.

Although the presented measurements provide information on the liquid volume fraction of the ice accretion, they do not enable the quantification of pore saturation as the porosity of the accretion is not known. However, observations with a slightly modified test article suggest that the pores might not be fully saturated. For this investigation, the test article is adapted by extending the non-heated side walls of the polyamide holder. Experiments with this modified configuration reveal that the liquid fraction at the substrate diminishes and reaches zero even though an ice layer is present on the substrate. A visual inspection of the ice layer shows that it formed a bridge over the heated substrate. The bridge is supported by ice that connects to the non-heated side walls. The fact that the void between the ice accretion and the heated sensor is dry and not filled with liquid water indicates

that the generated meltwater is imbibed by the ice layer. This suggests that the pores of the ice accretion are not saturated.

In the following, the influences of wet bulb temperature, heat flux and ice water content on the liquid fraction of an ice accretion are investigated. One possibility for comparing the various experimental runs with regard to the liquid distribution would be to analyze the results at a fixed time after the start of the experiment. However, this would result in large discrepancies in accretion thickness. Since the thickness over which the liquid water is distributed is expected to affect its distribution, a comparison at a fixed time does not enable an isolated analysis of each influence. Furthermore, the limited spatial sensitivity range of the sensor does not provide accurate results for very thick ice layers. Therefore, an alternative approach is chosen in which the liquid distributions in the ice accretions are compared at a fixed thickness of the ice layer. While this approach eliminates the influence of accretion thickness, the different time instances at which the parameters are compared can affect the results. Therefore, it will be mentioned if certain data points were acquired at a significantly different time after the start of the experiment. The mean accretion thickness for which the liquid distributions in the ice layers are compared is chosen as 2 mm, which is within the sensitivity range of the sensors and includes most experimental runs.

The influence of wet bulb temperature on the liquid volume fraction at the interface to the substrate and at the accretion front is shown in Figure 5.19a. No data points are presented for a wet bulb temperature of −15 °C, since the mean ice layer thickness did not reach 2 mm. Due to a decreasing growth rate with decreasing temperature, the data points at lower temperatures correspond to later times in the experiments. The liquid fraction at the interface to the substrate increases significantly with increasing wet bulb temperature. This is partially attributed to the increasing volume of liquid that accumulates on the substrate prior to the onset of accretion. An increase in air temperature results in less convective cooling of the substrate. Thus, to reach a surface temperature of 0 °C, more heat must be withdrawn by melting ice crystals, which increases the volume of meltwater on the test article. A minor contribution can be attributed to the decreased sensible heat required to melt the ice particles at higher temperatures. The increased availability of liquid water from the heated substrate also leads to an increase in liquid fraction at the accretion front. Furthermore, lower air temperatures enhance convective cooling, which reduces the melting rate and thus the liquid fraction at the substrate. Similarly, a decreasing air temperature leads to more pronounced refreezing of water at the outer surface of the accretion.

The effects of heat flux on the distribution of liquid water in the ice accretion are shown in Figure 5.19b. The data points at the lowest heat flux of 4.5 $\mathrm{kW\,m^{-2}}$ correspond to a significantly later time than the other data points at higher heat fluxes, since the growth rate was smaller at these conditions. It appears that

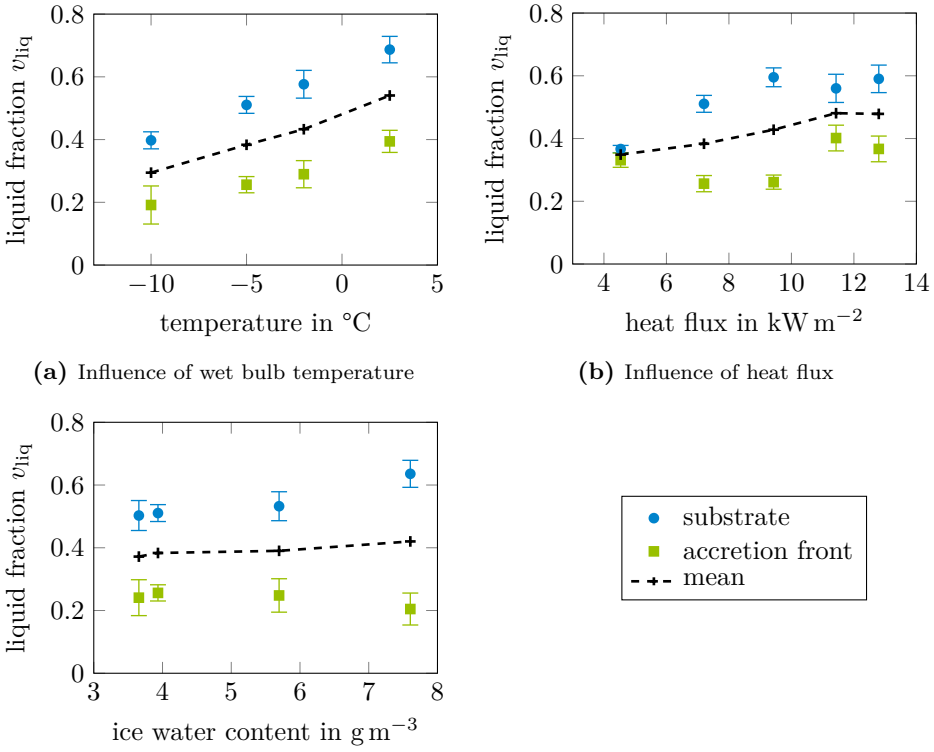

(a) Influence of wet bulb temperature

(b) Influence of heat flux

(c) Influence of ice water content

Figure 5.19: Influences of the wet bulb temperature, the heat flux and the ice water content on the liquid volume fraction of ice accretions with a mean thickness of 2 mm. The parameter variation is performed around the default conditions with a wet bulb temperature of −5 °C, a heat flux of 7.2 kW m^{-2} and an ice water content of approximately 3.9 g m^{-3}.

the liquid fraction at the substrate first increases with increasing heat flux before reaching a plateau of close to 60 % at heat flux levels of 9.4 kW m^{-2} and above. This could be related to the increasing formation of runback ice on the side walls of the test article by water that is not imbibed by the ice layer but transported to the edges of the test article. However, it should be noted that the assumption of a linear distribution of liquid water in the accretion may not hold at higher heat fluxes. In an extreme case, the ice accretion may float on a liquid film, resulting in a layer of pure liquid and a nonlinear water distribution in front of the sensor. Nonetheless, the estimated mean liquid fraction of the ice accretion shows an increase with increasing heat flux.

Finally, the effects of different ice water contents are presented in Figure 5.19c. Of these data points, the values at higher ice water contents were recorded earlier in the experiments. This is presumably responsible for the slight increase in the liquid fraction at the substrate. Overall, a change in ice water content does not appear to have a significant impact on the liquid fraction of an ice accretion.

5.5 Sticking efficiency

The sticking efficiency describes the fraction of the impacting ice mass that adheres to the surface of the test article or the ice accretion. Therefore, this quantity plays a crucial role for the modeling of the accretion process. Since ice layer growth is only enabled by the presence of liquid water, it can be expected that the sticking efficiency is a function of the liquid fraction at the location of ice crystal impact. This relation can be derived from the experiments.

Neglecting the effects of erosion, the sticking efficiency η_s can be calculated by

$$\eta_\mathrm{s} = \frac{\dot{h}\rho_\mathrm{acc}}{\eta_\mathrm{c} IWC u} \tag{5.5}$$

with the growth rate $\dot{h}$, the density of the ice accretion ρ_acc, the ice water content IWC, the flow velocity u and the collection efficiency η_c. In order to minimize the effects of erosion on the obtained values, the growth rate $\dot{h}$ is evaluated at the stagnation point, where the tangential velocity component of the impacting particles vanishes. The collection efficiency represents the ratio of the impacting mass flux to the freestream mass flux. A numerical simulation of the particle trajectories performed at the aerospace research center ONERA yields a collection efficiency of $\eta_\mathrm{c} = 0.876$ at the stagnation point. The density of the ice accretion is estimated as $\rho_\mathrm{acc} \approx 940\,\mathrm{kg\,m^{-3}}$, which accounts for the mixture of ice and liquid water.

It must be considered that, given the geometry of the test article, particles that rebound upon initial impact may subsequently impact the surface again.

The capacitive sensors enable the calculation of the liquid volume fraction at the outer surface of the accretion, which can be related to the obtained sticking

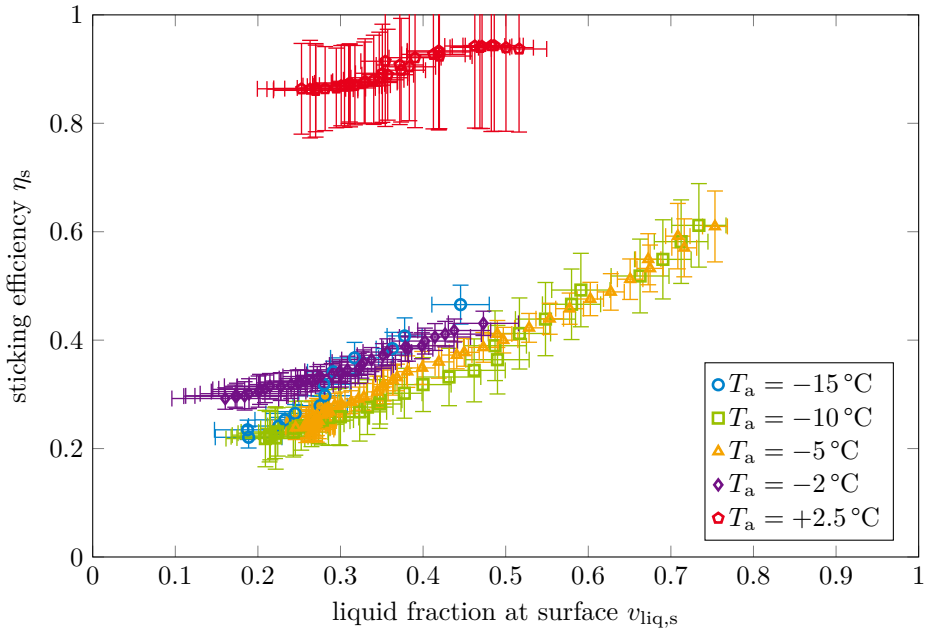

Figure 5.20: Experimentally obtained relation between the sticking efficiency and the liquid volume fraction at the accretion front. The relationship is plotted for different wind tunnel temperatures ranging from negative to positive wet bulb temperatures. The experiments were conducted at a heat flux of $7.2\,\mathrm{kW\,m^{-2}}$ and an ice water content of approximately $3.9\,\mathrm{g\,m^{-3}}$.

efficiency. Due to the low sensitivity of the sensor at distances greater than 2 mm and the linearization of the liquid distribution in post-processing, the maximum ice layer thickness that can be processed is limited. For ice layers significantly thicker than 2 mm, the post-processing can be considered as an extrapolation of the measured linear trend. Therefore, the evaluation of the relation of sticking efficiency and liquid fraction is only performed for stage II when the accretion starts to form.

Figure 5.20 shows the experimentally obtained relation between the sticking efficiency and the liquid fraction at the outer surface of the ice accretion. The relationship is shown for different wind tunnel temperatures. Since the air in the wind tunnel is saturated with water vapor, the indicated air temperature is equal to the wet bulb temperature. The data show an increase in sticking efficiency with increasing liquid fraction. This is in line with the expected behavior, since liquid water enables the adhesion of ice crystals. Due to the hydrophilic nature of ice, the available liquid water wets the impacting particle and capillary forces pull the particle towards the liquid film, as observed by Hauk [72]. Thus, the presence of liquid water hinders the particle from detaching from the surface. Furthermore,

the cold particle withdraws heat from the ice accretion, which causes liquid water at the surface to freeze and form a solid connection between the particle and the accretion. This could contribute to the steeper increase in sticking efficiency with increasing liquid fraction seen in the experiments performed at the lowest wet bulb temperature of −15 °C. The measurements taken at a wet bulb temperature of −2 °C exhibit a slightly higher sticking efficiency than those conducted at −5 °C and −10 °C. This difference can presumably be attributed to the particles not being fully frozen upon impact. While the wind tunnel maintains a wet bulb temperature of −2 °C, the pipe that transports the ice particles to the wind tunnel operates at a higher temperature. Consequently, the ice particles may experience a minor degree of melting, which could account for the observed increase in sticking efficiency. This effect becomes more pronounced at lower liquid fractions at the accretion front, as the water present at the surface alone would only result in a minor sticking efficiency. Therefore, at drier conditions, the measurements at −2 °C diverge from the other measurements.

The data points at a wind tunnel temperature of 2.5 °C shown in Figure 5.20 demonstrate a behavior that is qualitatively different than that at temperatures below 0 °C. For this positive temperature, no significant dependency of the sticking efficiency on the liquid fraction at the wall can be recognized. This is attributed to the fact that these particles have already partially melted. Therefore, the particles provide the necessary liquid water for adhesion without requiring additional water to be present at the location of impact. Thus, the growth rate of the ice layer is not governed by the liquid fraction available at the accretion front, which is determined by water transport through the ice accumulation. Instead, the constant melt ratio of the impacting particles determines the accretion process, resulting in a constant rate of growth. This is consistent with the findings of Currie et al. [46], who studied the sticking efficiency in the positive wet bulb temperature regime.

Furthermore, the sticking efficiency at the investigated positive wet bulb temperature is significantly larger than those observed at temperatures below freezing. This is suspected to be due to the wetting of the impacting particle. While for fully frozen ice particles, a three-phase contact line needs to propagate along the surface of the particle upon contact with liquid water, at positive wet bulb temperatures the particle is already wetted over a larger surface area, which promotes sticking. This highlights the importance of an adequate understanding of ice particle melting, which is discussed in chapter 3.

Due to the limited sensitivity range of the capacitive sensors, an accurate measurement of the liquid fraction at the accretion front is restricted to ice layers of small thickness. Furthermore, the applied methodology assumes a linear distribution of the liquid fraction in the accretion, which is expected to be invalid for high heat fluxes or thick ice layers. Therefore, in stage III of the accretion process, i.e., once the growth rate approaches a constant value, the evaluation of the liquid fraction

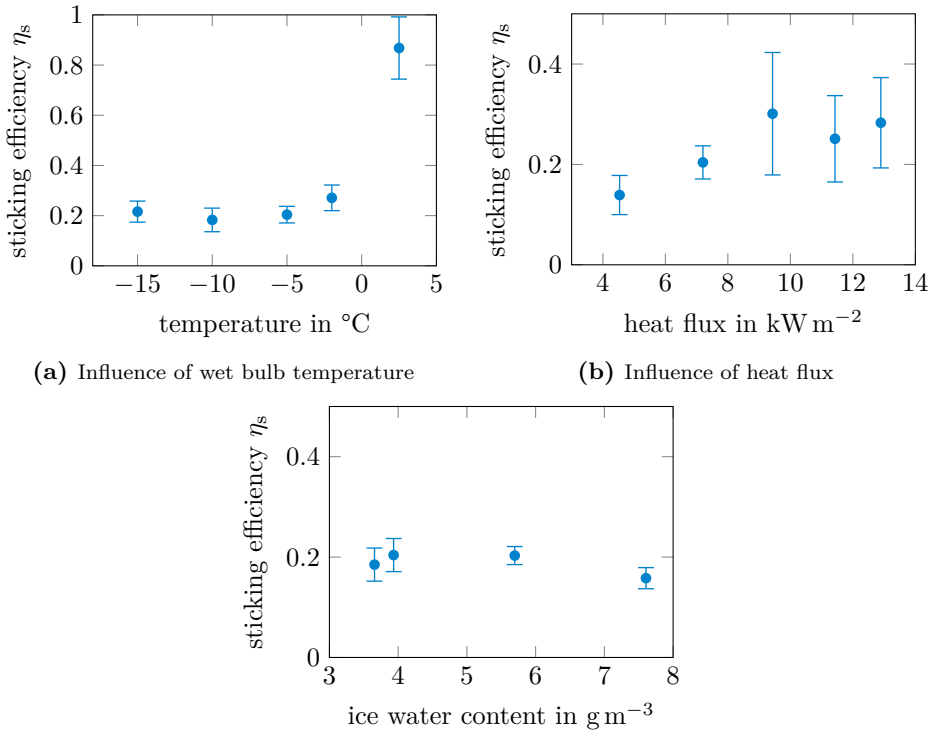

(a) Influence of wet bulb temperature

(b) Influence of heat flux

(c) Influence of ice water content

Figure 5.21: Influences of the wet bulb temperature, the heat flux and the ice water content on the sticking efficiency in stage III, i.e., when the ice layer grows at a constant rate. The parameter variation is performed around the default conditions with a wet bulb temperature of −5 °C, a heat flux of 7.2 kW m^{-2} and an ice water content of approximately 3.9 g m^{-3}.

at the outer surface of the accretion can be unreliable. However, the influences of air temperature, heat flux and ice water content on the sticking efficiency can be investigated.

Figure 5.21 shows the effects of the various influences on the sticking efficiency once the accretion grows at a constant rate. The most significant effect can be recognized in Figure 5.21a, where the influence of wet bulb temperature is shown. At a positive wet bulb temperature, accretion is not limited by the water transport through the ice layer. Therefore, the sticking efficiency remains at a high level. In contrast, at negative wet bulb temperatures, accretion is dictated by the supply of meltwater from the heated substrate to the surface of the accretion. Here, lower ambient temperatures are expected to lead to refreezing of liquid water at the accretion front. This effect could reduce the availability of liquid water, allowing fewer ice crystals to adhere to the surface, corresponding to a decreasing sticking

efficiency with decreasing temperature. However, this effect appears to be small compared to the inherent scatter.

The effect of heat flux on the sticking efficiency in stage III is shown in Figure 5.21b. The data suggest an increase in sticking efficiency with increasing heat flux. However, the conclusiveness is limited by the uncertainty in the data. An increased heat flux results in an increased supply of liquid water at the interface to the substrate. However, not all of the water is transported to the accretion front and thus the increase in sticking efficiency is limited. At high heat fluxes, a non-negligible proportion of the water is transported to the edge of the test article and causes the formation of runback ice on the side walls. This does not contribute to an increase in ice layer thickness and therefore does not result in an increase in sticking efficiency.

Finally, the variation of ice water content does not show a significant influence on the experimentally determined sticking efficiency. The slightly lower value at the highest investigated ice water content is presumably caused by erosion of the ice layer. This effect appears to be more pronounced at high ice water contents, resulting in a more pronounced decrease in accretion thickness towards the edges of the test article. The constant sticking efficiency indicates the proportionality of growth rate and ice water content, as can be recognized in Equation 5.5.

5.6 Summary

An novel capacitive sensor has been developed, which enables quantifying the distribution of liquid water in an ice accretion. The sensor is employed in an icing wind tunnel to investigate the role of liquid water in the accretion process. Additionally, the three-dimensional shape of the ice layer has been characterized using stereo vision, enabling the derivation of the mean thickness as a measure of the accreted volume. The thickness of the accretion at the stagnation point is additionally captured by shadowgraphy. Combining the measurements reveals the relationship between the liquid volume fraction at the accretion front and the rate of ice accretion, represented by the sticking efficiency. This relationship is a crucial input for numerical tools for the prediction of icing. However, it is usually obtained by fitting model parameters to minimize the deviation of the predicted and measured ice thickness and shape. The present study represents the first experimental measurement of this relation in a more direct manner in wind tunnel experiments.

The accretion process is found to follow three stages: In the first stage, the test article cools down by the melting of impacting particles. At the beginning of the second stage, defined by the onset of ice accretion, a film of liquid water has accumulated on the substrate. This results in a high sticking efficiency which yields a drastic growth rate of the ice layer. The adhering ice crystals lead to a decrease in liquid fraction, which in turn results in a decrease in sticking efficiency

and thus, growth rate. The third stage of the accretion process is defined by an approximately constant growth rate caused by an equilibrium of supply of liquid water from the heated substrate and the reduction of liquid fraction due to ice layer growth.

The liquid volume fraction of ice layers of identical thickness increases with increasing wet bulb temperature and increasing heat flux. This increase is most pronounced in the liquid fraction at the interface to the substrate, which determines the supply of liquid water.

The presented results enable a better understanding of the role of liquid water in the process of ice accretion. The measurement of the distribution of liquid water in realistic ice accretions on heated substrates is unprecedented in literature. Furthermore, the characterization of the relation of sticking efficiency and liquid fraction represents a finding that was previously inaccessible to experimental measurements. The newly developed methodology has the potential to provide further insight into different phenomena in the framework of icing.

6 Summary and outlook

The present work is driven by the need for a better understanding of the physical phenomena associated with icing caused by snowflakes and ice crystals, which poses a serious threat in aviation. The involved physical phenomena are manifold and not completely understood. Especially for snowflakes, which assume highly complex shapes, transport processes are not fully elucidated. Furthermore, although the role of liquid water has been identified as a key driver of icing induced by ice crystals and snow, studies on the liquid content of ice accretions are sparse. The advancement of numerical tools for the prediction of aircraft icing requires a deeper insight into the underlying mechanisms to improve aviation safety.

To contribute to an enhanced understanding of snow and ice crystal icing, several interlinked physical transport processes have been investigated in this thesis. Dedicated experimental setups in this study provided detailed insight into each of these phenomena.

Drag of snowflakes

In the first part of this thesis, transport processes of airborne particles are discussed. Chapter 2 encompasses an experimental investigation of the drag of snowflakes, along with the presentation of methods for predicting the drag coefficient based on three-dimensional and two-dimensional simplifications.

The experiments are conducted with artificial snowflakes produced by additive manufacturing, which enables capturing the detailed geometry of the particles. The model of Hölzer and Sommerfeld [81] demonstrates accurate prediction of the drag coefficient when the exact three-dimensional particle geometry is available. Due to the inherent complexity of natural snowflake structures, this information is generally not available. Therefore, a shape simplification based on the convex hull of the particle is proposed. Theoretical considerations indicate that the flow through the pores of this convex body can be neglected within a broad range of particle porosities, pore sizes and Reynolds numbers relevant for natural snow conditions. Therefore, the drag force experienced by the snowflake can be approximated by the drag force of the convex hull, which is obtained from drag models for irregular particles in literature. In contrast to the intricate geometry of snowflakes, which encompasses their internal structure, the geometry of the convex hull can be measured for natural snowflakes, as demonstrated by Leinonen et al. [110]. In addition to providing a simplified geometry, it is found that the utilization of the convex hull results in an enhanced prediction of the drag force.

Furthermore, it is shown that the relevant three-dimensional descriptors of the convex body, given by its volume equivalent diameter and sphericity, can be estimated from the area equivalent diameter and the Cox roundness of two-dimensional convex hull projections.

These findings enable an improved prediction of the drag of snowflakes based on reduced information on the particle geometry and can thereby enhance trajectory calculations required by numerical tools for the prediction of icing.

In future studies, the detailed motion and orientation of the particle in the flow could be investigated. While the present work suggests that the particle orients such that the area projected into the direction of flow is maximized, the rotating motion and oscillations in the orientation and the influence of Reynolds number on this behavior are not investigated in detail. McCorquodale and Westbrook [134] used similar methods to conduct exploratory experiments on the unsteady motion of falling ice particles, but further research is necessary to understand these transient effects.

While the proposed convex hull approach yields a significant simplification of the particle geometry, it may not accurately account for the presence of large pores, which can influence the predicted drag coefficient. To address this limitation, a potential next step in modeling could involve the application of morphological closing, selectively closing only small pores based on a diameter threshold determined by the Reynolds number.

Melting of snowflakes

Chapter 3 addresses the melting of snowflakes in forced convection. In the experiments, laboratory-generated snowflakes suspended in an acoustic levitator are melted in a warm airflow.

As observed in previous studies by Knight [102], Matsuo and Sasyo [130] and Mitra et al. [141], capillary forces drive the meltwater into the pores of the particle. As a consequence, in an early stage of the melting process, the aspect ratio of the particle appears to be only weakly affected by meltwater. As the particle size decreases and the pores become more saturated, liquid water starts to enclose the particle. In the final stage of melting, the residual ice is fully encapsulated by a liquid drop. Eventually, the residual ice melts, which marks the completion of the melting process.

These experimental findings contribute to the development of a theoretical model to describe snowflake melting. The imbibition of meltwater and the fractal aspects of snowflakes justify the use of a mass–size relationship in form of a power law to describe the structure of the particle. Based on the findings in chapter 2, heat and mass transfer are modeled by approximating the convex hull of the particle as an ellipsoid. The proposed model is validated by comparing its predictions of particle size evolution and melt time with the experimental results, demonstrating good

agreement between the model and the experiments. The developed model requires fewer empirical correlations compared to previous models in literature. Suitable parameters for the mass–size power law across various morphological classes can be obtained from existing literature, allowing for the application of the model to a wide range of ice particles, including graupel, hailstones and single crystals.

The reported results enable an enhanced prediction of the melting of airborne particles, which is a crucial input to numerical tools for icing processes.

The proposed model assumes the validity of a mass–size relationship to describe the particle structure during melting. In order to make use of parameters from literature, structural rearrangements during melting must be neglected. Therefore, following studies should focus on the potential collapse of snowflake branches to account for these effects and improve the accuracy of the model predictions.

Imbibition into granular ice layers

The second part of this thesis focuses on the water transport in porous ice accumulations. In chapter 4, initially dry granular ice layers are melted in a controlled environment and the imbibition of meltwater is investigated.

Melting of the ice layer at a constant rate results in a constant wetting front velocity, suggesting that gravity plays a negligible role in imbibition processes at the investigated length scales. The wetting front velocity is primarily determined by the melting induced volume flux and no significant influence of porosity or grain size is observed. This effect is presumably attributed to unsaturated flow along the network of surface grooves, which is governed by the ice crystal morphology.

A capacitive sensor is designed to investigate the saturation of the pores in the wetted region. The sensor is capable of measuring the space and time resolved liquid content in the granular layer. The sensor has a spatial resolution of 2 mm, is calibrated *in situ* to ensure independence from ice layer properties and experimental conditions, and the measured values agree well with the total liquid content evaluated from video recordings.

Under the studied boundary conditions, the pores are found to be unsaturated and the saturation decreases significantly from the melting front to the wetting front. The saturation decreases with increasing porosity, due to the increased pore volume in which the liquid is distributed. Moreover, an increasing volume flux and a decreasing ice crystal grain size result in a sharper decline in saturation. This highlights the dynamics of unsaturated flow and is in accordance with trends anticipated from Richards' equation. The optical observations suggest that liquid accumulates when the wetting front reaches the upper edge of the granular ice layer, which prevents flux across the upper boundary. Finally, as the remaining pores become infiltrated, it is observed that air bubbles are trapped in the wet granular layer.

The conducted experiments provide insight into the processes involved in imbibi-

tion into melting granular ice layers. The presented data can be used to enhance water transport models and account for effects of porosity and grain size.

The developed sensor is proven to work well for granular ice layers well below saturation. However, due to the arrangement of the electrodes, its applicability to higher saturation levels is limited. This could be addressed in an improved version of the sensor.

Liquid water in ice accretions

Chapter 5 of this thesis provides insight into the liquid content of ice accretions formed on heated substrates under realistic ice crystal icing conditions. Additionally, the effect of liquid fraction on the accretion process is investigated.

In order to achieve these objectives, a novel capacitive measurement technique is developed which, for the first time, enables the measurement of the water distribution in an ice layer growing in simulated icing conditions. In addition, the three-dimensional shape and thickness of the accretion are characterized by stereo vision and shadowgraphy.

The accretion process induced by fully frozen particles impacting onto a heated substrate is divided into three stages. In the first stage, impacting ice crystals result in the accumulation of meltwater on the heated surface and cool the substrate. In the second stage, when the surface reaches the freezing temperature, an ice layer forms and grows relatively quickly in thickness. The obtained water distribution demonstrates that the ice layer growth rate is correlated with the liquid volume fraction at the accretion front. The measured relation between liquid fraction and growth rate given in terms of the dimensionless sticking efficiency is presented. As more ice crystals adhere to the wet layer, the liquid fraction and consequently the growth rate decreases. In the subsequent third stage, the liquid fraction at the accretion front and the growth rate are approximately constant, indicating an equilibrium between water supply from the heated substrate and liquid redistribution due to adhering ice crystals.

At positive wet bulb temperatures, the process following the onset of ice accretion is qualitatively different. Liquid water, which facilitates ice accretion, is bound to the partially melted particles. Ice layer growth is thereby not solely determined by the supply of meltwater from the heated substrate.

The application of the novel measurement instrumentation provides detailed insights into aspects that were previously inaccessible to experimental investigations. The experiments confirm the central role of liquid water in ice accretion and contribute valuable data for the improvement of models for the prediction of ice crystal icing.

In a next step, the integration of the two sensors into a single unit could be pursued, enhancing the instrument's usability and potentially broadening its usage

in icing wind tunnel tests.

Furthermore, following a calibration of the icing wind tunnel with respect to the melt ratio, the transition from the regime dominated by melting on the heated substrate to the regime determined by the melt ratio could be investigated.

Overall, in this thesis significant progress has been made in understanding snow and ice crystal icing by investigating the transport processes of airborne snowflakes and the liquid distribution in porous ice accumulations. The gained insights can enhance numerical tools and experimental instrumentation, leading to more accurate predictions of snow and ice crystal icing. Ultimately, this advancement contributes to safer and more efficient air traffic operations.

Bibliography

[1] F. F. Abraham. Functional dependence of drag coefficient of a sphere on Reynolds number. *Physics of Fluids*, 13(8):2194, 1970. ISSN 00319171. doi: 10.1063/1.1693218.

[2] B. Aguilar, P. Trontin, L. Reitter, K. Köbschall, F. Dezitter, I. Roisman, and P. Villedieu. Ice crystal drag model extension to snowflakes: Experimental and numerical investigations. *AIAA Journal*, 60(12):6633–6646, 2022. ISSN 0001-1452. doi: 10.2514/1.J062122.

[3] B. Aguilar, P. Trontin, K. Köbschall, F. Dezitter, J. Hussong, and P. Villedieu. Experimental investigation and semi-empirical modeling of snowflake melting. *International Journal of Heat and Mass Transfer*, 209:124117, 2023. ISSN 00179310. doi: 10.1016/j.ijheatmasstransfer.2023.124117.

[4] W. Ambach and A. Denoth. The dielectric behaviour of snow: A study versus liquid water content. In *NASA workshop on microwave remote sensing of snowpack properties*, pages 69–92, Ft. Collins, Colorado, 1980. NASA.

[5] M. A. B. Andrade, N. Pérez, and J. C. Adamowski. Review of progress in acoustic levitation. *Brazilian Journal of Physics*, 48(2):190–213, 2018. ISSN 0103-9733. doi: 10.1007/s13538-017-0552-6.

[6] D. Atlas, R. Tatehira, R. C. Srivastava, W. Marker, and R. E. Carbone. Precipitation-induced mesoscale wind perturbations in the melting layer. *Quarterly Journal of the Royal Meteorological Society*, 95(405):544–560, 1969. ISSN 00359009. doi: 10.1002/qj.49709540508.

[7] F. Avanzi, H. Hirashima, S. Yamaguchi, T. Katsushima, and C. de Michele. Observations of capillary barriers and preferential flow in layered snow during cold laboratory experiments. *The Cryosphere*, 10(5):2013–2026, 2016. doi: 10.5194/tc-10-2013-2016.

[8] A. T. S. Babb. A radio-frequency electronic moisture meter. *The Analyst*, 76 (898):12, 1951. ISSN 0003-2654. doi: 10.1039/AN9517600012.

[9] G. Bagheri and C. Bonadonna. On the drag of freely falling non-spherical particles. *Powder Technology*, 301(1):526–544, 2016. ISSN 00325910. doi: 10.1016/j.powtec.2016.06.015. URL http://arxiv.org/pdf/1810.08787v1.

[10] B. Baker and R. P. Lawson. Improvement in determination of ice water content from two-dimensional particle imagery. Part I: Image-to-mass relationships. *Journal of Applied Meteorology and Climatology*, 45(9):1282–1290, 2006. ISSN 1558-8424. doi: 10.1175/JAM2398.1.

[11] S. E. Bansmer, A. Baumert, S. Sattler, I. Knop, D. Leroy, A. Schwarzenboeck, T. Jurkat-Witschas, C. Voigt, H. Pervier, and B. Esposito. Design, construction and commissioning of the Braunschweig Icing Wind Tunnel. *Atmospheric Measurement Techniques*, 11(6):3221–3249, 2018. doi: 10.5194/amt-11-3221-2018.

[12] E. Barthazy and R. Schefold. Fall velocity of snowflakes of different riming degree and crystal types. *Atmospheric Research*, 82(1-2):391–398, 2006. ISSN 01698095. doi: 10.1016/j.atmosres.2005.12.009.

[13] A. Baumert, S. Bansmer, P. Trontin, and P. Villedieu. Experimental and numerical investigations on aircraft icing at mixed phase conditions. *International Journal of Heat and Mass Transfer*, 123:957–978, 2018. ISSN 00179310. doi: 10.1016/j.ijheatmasstransfer.2018.02.008.

[14] W. A. Bentley. Photographing snowflakes. *Popular Mechanics*, 37:309–312, 1922.

[15] S. Bhattacharyya, S. Dhinakaran, and A. Khalili. Fluid motion around and through a porous cylinder. *Chemical Engineering Science*, 61(13):4451–4461, 2006. ISSN 00092509. doi: 10.1016/j.ces.2006.02.012.

[16] M. Bittelli, M. Flury, and K. Roth. Use of dielectric spectroscopy to estimate ice content in frozen porous media. *Water Resources Research*, 40(4), 2004. ISSN 00431397. doi: 10.1029/2003WR002343.

[17] M. J. Blunt and H. Scher. Pore-level modeling of wetting. *Physical Review E*, 52(6):6387–6403, 1995. ISSN 1063-651X. doi: 10.1103/PhysRevE.52.6387.

[18] R. Botet and R. Jullien. Fractal aggregates of particles. *Phase Transitions*, 24-26(2):691–736, 1990. ISSN 0141-1594. doi: 10.1080/01411599008210249.

[19] C. G. Bowers, N. JR., and H. D. Bowen. Drying front sensing and signal evaluation for planters. *Transactions of the ASAE*, 18(6):1051–1056, 1975. doi: 10.13031/2013.36736.

[20] E. A. Brandes, K. Ikeda, G. Zhang, M. Schönhuber, and R. M. Rasmussen. A statistical and physical description of hydrometeor distributions in Colorado snowstorms using a video disdrometer. *Journal of Applied Meteorology and Climatology*, 46(5):634–650, 2007. ISSN 1558-8424. URL http://www.jstor.org/stable/26171929.

[21] E. H. Brandt. Suspended by sound. *Nature*, 413(6855):474–475, 2001. ISSN 0028-0836. doi: 10.1038/35097192.

[22] R. A. Brewster, S. Frik, and F. Werner. Computational analysis of automotive windshield de-icing with comparison to test data. In *SAE Technical Paper Series*. SAE International, 1995. doi: 10.4271/971833.

[23] L. Brocca, L. Ciabatta, C. Massari, S. Camici, and A. Tarpanelli. Soil moisture for hydrological applications: Open questions and new opportunities. *Water*, 9(2):140, 2017. doi: 10.3390/w9020140.

[24] P. R. A. Brown and P. N. Francis. Improved measurements of the ice water content in cirrus using a total-water probe. *Journal of Atmospheric and Oceanic Technology*, 12(2):410–414, 1995. ISSN 0739-0572. doi: 10.1175/1520-0426(1995)012<0410:IMOTIW>2.0.CO;2.

[25] D. A. G. Bruggeman. Berechnung verschiedener physikalischer Konstanten von heterogenen Substanzen. I. Dielektrizitätskonstanten und Leitfähigkeiten der Mischkörper aus isotropen Substanzen. *Annalen der Physik*, 416(7): 636–664, 1935. ISSN 00033804. doi: 10.1002/andp.19354160705.

[26] I. P. Castro. Wake characteristics of two-dimensional perforated plates normal to an air-stream. *Journal of Fluid Mechanics*, 46(3):599–609, 1971. ISSN 0022-1120. doi: 10.1017/S0022112071000727.

[27] I. Chatzis and F. Dullien. Dynamic immiscible displacement mechanisms in pore doublets: Theory versus experiment. *Journal of Colloid and Interface Science*, 91(1):199–222, 1983. ISSN 00219797. doi: 10.1016/0021-9797(83)90326-0.

[28] H.-R. Cho, J. V. Iribarne, and W. G. Richards. On the orientation of ice crystals in a cumulonimbus cloud. *Journal of the Atmospheric Sciences*, 38(5): 1111–1114, 1981. ISSN 0022-4928. doi: 10.1175/1520-0469(1981)038<1111:OTOOIC>2.0.CO;2.

[29] W. S. Clayton. Measurement of unsaturated meltwater percolation flux in seasonal snowpack using self-potential. *Journal of Glaciology*, 68(267):25–40, 2022. ISSN 0022-1430. doi: 10.1017/jog.2021.67.

[30] R. Clift and W. H. Gauvin. The motion of particles in turbulent gas streams. *Chemeca '70: A conference convened by the Australian National Committee of the Institution of Chemical Engineers and the Australian Academy of Science*, pages 14–28, 1970.

[31] D. Coelho, J.-F. Thovert, and P. M. Adler. Geometrical and transport properties of random packings of spheres and aspherical particles. *Physical*

Review E, 55(2):1959–1978, 1997. ISSN 1063-651X. doi: 10.1103/PhysRevE.55.1959.

[32] S. C. Colbeck. A theory of water percolation in snow. *Journal of Glaciology*, 11(63):369–385, 1972. ISSN 0022-1430. doi: 10.3189/S0022143000022346.

[33] S. C. Colbeck. The capillary effects on water percolation in homogeneous snow. *Journal of Glaciology*, 13(67):85–97, 1974. ISSN 0022-1430. doi: 10.3189/S002214300002339X.

[34] S. C. Colbeck. Water flow through heterogeneous snow. *Cold Regions Science and Technology*, 1(1):37–45, 1979. ISSN 0165232X. doi: 10.1016/0165-232X(79)90017-X.

[35] C. Coléou, K. Xu, B. Lesaffre, and J.-B. Brzoska. Capillary rise in snow. *Hydrological Processes*, 13(12-13):1721–1732, 1999. ISSN 0885-6087. doi: 10.1002/(SICI)1099-1085(199909)13:12/13<1721::AID-HYP852>3.0.CO;2-D.

[36] J. Connolly. *Ice crystal icing in gas turbine engines*. PhD thesis, University of Oxford, Oxford, 2021.

[37] H. Conway and R. Benedict. Infiltration of water into snow. *Water Resources Research*, 30(3):641–649, 1994. ISSN 00431397. doi: 10.1029/93WR03247.

[38] H. Conway and C. F. Raymond. Snow stability during rain. *Journal of Glaciology*, 39(133):635–642, 1993. ISSN 0022-1430. doi: 10.3189/S0022143000016531.

[39] E. P. Cox. A method of assigning numerical and percentage values to the degree of roundness of sand grains. *Journal of Paleontology*, 1(3):179–183, 1927.

[40] L. Cox, A. Croxford, B. W. Drinkwater, and A. Marzo. Acoustic Lock: Position and orientation trapping of non-spherical sub-wavelength particles in mid-air using a single-axis acoustic levitator. *Applied Physics Letters*, 113 (5):054101, 2018. ISSN 0003-6951. doi: 10.1063/1.5042518.

[41] C. T. Crowe. *Multiphase flow handbook*. Mechanical engineering series. CRC, Boca Raton, Fla. and London, 2005. ISBN 0-8493-1280-9.

[42] E. Cumberbatch. Two-dimensional flow past a mesh. *The Quarterly Journal of Mechanics and Applied Mathematics*, 35(3):335–344, 1982. ISSN 0033-5614. doi: 10.1093/qjmam/35.3.335.

[43] C. Cummins, M. Seale, A. Macente, D. Certini, E. Mastropaolo, I. M. Viola, and N. Nakayama. A separated vortex ring underlies the flight of the dandelion. *Nature*, 562(7727):414–418, 2018. doi: 10.1038/s41586-018-0604-2.

[44] T. C. Currie and D. Fuleki. Development and application of an impedance-based instrument for measuring the liquid fraction and thickness of ice crystal accretions. In *SAE Technical Paper Series*. SAE International, 2015. doi: 10.4271/2015-01-2134.

[45] T. C. Currie and D. Fuleki. Experimental results for ice crystal icing on hemispherical and double wedge geometries at varying Mach numbers and wet bulb temperatures. In *8th AIAA Atmospheric and Space Environments Conference*, Reston, Virginia, 2016. American Institute of Aeronautics and Astronautics. ISBN 978-1-62410-433-6. doi: 10.2514/6.2016-3740.

[46] T. C. Currie, D. Fuleki, and A. Mahallati. Experimental studies of mixed-phase sticking efficiency for ice crystal accretion in jet engines. In *6th AIAA Atmospheric and Space Environments Conference*, Reston, Virginia, 06162014. American Institute of Aeronautics and Astronautics. ISBN 978-1-62410-291-2. doi: 10.2514/6.2014-3049.

[47] T. C. Currie, D. Fuleki, D. C. Knezevici, and J. D. MaCleod. Altitude scaling of ice crystal accretion. In *5th AIAA Atmospheric and Space Environments Conference*, Reston, Virginia, 2013. American Institute of Aeronautics and Astronautics. doi: 10.2514/6.2013-2677.

[48] T. J. Dean, J. P. Bell, and A. Baty. Soil moisture measurement by an improved capacitance technique, Part I. Sensor design and performance. *Journal of Hydrology*, 93(1-2):67–78, 1987. ISSN 00221694. doi: 10.1016/0022-1694(87)90194-6.

[49] A. Denoth. An electronic device for long-term snow wetness recording. *Annals of Glaciology*, 19:104–106, 1994. ISSN 0260-3055. doi: 10.3189/S0260305500011058.

[50] A. Denoth, A. Foglar, P. Weiland, C. Mätzler, H. Aebischer, M. Tiuri, and A. Sihvola. A comparative study of instruments for measuring the liquid water content of snow. *Journal of Applied Physics*, 56(7):2154–2160, 1984. ISSN 0021-8979. doi: 10.1063/1.334215.

[51] R. Descartes. *Les météores*. Imprimerie Jan Maire, Leiden, 1637.

[52] DIN 66165-2:2016-08. Partikelgrößenanalyse - Siebanalyse - Teil 2: Durchführung, 2016.

[53] M. Farzaneh. *Atmospheric icing of power networks*. Springer, Dordrecht and London, 2008. ISBN 978-1-4020-8530-7.

[54] R. M. Fillion, A. R. Riahi, and A. Edrisy. A review of icing prevention in photovoltaic devices by surface engineering. *Renewable and Sustainable*

Energy Reviews, 32:797–809, 2014. ISSN 13640321. doi: 10.1016/j.rser.2014.01.015.

[55] K. E. Fitch, C. Hang, A. Talaei, and T. J. Garrett. Arctic observations and numerical simulations of surface wind effects on multi-angle snowflake camera measurements. *Atmospheric Measurement Techniques*, 14(2):1127–1142, 2021. doi: 10.5194/amt-14-1127-2021.

[56] N. Fries and M. Dreyer. The transition from inertial to viscous flow in capillary rise. *Journal of Colloid and Interface Science*, 327(1):125–128, 2008. ISSN 00219797. doi: 10.1016/j.jcis.2008.08.018.

[57] N. Fries and M. Dreyer. An analytic solution of capillary rise restrained by gravity. *Journal of Colloid and Interface Science*, 320(1):259–263, 2008. ISSN 00219797. doi: 10.1016/j.jcis.2008.01.009.

[58] N. Frössling. Über die Verdunstung fallender Tropfen. *Gerlands Beiträge zur Geophysik*, 52:170–216, 1938.

[59] N. Fukuta, R. C. Savage, G. J. Donovan, and C.-M. Liu. The microphysics of snow crystal and snowflake melting. Technical Report ADA129030, University of Utah, 1982. URL https://apps.dtic.mil/sti/citations/ADA129030.

[60] G. H. Ganser. A rational approach to drag prediction of spherical and nonspherical particles. *Powder Technology*, 77(2):143–152, 1993. ISSN 00325910. doi: 10.1016/0032-5910(93)80051-B.

[61] T. J. Garrett, C. Fallgatter, K. Shkurko, and D. Howlett. Fall speed measurement and high-resolution multi-angle photography of hydrometeors in free fall. *Atmospheric Measurement Techniques*, 5(11):2625–2633, 2012. doi: 10.5194/amt-5-2625-2012.

[62] T. J. Garrett, S. E. Yuter, C. Fallgatter, K. Shkurko, S. R. Rhodes, and J. L. Endries. Orientations and aspect ratios of falling snow. *Geophysical Research Letters*, 42(11):4617–4622, 2015. ISSN 0094-8276. doi: 10.1002/2015GL064040.

[63] L. Gałęzewski, I. Jaskulska, D. Jaskulski, A. Lewandowski, A. Szypłowska, A. Wilczek, and M. Szczepańczyk. Analysis of the need for soil moisture, salinity and temperature sensing in agriculture: A case study in Poland. *Scientific reports*, 11(1):16660, 2021. doi: 10.1038/s41598-021-96182-1.

[64] R. W. Gent, N. P. Dart, and J. T. Cansdale. Aircraft icing. *Philosophical Transactions of the Royal Society of London. Series A: Mathematical, Physical and Engineering Sciences*, 358(1776):2873–2911, 2000. ISSN 1364-503X. doi: 10.1098/rsta.2000.0689.

[65] R. W. Gerdel. The transmission of water through snow. *Transactions, American Geophysical Union*, 35(3):475, 1954. ISSN 0002-8606. doi: 10.1029/TR035i003p00475.

[66] J. Grazioli, G. Ghiggi, A.-C. Billault-Roux, and A. Berne. MASCDB, a database of images, descriptors and microphysical properties of individual snowflakes in free fall. *Scientific Data*, 9(1):1–16, 2022. doi: 10.1038/s41597-022-01269-7.

[67] R. P. Gupta, U. K. Haritashya, and P. Singh. Mapping dry/wet snow cover in the Indian Himalayas using IRS multispectral imagery. *Remote Sensing of Environment*, 97(4):458–469, 2005. ISSN 00344257. doi: 10.1016/j.rse.2005.05.010.

[68] O. Habibzadeh-Bigdarvish, X. Yu, T. Li, G. Lei, A. Banerjee, and A. J. Puppala. A novel full-scale external geothermal heating system for bridge deck de-icing. *Applied Thermal Engineering*, 185:116365, 2021. ISSN 13594311. doi: 10.1016/j.applthermaleng.2020.116365.

[69] A. Haider and O. Levenspiel. Drag coefficient and terminal velocity of spherical and nonspherical particles. *Powder Technology*, 58(1):63–70, 1989. ISSN 00325910. doi: 10.1016/0032-5910(89)80008-7.

[70] A. Hamraoui, K. Thuresson, T. Nylander, and V. Yaminsky. Can a dynamic contact angle be understood in terms of a friction coefficient? *Journal of Colloid and Interface Science*, 226(2):199–204, 2000. ISSN 00219797. doi: 10.1006/jcis.2000.6830.

[71] Z. Hashin and S. Shtrikman. A variational approach to the theory of the effective magnetic permeability of multiphase materials. *Journal of Applied Physics*, 33(10):3125–3131, 1962. ISSN 0021-8979. doi: 10.1063/1.1728579.

[72] T. Hauk. *Investigation of the impact and melting process of ice particles: Untersuchung des Aufschlags-und Schmelzprozesses von Eispartikeln*. Dissertation, Technische Universität Darmstadt, Darmstadt, 2016. URL https://tuprints.ulb.tu-darmstadt.de/5280/1/PhD%20Thesis%20Hauk%20-%20genehmigte%20Version%20final.pdf.

[73] T. Hauk, E. Bonaccurso, I. V. Roisman, and C. Tropea. Ice crystal impact onto a dry solid wall. Particle fragmentation. *Proceedings of the Royal Society A: Mathematical, Physical and Engineering Sciences*, 471(2181):20150399, 2015. ISSN 1364-5021. doi: 10.1098/rspa.2015.0399.

[74] T. Hauk, E. Bonaccurso, P. Villedieu, and P. Trontin. Theoretical and experimental investigation of the melting process of ice particles. *Journal of Thermophysics and Heat Transfer*, 30(4):946–954, 2016. ISSN 0887-8722. doi: 10.2514/1.T4886.

[75] H. He, K. Aogu, M. Li, J. Xu, W. Sheng, S. B. Jones, J. D. González-Teruel, D. A. Robinson, R. Horton, K. Bristow, M. Dyck, V. Filipović, K. Noborio, Q. Wu, H. Jin, H. Feng, B. Si, and J. Lv. A review of time domain reflectometry (TDR) applications in porous media. *Advances in Agronomy*, 168:83–155, 2021. doi: 10.1016/bs.agron.2021.02.003.

[76] M. Heshmati and M. Piri. Experimental investigation of dynamic contact angle and capillary rise in tubes with circular and noncircular cross sections. *Langmuir: the ACS journal of surfaces and colloids*, 30(47):14151–14162, 2014. doi: 10.1021/la501724y.

[77] A. J. Heymsfield and J. Iaquinta. Cirrus crystal terminal velocities. *Journal of the Atmospheric Sciences*, 57(7):916–938, 2000. ISSN 0022-4928. doi: 10.1175/1520-0469(2000)057<0916:CCTV>2.0.CO;2.

[78] A. J. Heymsfield and M. Kajikawa. An improved approach to calculating terminal velocities of plate-like crystals and graupel. *Journal of the Atmospheric Sciences*, 44(7):1088–1099, 1987. ISSN 0022-4928. doi: 10.1175/1520-0469(1987)044<1088:AIATCT>2.0.CO;2.

[79] A. J. Heymsfield and C. D. Westbrook. Advances in the estimation of ice particle fall speeds using laboratory and field measurements. *Journal of the Atmospheric Sciences*, 67(8):2469–2482, 2010. ISSN 0022-4928. doi: 10.1175/2010JAS3379.1.

[80] M. Hilpert. Effects of dynamic contact angle on liquid infiltration into horizontal capillary tubes: (semi)-analytical solutions. *Journal of Colloid and Interface Science*, 337(1):131–137, 2009. ISSN 00219797. doi: 10.1016/j.jcis.2009.04.013.

[81] A. Hölzer and M. Sommerfeld. New simple correlation formula for the drag coefficient of non-spherical particles. *Powder Technology*, 184(3):361–365, 2008. ISSN 00325910. doi: 10.1016/j.powtec.2007.08.021.

[82] H. Ishimoto. Radar backscattering computations for fractal-shaped snowflakes. *Journal of the Meteorological Society of Japan. Ser. II*, 86(3):459–469, 2008. ISSN 0026-1165. doi: 10.2151/jmsj.86.459.

[83] P. Jansson, R. Hock, and T. Schneider. The concept of glacier storage: A review. *Journal of Hydrology*, 282(1-4):116–129, 2003. ISSN 00221694. doi: 10.1016/S0022-1694(03)00258-0.

[84] W. J. Jasinski, S. C. Noe, M. S. Selig, and M. B. Bragg. Wind turbine performance under icing conditions. *Journal of Solar Energy Engineering*, 120(1):60–65, 1998. ISSN 0199-6231. doi: 10.1115/1.2888048.

[85] H. Jeoung, G. Liu, K. Kim, G. Lee, and E.-K. Seo. Microphysical properties of three types of snow clouds: Implication for satellite snowfall retrievals. *Atmospheric Chemistry and Physics*, 20(23):14491–14507, 2020. doi: 10.5194/acp-20-14491-2020.

[86] J. E. Jiusto and G. E. Bosworth. Fall velocity of snowflakes. *Journal of Applied Meteorology*, 10(6):1352–1354, 1971. ISSN 0021-8952. doi: 10.1175/1520-0450(1971)010<1352:FVOS>2.0.CO;2.

[87] G. P. Johari and E. Whalley. The dielectric properties of ice Ih in the range 272–133 K. *The Journal of Chemical Physics*, 75(3):1333–1340, 1981. ISSN 0021-9606. doi: 10.1063/1.442139.

[88] R. Jullien. Aggregation phenomena and fractal aggregates. *Contemporary Physics*, 28(5):477–493, 1987. ISSN 0010-7514. doi: 10.1080/00107518708213736.

[89] M. Junk, J. Hinrichs, F. Polt, J. Fechner, and W. Pauer. Quantitative experimental determination of evaporation influencing factors in single droplet levitation. *International Journal of Heat and Mass Transfer*, 149:119057, 2020. ISSN 00179310. doi: 10.1016/j.ijheatmasstransfer.2019.119057.

[90] M. Kajikawa. Observation of the falling motion of early snowflakes. *Journal of the Meteorological Society of Japan. Ser. II*, 67(5):731–738, 1989. ISSN 0026-1165. doi: 10.2151/jmsj1965.67.5_731.

[91] T. Katsushima, S. Yamaguchi, T. Kumakura, and A. Sato. Experimental analysis of preferential flow in dry snowpack. *Cold Regions Science and Technology*, 85:206–216, 2013. ISSN 0165-232X. doi: 10.1016/j.coldregions.2012.09.012.

[92] R. Kattelmann and J. Dozier. Observations of snowpack ripening in the Sierra Nevada, California, U.S.A. *Journal of Glaciology*, 45(151):409–416, 1999. ISSN 0022-1430. doi: 10.3189/S002214300000126X.

[93] K. Kawashima, T. Endo, and Y. Takeuchi. A portable calorimeter for measuring liquid-water content of wet snow. *Annals of Glaciology*, 26:103–106, 1998. ISSN 0260-3055. doi: 10.3189/1998AoG26-1-103-106.

[94] T. J. Kelleners, D. A. Robinson, P. J. Shouse, J. E. Ayars, and T. H. Skaggs. Frequency dependence of the complex permittivity and its impact on dielectric sensor calibration in soils. *Soil Science Society of America Journal*, 69(1):67–76, 2005. ISSN 0361-5995. doi: 10.2136/sssaj2005.0067a.

[95] J. Kepler. *Strena seu de nive sexangula*. Frankfurt am Main, 1611.

[96] V. I. Khvorostyanov and J. A. Curry. Terminal velocities of droplets and crystals: Power laws with continuous parameters over the size spectrum. *Journal of the Atmospheric Sciences*, 59(11):1872–1884, 2002. ISSN 0022-4928. doi: 10.1175/1520-0469(2002)059<1872:TVODAC>2.0.CO;2.

[97] V. I. Khvorostyanov and J. A. Curry. Fall velocities of hydrometeors in the atmosphere: Refinements to a continuous analytical power law. *Journal of the Atmospheric Sciences*, 62(12):4343–4357, 2005. ISSN 0022-4928. doi: 10.1175/JAS3622.1.

[98] D. M. Kintea, T. Hauk, I. V. Roisman, and C. Tropea. Shape evolution of a melting nonspherical particle. *Physical review. E, Statistical, nonlinear, and soft matter physics*, 92(3):033012, 2015. doi: 10.1103/PhysRevE.92.033012.

[99] D. M. Kintea, I. V. Roisman, and C. Tropea. Transport processes in a wet granular ice layer: Model for ice accretion and shedding. *International Journal of Heat and Mass Transfer*, 97:461–472, 2016. ISSN 00179310. doi: 10.1016/j.ijheatmasstransfer.2016.01.076.

[100] S. Kirkpatrick. Percolation and conduction. *Reviews of Modern Physics*, 45 (4):574–588, 1973. ISSN 0034-6861. doi: 10.1103/RevModPhys.45.574.

[101] C. A. Knight. The contact angle of water on ice. *Journal of Colloid and Interface Science*, 25(2):280–284, 1967. ISSN 00219797. doi: 10.1016/0021-9797(67)90031-8.

[102] C. A. Knight. Observations of the morphology of melting snow. *Journal of the Atmospheric Sciences*, 36(6):1123–1130, 1979. ISSN 0022-4928. doi: 10.1175/1520-0469(1979)036<1123:OOTMOM>2.0.CO;2.

[103] K. Köbschall, J. Breitenbach, I. V. Roisman, C. Tropea, and J. Hussong. Geometric descriptors for the prediction of snowflake drag. *Experiments in Fluids*, 64(1), 2023. ISSN 0723-4864. doi: 10.1007/s00348-022-03539-x.

[104] K. Köbschall, B. Traut, I. V. Roisman, C. Tropea, and J. Hussong. Melting of fractal snowflakes: Experiments and modeling. *International Journal of Heat and Mass Transfer*, 212:124254, 2023. ISSN 00179310. doi: 10.1016/j.ijheatmasstransfer.2023.124254.

[105] J. L. Laforte, M. A. Allaire, and J. Laflamme. State-of-the-art on power line de-icing. *Atmospheric Research*, 46(1-2):143–158, 1998. ISSN 01698095. doi: 10.1016/S0169-8095(97)00057-4.

[106] M. P. Langleben. The terminal velocity of snowflakes. *Quarterly Journal of the Royal Meteorological Society*, 80(344):174–181, 1954. ISSN 00359009. doi: 10.1002/qj.49708034404.

[107] R. P. Lawson, L. J. Angus, and A. J. Heymsfield. Cloud particle measurements in thunderstorm anvils and possible weather threat to aviation. *Journal of Aircraft*, 35(1):113–121, 1998. ISSN 0021-8669. doi: 10.2514/2.2268.

[108] J. Leinonen and A. von Lerber. Snowflake melting simulation using smoothed particle hydrodynamics. *Journal of Geophysical Research: Atmospheres*, 123 (3):1811–1825, 2018. ISSN 2169-897X. doi: 10.1002/2017JD027909.

[109] J. Leinonen, D. Moisseev, and T. Nousiainen. Linking snowflake microstructure to multi-frequency radar observations. *Journal of Geophysical Research: Atmospheres*, 118(8):3259–3270, 2013. ISSN 2169897X. doi: 10.1002/jgrd.50163.

[110] J. Leinonen, J. Grazioli, and A. Berne. Reconstruction of the mass and geometry of snowfall particles from multi-angle snowflake camera (MASC) images. *Atmospheric Measurement Techniques*, 14(10):6851–6866, 2021. doi: 10.5194/amt-14-6851-2021.

[111] K. G. Libbrecht. A quantitative physical model of the snow crystal morphology diagram. 2019. doi: 10.48550/arXiv.1910.09067.

[112] K. Lichtenecker. Die Dielektrizitätskonstante natürlicher und künstlicher Mischkörper. *Physikalische Zeitschrift*, 27:115–133, 1926.

[113] L. Lilie, E. Emery, J. Strapp, and J. Emery. A multiwire hot-wire device for measurement of icing severity, total water content, liquid water content, and droplet diameter. In *43rd AIAA Aerospace Sciences Meeting and Exhibit*, Reston, Virigina, 2005. American Institute of Aeronautics and Astronautics. ISBN 978-1-62410-064-2. doi: 10.2514/6.2005-859.

[114] J. Liu, S. Zhao, L. Jiang, L. Chai, and F. Wu. The influence of organic matter on soil dielectric constant at microwave frequencies (0.5–40 GHz). In *2013 IEEE International Geoscience and Remote Sensing Symposium - IGARSS*, pages 13–16. IEEE, 2013. ISBN 978-1-4799-1114-1. doi: 10.1109/IGARSS.2013.6721080.

[115] J. D. Locatelli and P. V. Hobbs. Fall speeds and masses of solid precipitation particles. *Journal of Geophysical Research*, 79(15):2185–2197, 1974. ISSN 01480227. doi: 10.1029/JC079i015p02185.

[116] E. Loth. Drag of non-spherical solid particles of regular and irregular shape. *Powder Technology*, 182(3):342–353, 2008. ISSN 00325910. doi: 10.1016/j.powtec.2007.06.001.

[117] R. Lucas. Ueber das Zeitgesetz des kapillaren Aufstiegs von Flüssigkeiten. *Kolloid-Zeitschrift*, 23(1):15–22, 1918. ISSN 0303-402X. doi: 10.1007/bf01461107.

[118] A. V. Luikov. Heat and mass transfer in capillary-porous bodies. In *Advances in Heat Transfer Volume 1*, volume 1 of *Advances in Heat Transfer*, pages 123–184. Elsevier, 1964. ISBN 9780120200016. doi: 10.1016/S0065-2717(08)70098-4.

[119] A. Lundberg. Laboratory calibration of TDR-probes for snow wetness measurements. *Cold Regions Science and Technology*, 25(3):197–205, 1997. ISSN 0165232X. doi: 10.1016/S0165-232X(96)00012-2.

[120] C. Magono and C. W. Lee. Meteorological classification of natural snow crystals. *Journal of the Faculty of Science, Hokkaido University. Series 7, Geophysics*, 2(4):321–335, 1966.

[121] C. Magono and T. Nakamura. Aerodynamic studies of falling snowflakes. *Journal of the Meteorological Society of Japan. Ser. II*, 43(3):139–147, 1965. ISSN 0026-1165. doi: 10.2151/jmsj1965.43.3_139.

[122] L. Makkonen. Estimation of wet snow accretion on structures. *Cold Regions Science and Technology*, 17(1):83–88, 1989. ISSN 0165232X. doi: 10.1016/S0165-232X(89)80018-7.

[123] Y. A. Malik, L. Bennani, A. Vorgias, P. Trontin, and P. Villedieu. Experimental and numerical investigation of ice crystal icing on a heatable NACA0012 airfoil. In *AIAA AVIATION 2022 Forum*, Reston, Virginia, 2022. American Institute of Aeronautics and Astronautics. ISBN 978-1-62410-635-4. doi: 10.2514/6.2022-3534.

[124] A. Marzo, A. Barnes, and B. W. Drinkwater. TinyLev: A multi-emitter single-axis acoustic levitator. *The Review of scientific instruments*, 88(8):085105, 2017. doi: 10.1063/1.4989995.

[125] J. H. Masliyah and M. Polikar. Terminal velocity of porous spheres. *The Canadian Journal of Chemical Engineering*, 58(3):299–302, 1980. ISSN 00084034. doi: 10.1002/cjce.5450580303.

[126] B. J. Mason. On the melting of hailstones. *Quarterly Journal of the Royal Meteorological Society*, 82(352):209–216, 1956. ISSN 00359009. doi: 10.1002/qj.49708235207.

[127] J. Mason, W. Strapp, and P. Chow. The ice particle threat to engines in flight. In *44th AIAA Aerospace Sciences Meeting and Exhibit*, Reston, Virigina, 2006. American Institute of Aeronautics and Astronautics. ISBN 978-1-62410-039-0. doi: 10.2514/6.2006-206.

[128] J. G. Mason, P. Chow, and D. M. Fuleki. Understanding ice crystal accretion and shedding phenomenon in jet engines using a rig test. *Journal of*

Engineering for Gas Turbines and Power, 133(4), 2011. ISSN 0742-4795. doi: 10.1115/1.4002020.

[129] S. Y. Matrosov. Theoretical study of radar polarization parameters obtained from cirrus clouds. *Journal of the Atmospheric Sciences*, 48(8):1062–1070, 1991. ISSN 0022-4928. doi: 10.1175/1520-0469(1991)048<1062:TSORPP>2.0.CO;2.

[130] T. Matsuo and Y. Sasyo. Empirical formula for the melting rate of snowflakes. *Journal of the Meteorological Society of Japan. Ser. II*, 59(1):1–9, 1981. ISSN 0026-1165. doi: 10.2151/jmsj1965.59.1_1.

[131] T. Matsuo and Y. Sasyo. Melting of snowflakes below freezing level in the atmosphere. *Journal of the Meteorological Society of Japan. Ser. II*, 59(1): 10–25, 1981. ISSN 0026-1165. doi: 10.2151/jmsj1965.59.1_10.

[132] J. C. Maxwell Garnett. XII. Colours in metal glasses and in metallic films. *Philosophical Transactions of the Royal Society of London. Series A, Containing Papers of a Mathematical or Physical Character*, 203(359-371):385–420, 1904. ISSN 0264-3952. doi: 10.1098/rsta.1904.0024.

[133] M. W. McCorquodale and C. D. Westbrook. TRAIL: A novel approach for studying the aerodynamics of ice particles. *Quarterly Journal of the Royal Meteorological Society*, 147(734):589–604, 2021. ISSN 00359009. doi: 10.1002/qj.3935.

[134] M. W. McCorquodale and C. D. Westbrook. TRAIL part 2: A comprehensive assessment of ice particle fall speed parametrisations. *Quarterly Journal of the Royal Meteorological Society*, 147(734):605–626, 2021. ISSN 00359009. doi: 10.1002/qj.3936.

[135] H. G. Merkus. *Particle size measurements: Fundamentals, practice, quality*, volume 17 of *Particle technology series*. Springer, New York, 2009. ISBN 978-1-4020-9016-5.

[136] B. L. Messinger. Equilibrium temperature of an unheated icing surface as a function of air speed. *Journal of the Aeronautical Sciences*, 20(1):29–42, 1953. doi: 10.2514/8.2520.

[137] D. J. Millard. The electrical measurement of moisture in granular materials. *British Journal of Applied Physics*, 4(3):84–87, 1953. ISSN 0508-3443. doi: 10.1088/0508-3443/4/3/305.

[138] D. L. Mitchell. Use of mass- and area-dimensional power laws for determining precipitation particle terminal velocities. *Journal of the Atmospheric Sciences*, 53(12):1710–1723, 1996. ISSN 0022-4928. doi: 10.1175/1520-0469(1996)053<1710:UOMAAD>2.0.CO;2.

[139] D. L. Mitchell and A. J. Heymsfield. Refinements in the treatment of ice particle terminal velocities, highlighting aggregates. *Journal of the Atmospheric Sciences*, 62(5):1637–1644, 2005. ISSN 0022-4928. doi: 10.1175/JAS3413.1.

[140] D. L. Mitchell, R. Zhang, and R. L. Pitter. Mass-dimensional relationships for ice particles and the influence of riming on snowfall rates. *Journal of Applied Meteorology*, 29(2):153–163, 1990. ISSN 0894-8763. doi: 10.1175/1520-0450(1990)029<0153:MDRFIP>2.0.CO;2.

[141] S. K. Mitra, O. Vohl, M. Ahr, and H. R. Pruppacher. A wind tunnel and theoretical study of the melting behavior of atmospheric ice particles. IV: Experiment and theory for snow flakes. *Journal of the Atmospheric Sciences*, 47(5):584–591, 1990. ISSN 0022-4928. doi: 10.1175/1520-0469(1990)047<0584:AWTATS>2.0.CO;2.

[142] U. Nakaya and T. Terada. Simultaneous observations of the mass, falling velocity and form of individual snow crystals. *Journal of the Faculty of Science, Hokkaido Imperial University. Ser. 2, Physics*, 1(7):191–200, 1935. URL http://hdl.handle.net/2115/34452.

[143] A. N. Nevzorov. Aircraft cloud water content meter. In *Communication présentée à la 8ème conférence internationale sur la physique des nuages*, volume 2, pages 701–703, Clermont-Ferrand, France, 1980.

[144] R. F. Paetzold, G. A. Matzkanin, and A. de Los Santos. Surface soil water content measurement using pulsed nuclear magnetic resonance techniques. *Soil Science Society of America Journal*, 49(3):537–540, 1985. ISSN 0361-5995. doi: 10.2136/sssaj1985.03615995004900030001x.

[145] O. Parent and A. Ilinca. Anti-icing and de-icing techniques for wind turbines: Critical review. *Cold Regions Science and Technology*, 65(1):88–96, 2011. ISSN 0165232X. doi: 10.1016/j.coldregions.2010.01.005.

[146] A. Pentland. A method of measuring the angularity of sands. *Proceedings and Transactions of the Royal Society of Canada*, 21(3):43, 1927.

[147] D. Polder and J. H. van Santeen. The effective permeability of mixtures of solids. *Physica*, 12(5):257–271, 1946. ISSN 00318914. doi: 10.1016/S0031-8914(46)80066-1.

[148] G. Poots. *Ice and snow accretion on structures*, volume vol.10 of *Applied and engineering mathematics series*. Research Studies Press, Taunton, 1996. ISBN 978-0863801891.

[149] C. Praz, Y.-A. Roulet, and A. Berne. Solid hydrometeor classification and riming degree estimation from pictures collected with a Multi-Angle Snowflake

Camera. *Atmospheric Measurement Techniques*, 10(4):1335–1357, 2017. doi: 10.5194/amt-10-1335-2017.

[150] H. R. Pruppacher and J. D. Klett. *Microphysics of clouds and precipitation*, volume 18. Springer, Dordrecht, 2010. ISBN 978-0-7923-4211-3. doi: 10.1007/978-0-306-48100-0.

[151] L. Ragni, E. Iaccheri, C. Cevoli, A. Berardinelli, A. Bendini, and T. G. Toschi. A capacitive technique to assess water content in extra virgin olive oils. *Journal of Food Engineering*, 116(1):246–252, 2013. ISSN 02608774. doi: 10.1016/j.jfoodeng.2012.10.031.

[152] R. Rasmussen and H. R. Pruppacher. A wind tunnel and theoretical study of the melting behavior of atmospheric ice particles. I: A wind tunnel study of frozen drops of radius $< 500\,\mu m$. *Journal of the Atmospheric Sciences*, 39 (1):152–158, 1982. ISSN 0022-4928. doi: 10.1175/1520-0469(1982)039<0152:AWTATS>2.0.CO;2.

[153] R. M. Rasmussen, V. Levizzani, and H. R. Pruppacher. A wind tunnel and theoretical study of the melting behavior of atmospheric ice particles. II: A theoretical study for frozen drops of radius $< 500\,\mu m$. *Journal of the Atmospheric Sciences*, 41(3):374–380, 1984. ISSN 0022-4928. doi: 10.1175/1520-0469(1984)041<0374:AWTATS>2.0.CO;2.

[154] R. M. Rasmussen, V. Levizzani, and H. R. Pruppacher. A wind tunnel and theoretical study on the melting behavior of atmospheric ice particles: III. Experiment and theory for spherical ice particles of radius $> 500\,\mu m$. *Journal of the Atmospheric Sciences*, 41(3):381–388, 1984. ISSN 0022-4928. doi: 10.1175/1520-0469(1984)041<0381:AWTATS>2.0.CO;2.

[155] L. M. Reitter, H. Lohmann, M. Schremb, I. V. Roisman, J. Hussong, and C. Tropea. Impact of an ice particle onto a dry rigid substrate: Dynamic sintering of a residual ice cone. *Cold Regions Science and Technology*, 194: 103416, 2022. ISSN 0165232X. doi: 10.1016/j.coldregions.2021.103416.

[156] L. A. Richards. Capillary conduction of liquids through porous mediums. *Physics*, 1(5):318–333, 1931. ISSN 0148-6349. doi: 10.1063/1.1745010.

[157] A. Richter and P. A. Nikrityuk. Drag forces and heat transfer coefficients for spherical, cuboidal and ellipsoidal particles in cross flow at sub-critical Reynolds numbers. *International Journal of Heat and Mass Transfer*, 55(4): 1343–1354, 2012. ISSN 00179310. doi: 10.1016/j.ijheatmasstransfer.2011.09.005.

[158] J. T. Riley. Mixed-phase icing conditions: A review, 1998. URL https://www.tc.faa.gov/its/worldpac/techrpt/ar98-76.pdf.

[159] A. Roostaee and M. Vaezi. Developing a standard platform to predict the drag coefficient of irregular shape particles. *Powder Technology*, 395:314–337, 2022. ISSN 00325910. doi: 10.1016/j.powtec.2021.09.037.

[160] S. A. Rutledge and P. V. Hobbs. The mesoscale and microscale structure and organization of clouds and precipitation in midlatitude cyclones. XII: A diagnostic modeling study of precipitation development in narrow cold-frontal rainbands. *Journal of the Atmospheric Sciences*, 41(20):2949–2972, 1984. ISSN 0022-4928. doi: 10.1175/1520-0469(1984)041<2949:TMAMSA>2.0.CO;2.

[161] C. G. Schmitt and A. J. Heymsfield. The dimensional characteristics of ice crystal aggregates from fractal geometry. *Journal of the Atmospheric Sciences*, 67(5):1605–1616, 2010. ISSN 0022-4928. doi: 10.1175/2009JAS3187.1.

[162] M. Schneebeli. Development and stability of preferential flow paths in a layered snowpack. *Biogeochemistry of Seasonally Snow Covered Basins*, 228: 89–96, 01 1995.

[163] S. Sellers. Theory of water transport in melting snow with a moving surface. *Cold Regions Science and Technology*, 31(1):47–57, 2000. ISSN 0165-232X. doi: 10.1016/S0165-232X(00)00006-9.

[164] Y. Shiri and S. M. J. Seyed Sabour. Analytical, experimental, and numerical study of capillary rise dynamics from inertial to viscous flow. *Physics of Fluids*, 34(10):102105, 2022. ISSN 1070-6631. doi: 10.1063/5.0111688.

[165] A. Sihvola and M. Tiuri. Snow fork for field determination of the density and wetness profiles of a snow pack. *IEEE Transactions on Geoscience and Remote Sensing*, GE-24(5):717–721, 1986. ISSN 0196-2892. doi: 10.1109/TGRS.1986.289619.

[166] A. H. Sihvola. *Electromagnetic mixing formulas and applications*. IEE electromagnetic waves series 47. Institution of Electrical Engineers, London, 1999. ISBN 9780852967720.

[167] E. M. Sparrow, J. P. Abraham, and J. C. Tong. Archival correlations for average heat transfer coefficients for non-circular and circular cylinders and for spheres in cross-flow. *International Journal of Heat and Mass Transfer*, 47(24):5285–5296, 2004. ISSN 00179310. doi: 10.1016/j.ijheatmasstransfer.2004.06.024.

[168] J. H. Spurk and N. Aksel. *Fluid Mechanics*. Springer International Publishing, Cham, 2020. ISBN 978-3-030-30258-0. doi: 10.1007/978-3-030-30259-7.

[169] J. R. Stallabrass. Engine snow ingestion in the Bell 206A Jet Ranger helicopter, 1971. URL https://apps.dtic.mil/sti/citations/AD0721516.

[170] M. Stange, M. E. Dreyer, and H. J. Rath. Capillary driven flow in circular cylindrical tubes. *Physics of Fluids*, 15(9):2587–2601, 2003. ISSN 1070-6631. doi: 10.1063/1.1596913.

[171] J. Stein, G. Laberge, and D. Lévesque. Monitoring the dry density and the liquid water content of snow using time domain reflectometry (TDR). *Cold Regions Science and Technology*, 25(2):123–136, 1997. ISSN 0165232X. doi: 10.1016/S0165-232X(96)00022-5.

[172] K. Steiros and M. Hultmark. Drag on flat plates of arbitrary porosity. *Journal of Fluid Mechanics*, 853, 2018. ISSN 0022-1120. doi: 10.1017/jfm.2018.621.

[173] G. L. Stephens. Radiative properties of cirrus clouds in the infrared region. *Journal of the Atmospheric Sciences*, 37(2):435–446, 1980. ISSN 0022-4928. doi: 10.1175/1520-0469(1980)037<0435:RPOCCI>2.0.CO;2.

[174] G. N. Stevens and M. Hughes. Moisture meter performance in field and laboratory. *Journal of Agricultural Engineering Research*, 11(3):210–217, 1966. ISSN 00218634. doi: 10.1016/S0021-8634(66)80023-9.

[175] J. W. Strapp, L. E. Lilie, T. P. Ratvasky, C. R. Davison, and C. Dumont. Isokinetic TWC evaporator probe: Development of the IKP2 and performance testing for the HAIC-HIWC Darwin 2014 and Cayenne field campaigns. In *8th AIAA Atmospheric and Space Environments Conference*, Reston, Virginia, 2016. American Institute of Aeronautics and Astronautics. ISBN 978-1-62410-433-6. doi: 10.2514/6.2016-4059.

[176] P. Struk, T. Currie, W. B. Wright, D. C. Knezevici, D. Fuleki, A. Broeren, M. Vargas, and J.-C. Tsao. Fundamental ice crystal accretion physics studies. In *SAE Technical Paper Series*. SAE International, 2011. doi: 10.4271/2011-38-0018.

[177] A. Szymkiewicz. *Modelling water flow in unsaturated porous media*. Springer Berlin Heidelberg, Berlin, Heidelberg, 2013. ISBN 978-3-642-23558-0. doi: 10.1007/978-3-642-23559-7.

[178] W. Szyrmer and I. Zawadzki. Modeling of the melting layer. Part I: Dynamics and microphysics. *Journal of the Atmospheric Sciences*, 56(20):3573–3592, 1999. ISSN 0022-4928. doi: 10.1175/1520-0469(1999)056<3573:MOTMLP>2.0.CO;2.

[179] G. Tagliavini, M. McCorquodale, C. Westbrook, P. Corso, Q. Krol, and M. Holzner. Drag coefficient prediction of complex-shaped snow particles falling in air beyond the Stokes regime. *International Journal of Multiphase Flow*, 140:103652, 2021. ISSN 03019322. doi: 10.1016/j.ijmultiphaseflow.2021.103652.

[180] G. Tagliavini, M. McCorquodale, C. Westbrook, and M. Holzner. Numerical analysis of the wake of complex-shaped snow particles at moderate Reynolds number. *Physics of Fluids*, 33(10):105103, 2021. ISSN 1070-6631. doi: 10.1063/5.0064902.

[181] Y. Takano, K. N. Liou, and P. Minnis. The effects of small ice crystals on cirrus infrared radiative properties. *Journal of the Atmospheric Sciences*, 49(16): 1487–1493, 1992. ISSN 0022-4928. doi: 10.1175/1520-0469(1992)049<1487: TEOSIC>2.0.CO;2.

[182] G. I. Taylor. Air resistance of a flat plate of very porous material. *Aeronautical Research Council, Reports and Memoranda*, 2236:159–162, 1944.

[183] F. Techel and C. Pielmeier. Point observations of liquid water content in wet snow – investigating methodical, spatial and temporal aspects. *The Cryosphere*, 5(2):405–418, 2011. doi: 10.5194/tc-5-405-2011.

[184] A. M. Thomas. In situ measurement of moisture in soil and similar substances by 'fringe' capacitance. *Journal of Scientific Instruments*, 43(1):21–27, 1966. ISSN 0950-7671. doi: 10.1088/0950-7671/43/1/306.

[185] S. Tran-Cong, M. Gay, and E. E. Michaelides. Drag coefficients of irregularly shaped particles. *Powder Technology*, 139(1):21–32, 2004. ISSN 00325910. doi: 10.1016/j.powtec.2003.10.002.

[186] P. Trontin and P. Villedieu. A comprehensive accretion model for glaciated icing conditions. *International Journal of Multiphase Flow*, 108:105–123, 2018. ISSN 03019322. doi: 10.1016/j.ijmultiphaseflow.2018.06.023.

[187] P. Trontin, G. Blanchard, and P. Villedieu. A comprehensive numerical model for mixed-phase and glaciated icing conditions. In *8th AIAA Atmospheric and Space Environments Conference*, Reston, Virginia, 2016. American Institute of Aeronautics and Astronautics. ISBN 978-1-62410-433-6. doi: 10.2514/6.2016-3742.

[188] C. H. M. van Bavel. Neutron measurement of surface soil moisture. *Journal of Geophysical Research: Atmospheres*, 66(12):4193–4198, 1961. ISSN 01480227. doi: 10.1029/JZ066i012p04193.

[189] P. Villedieu, P. Trontin, and R. Chauvin. Glaciated and mixed phase ice accretion modeling using ONERA 2D icing suite. In *6th AIAA Atmospheric and Space Environments Conference*, Reston, Virginia, 2014. American Institute of Aeronautics and Astronautics. ISBN 978-1-62410-291-2. doi: 10.2514/6.2014-2199.

[190] A. R. von Hippel. The dielectric relaxation spectra of water, ice, and aqueous solutions, and their interpretation. I. Critical survey of the status-quo for water. *IEEE Transactions on Electrical Insulation*, 23(5):801–816, 1988. ISSN 00189367. doi: 10.1109/14.8745.

[191] P. A. Waldner, M. Schneebeli, U. Schultze-Zimmermann, and H. Flühler. Effect of snow structure on water flow and solute transport. *Hydrological Processes*, 18(7):1271–1290, 2004. ISSN 0885-6087. doi: 10.1002/hyp.1401.

[192] Y. Wang, L. Zhou, Y. Wu, and Q. Yang. New simple correlation formula for the drag coefficient of calcareous sand particles of highly irregular shape. *Powder Technology*, 326:379–392, 2018. ISSN 00325910. doi: 10.1016/j.powtec.2017.12.004.

[193] Z. Wang, J.-M. Pereira, E. Sauret, and Y. Gan. Emergence of unstable invasion during imbibition in regular porous media. *Journal of Fluid Mechanics*, 941, 2022. ISSN 0022-1120. doi: 10.1017/jfm.2022.336.

[194] E. W. Washburn. The dynamics of capillary flow. *Physical Review*, 17(3):273–283, 1921. ISSN 0031-899X. doi: 10.1103/PhysRev.17.273.

[195] C. D. Westbrook. The fall speeds of sub-100 µm ice crystals. *Quarterly Journal of the Royal Meteorological Society*, 134(634):1243–1251, 2008. ISSN 00359009. doi: 10.1002/qj.290.

[196] N. Wever, C. Vera Valero, and F. Techel. Coupled snow cover and avalanche dynamics simulations to evaluate wet snow avalanche activity. *Journal of Geophysical Research: Earth Surface*, 123(8):1772–1796, 2018. ISSN 2169-9003. doi: 10.1029/2017JF004515.

[197] R. Wexler, R. J. Reed, and J. Honig. Atmospheric cooling by melting snow. *Bulletin of the American Meteorological Society*, 35(2):48–51, 1954. ISSN 0003-0007. doi: 10.1175/1520-0477-35.2.48.

[198] W. R. Whalley. Development and evaluation of a microwave soil moisturesensor for incorporation in a narrow cultivator tine. *Journal of Agricultural Engineering Research*, 50:25–33, 1991. ISSN 00218634. doi: 10.1016/S0021-8634(05)80003-4.

[199] W. R. Whalley, T. J. Dean, and P. Izzard. Evaluation of the capacitance technique as a method for dynamically measuring soil water content. *Journal of Agricultural Engineering Research*, 52:147–155, 1992. ISSN 00218634. doi: 10.1016/0021-8634(92)80056-X.

[200] O. Wiener. Zur Theorie der Refractionskonstanten. *Berichte über die Verhandlungen der königlich-sächsischen Gesellschaft der Wissenschaften zu Leipzig, Mathematisch-Physikalische Klasse*, 62(5):256–277, 1910.

[201] W. W. Willmarth, N. E. Hawk, and R. L. Harvey. Steady and unsteady motions and wakes of freely falling disks. *Physics of Fluids*, 7(2):197, 1964. ISSN 00319171. doi: 10.1063/1.1711133.

[202] D. R. Wilson and S. P. Ballard. A microphysically based precipitation scheme for the UK meteorological office unified model. *Quarterly Journal of the Royal Meteorological Society*, 125(557):1607–1636, 1999. ISSN 00359009. doi: 10.1002/qj.49712555707.

[203] W. Wright, P. Jorgenson, and J. Veres. Mixed phase modeling in GlennICE with application to engine icing. In *AIAA Atmospheric and Space Environments Conference*, Reston, Virigina, 2010. American Institute of Aeronautics and Astronautics. ISBN 978-1-62410-149-6. doi: 10.2514/6.2010-7674.

[204] A. L. Yarin, G. Brenn, J. Keller, M. Pfaffenlehner, E. Ryssel, and C. Tropea. Flowfield characteristics of an aerodynamic acoustic levitator. *Physics of Fluids*, 9(11):3300–3314, 1997. ISSN 1070-6631. doi: 10.1063/1.869444.

[205] R. Zallen, editor. *The physics of amorphous solids*. Wiley-VCH Verlag GmbH, Weinheim, Germany, 1998. ISBN 9783527617968. doi: 10.1002/9783527617968.

[206] A. Zermeo-Gonzlez, J. Munguia-Lpez, M. Cadena-Zapata, S. Gabriel, L. Ibarra-Jimnez, and R. Rodrguez-Garc. Critical evaluation of different techniques for determining soil water content. In M. Kumar, editor, *Problems, perspectives and challenges of agricultural water management*. InTech, 2012. ISBN 978-953-51-0117-8. doi: 10.5772/30633.

[207] W. Zhang, K. E. Thompson, A. H. Reed, and L. Beenken. Relationship between packing structure and porosity in fixed beds of equilateral cylindrical particles. *Chemical Engineering Science*, 61(24):8060–8074, 2006. ISSN 00092509. doi: 10.1016/j.ces.2006.09.036.

[208] B. Zhao, C. W. MacMinn, and R. Juanes. Wettability control on multiphase flow in patterned microfluidics. *Proceedings of the National Academy of Sciences of the United States of America*, 113(37):10251–10256, 2016. doi: 10.1073/pnas.1603387113.

Nomenclature

Latin letters, uppercase

Symbol	Description
A	Area
AR	Aspect ratio
C	Capacitance
C_0	Parasitic capacitance
C_g	Geometric capacitance
$D_\mathrm{v,a}$	Diffusivity of water vapor in air
F_d	Drag force
IWC	Ice water content
L	Triangle leg length
L_f	Latent heat of fusion
L_v	Latent heat of evaporation
N	Number
Nu	Nusselt number
P	Perimeter
Pr	Prandtl number
R	Radius
Re	Reynolds number
S	Projected length
Sc	Schmidt number
Sh	Sherwood number
St	Stefan number
T	Temperature
V	Volume

Latin letters, lowercase

Symbol	Description
$a_1, \ldots, a_5$	Parameters in Equation 1.7
$b_0, \ldots, b_3$	Parameters in Equation 4.2
c_d	Drag coefficient
c_p	Isobaric specific heat capacity
d	Particle size

g	Gravitational acceleration
h	Thickness
$\dot{h}$	Growth rate
h_h	Heat transfer coefficient
h_m	Mass transfer coefficient
k	Thermal conductivity
l	Shape parameter
m	Mass
$\dot{m}_\mathrm{f}$	Melting rate
p	Pressure
s	Shape parameter
t	Time
u	Velocity
u_*	Volume flux
v^*_liq	Parameter in Equation 5.1
w	Normalized sensitivity
x, y, z	Coordinates

Greek letters, uppercase

Symbol	**Description**
Φ	Sphericity
$\Phi_\perp$	Crosswise sphericity
Ψ	Cox roundness
Ω	Angle, solid angle

Greek letters, lowercase

Symbol	**Description**
α	Factor in mass–size power law
β	Mass fractal dimension
γ	Inclination angle (see Figure 2.10)
δ	Parameter in Equation 5.1
ε_r	Relative permittivity
$\overline{\varepsilon}_\mathrm{r}$	Relative permittivity weighted according to the sensitivity profile
ζ	Depolarization factor
η_c	Collection efficiency
η_s	Sticking efficiency
κ	Permeability
μ	Parameter in log-normal distribution
ν	Kinematic viscosity

ρ	Density
σ	Parameter in log-normal distribution
τ	Dimensionless time
φ	Porosity
ω	Vapor mass fraction

Subscripts

Subscript	**Description**
2D	Two-dimensional
a	Air
acc	Accretion
B	Bruggeman model
eq	Volume equivalent
HSL	Lower Hashin-Shtrikman bound
HSU	Upper Hashin-Shtrikman bound
i	Ice
liq	Liquid
m	Melting
max	Maximum
p	Projected
par	Parallel
ref	Reference
s	Surface
ser	Serial
std	Standardized
w	Liquid water
$\perp$	Orthogonal
$\parallel$	Parallel
$\diamondsuit$	Tetrahedron
$\triangle$	Triangle

Abbreviations

Abbreviation	**Description**
FEP	Fluorinated ethylene propylene
I^2C	Inter-integrated circuit
ONERA	Office national d'études et de recherches aérospatiales
PCB	Printed circuit board
PTFE	Polytetrafluoroethylene
TU	Technische Universität

List of Figures

,

List of Tables